

https://dspace.org/

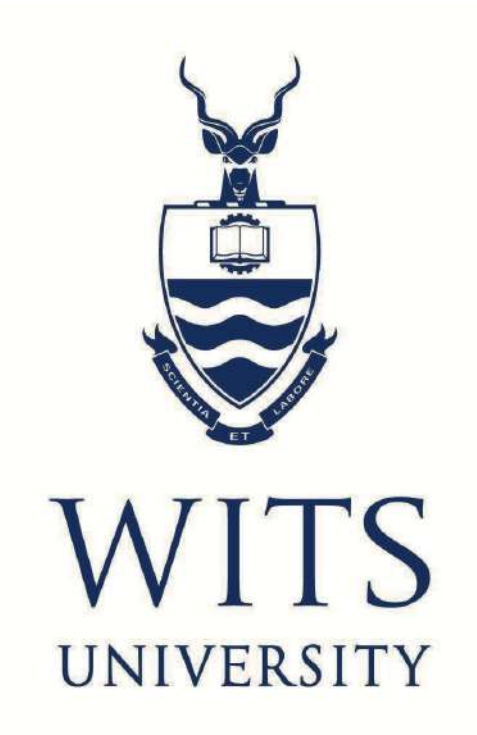
Exploring the influence of geological characteristics, surface texture, and surface energy of crushed rock aggregates on the compressive strength of concrete

Govender, Damisha

2025-08
University of the Witwatersrand, Johannesburg
https://hdl.handle.net/10539/50271

Govender, Damisha. (2025). Exploring the influence of geological characteristics, surface texture, and surface energy of crushed rock aggregates on the compressive strength of concrete. [Master's dissertation, University of the Witwatersrand, Johannesburg]. WIReDSpace. https://hdl.handle.net/10539/50271

Downloaded from a DSpace repository. https://dspace.org/



Exploring the influence of geological characteristics, surface texture, and surface energy of crushed rock aggregates on the compressive strength of concrete

by

Damisha Govender

2113150

A Dissertation

Submitted in fulfilment of the requirements for the degree

Master of Science

in

Geology

In the Faculty of Science, University of the Witwatersrand, Johannesburg, South Africa

Supervisor: Dr Nonkuselo Madlakana

Co-supervisor: Prof. Yunus Ballim

August 2025

Declaration

I declare that this dissertation is my own, unaided work. It is being submitted for the Degree of Master of Science in Geology at the University of the Witwatersrand, Johannesburg. It has not been submitted before for any degree or examination at any other University.



(Signature of candidate)

12 August 2025

(Date)

Abstract

Concrete is a globally used construction material valued for its strength, which has long been primarily determinant on the water-to-cement ratio. However, studies indicate that aggregate properties influence concrete strength. Therefore, this study aimed at assessing how geological characteristics, surface energy, and surface texture of crushed rock aggregates affect the compressive strength of concrete. The methods used in this study included Petrographic and TIMA analysis, UCS tests, SFE tests and Bond Strength tests. Dolomite, andesite, quartzite, ferro-quartzite and felsite aggregates were used to mix concrete with water-to-cement ratios of 0.4 and 0.6. The surface energy was measured on South Africa's first Contact Angle Meter DMs-401 instrument, and mechanical bond strength was measured using 3-point bending tests. Results show that high mica contents weaken compressive strength, and its influence becomes more prominent as the water-to-cement ratio decreases; low SFE does not always result in high compressive strengths and these energies do not correlate with previous studies performed with different probe liquids; rough surface texture enhances the macro-mechanical bond between aggregate and cement, but detrimental minerals and structural features hinder bond strength from developing. In conclusion, it was found that the compressive strength is dependent on a combined influence of mineral characteristics, structural integrity, surface energy and surface texture. Therefore, fine grain size and rough, intact texture, high mechanical bond, little to no detrimental minerals and structural defects, and low surface energy are the properties that make the most suitable aggregates for high-strength concrete.

Dedication

This dissertation is dedicated to my late grandfather, Dayalan Moodley, who always inspired me to pursue my dreams and strive for excellence. His unwavering belief in the power of education and lifelong learning shaped my journey, and I am forever grateful for the wisdom he imparted and the unconditional love he gave me.

Acknowledgements

The first two people I would like to acknowledge are my supervisors, Dr Nonkuselo Madlakana and Prof. Yunus Ballim. Without them, I would not have started or completed this research study. Their kindness towards me and lessons to ensure I understood every step of the study helped me complete this dissertation as smoothly as possible. Secondly, I would like to extend my gratitude to the Tirisano Foundation for funding my studies, it has been a great honour to be sponsored by such a progressive and benevolent organisation. The next few people I would like to acknowledge are the lab technicians within both schools, Mr Louis Mudalahothe and Mr Sam Tshabalala from the School of Geoscience, and Mr Masindi (Ronny) Lambani from the School of Civil and Environmental Engineering, for assisting in sample preparation and methods. Lastly, I am most grateful to those who provided me with continuous encouragement, love and comfort. My family and friends (Sharona Govender, Sarvesh Govender, Kialan Govender, Tholoana Mabula, Kaydi Govender, Nimisha Padayachee, Shezaan Shaikjee, Vigie Moodley and Cole Israel) have held my spirit high throughout this study which is what pushed me to complete this dissertation to the best of my ability.

Note

Images of all the methods have been included in this dissertation for the convenience of all my readers, regardless of their background – geology or civil engineering. I aspire to write a dissertation that is comprehensive to both fields of study.

Table of Contents

DECLARATION **II**

ABSTRACT **III**

DEDICATION **IV**

ACKNOWLEDGEMENTS **V**

NOTE **V**

LIST OF FIGURES **VIII**

LIST OF TABLES **XVI**

LIST OF EQUATIONS **XIX**

ABBREVIATIONS **XXI**

GLOSSARY **XXV**

CHAPTER 1: INTRODUCTION **1**

CHAPTER 2: BACKGROUND **7**

PART 2.1: GEOLOGICAL BACKGROUND 7

2.1.1. Witwatersrand Supergroup *10*

2.1.2. Ventersdorp Supergroup *11*

2.1.3. Transvaal Supergroup *12*

2.1.4. Bushveld Complex *12*

PART 2.2: CHARACTERISTICS OF CONCRETE 14

2.2.1. Portland cement in concrete *15*

2.2.2. The effects of water in concrete *17*

2.2.3. The effects of admixtures in concrete *18*

2.2.4. Aggregates of South Africa *19*

2.2.5. Effects of aggregate properties on concrete performance *23*

2.2.6. Concrete mixture designs *41*

CHAPTER 3: MATERIALS AND METHODS **45**

3.1. SAMPLE SELECTION AND LOCATION 45

3.2. SAMPLE PREPARATION 47

3.2.1. Thin section preparation *47*

3.2.2. Concrete mixture design and concrete cubes *48*
3.2.3. Thin section offcuts for Sessile Drop test *56*
3.2.4. Rock prisms for the bond strength test *58*
3.3. PETROGRAPHIC ANALYSIS 63
3.4. TIMA ANALYSIS 64
3.5. UNCONFINED COMPRESSIVE STRENGTH (UCS) TEST 66
3.6. SURFACE FREE ENERGY (SFE) ANALYSIS 67
3.7. BOND STRENGTH TEST 71
CHAPTER 4: RESULTS AND DISCUSSION 74
4.1. PETROGRAPHY AND TIMA 75
4.1.1. Dolomite *75*
4.1.2. Andesite *78*
4.1.3. Ferro-quartzite *80*
4.1.4. Quartzite *82*
4.1.5. Felsite *84*
4.2. COMPRESSIVE STRENGTH 86
4.3. SESSILE DROP (SD) METHOD 91
4.3.1. Droplet size determination *91*
4.3.2. Contact angles and SFE of solid aggregates *92*
4.4. BOND STRENGTH TEST 95
CHAPTER 5: COMPARATIVE ANALYSIS OF RESULTS 99
5.1. COMPRESSIVE STRENGTH MEASUREMENTS 99
5.2. COMPARISON OF AGGREGATE MINERALOGY AND COMPRESSIVE STRENGTH 100
5.3. INFLUENCE OF AGGREGATE SURFACE ENERGY ON COMPRESSIVE STRENGTH 103
5.4. EFFECT OF AGGREGATE SURFACE TEXTURE ON COMPRESSIVE STRENGTH 106
CHAPTER 6: CONCLUSION 108
RECOMMENDATIONS 110
REFERENCES 111
APPENDIX A: CONTACT ANGLE METER DMS-401 GUIDE 119
APPENDIX B: MANUAL SFE CALCULATIONS 123
APPENDIX C: MANUAL BENDING STRENGTH CALCULATIONS 127

List of figures

Figure 1.1 Schematic diagram showing that the relationship between the water-to-cement (w/c) ratio and the compressive strength of concrete is inversely proportional (Neville & Brooks, 1987, p.134). 2

Figure 1.2 The average 28-day compressive strength performance of concrete made with three different groups of aggregates at different c/w ratios. Concrete cubes made with different groups of aggregates and the same c/w ratio yield different compressive strengths after 28 days of curing (moderated from Davis and Alexander, 1992). 3

Figure 1.3 The structure of this dissertation. 6

Chapter 2: Background

Figure 2.1 Summary of chapter 2. 7

Figure 2.2 A schematic diagram showing the constituents of concrete and their approximate volumes in concrete (modified from Pedreros et al., 2020). 14

Figure 2.3 Ca-Si-Al ternary diagram for cementitious materials. The material used for this study, Portland cement, is near the Ca-rich corner. Other cementitious materials that are also Ca-rich and hydraulic include slag and calcareous (C) fly ash. Materials that are Si- and Al-rich, as well as pozzolanic, include silica fume, natural pozzolan, siliceous (F) fly ash and metakaolin (modified from Rossen, 2014). 16

Figure 2.4 Schematic diagram of the failure envelope defined by Coulomb's Law of Failure (Gibbs, 2023). 24

Figure 2.5 Schematic diagram showing how cracking may form under shear stress. 26

Figure 2.6 Schematic diagram showing the stress-strain relationship for aggregate, concrete and cement paste (modified from Ghadafi & Kankam, 2022). 27

Figure 2.7 Row 1 – satisfactory failure patterns according to BS 1881-116:1983. Failure patterns labelled 1 to 9 – unsatisfactory failure pattern. Note that T represents the tensile crack (Premakumara, 2020). 29

Figure 2.8 Schematic diagram showing the equilibrium forces described by Young in 1805 between a liquid droplet and a solid surface, in this case, a piece of rock aggregate (modified from Koc & Bulut, 2012). 31

Figure 2.9 Schematic diagram of the 3-point bending test showing the aggregate-cement prism with the load exerted vertically at the interface and the two support points of the system (modified from Gu et al. 2016, p.2). 36

Figure 2.10 Schematic diagram of the bending theory. A – the longitudinal tension and compression forces acting on the surface of the prism that are equal in size but opposite in direction, reversing at the neutral axis (N.A.). B – the bending moment diagram for a 3-point bending test (modified from Gu et al. 2016, p. 2). 37

Figure 2.11 Schematic diagram of the various forms of deterioration that may occur in concrete structures (modified from Gu et al., 2016). *AAR: Alkali-aggregate reaction; ASR: Alkali-silicate reaction; ACR: Alkali-carbonate reaction; CSR: Carbon-silicate reaction. 41

Figure 2.12 A – shaking apparatus to carry out a grading analysis. B – the sieves are mounted from largest at the top to the smallest at the bottom. 42

Chapter 3: Materials and methods

Figure 3.1 Summary of the materials and methods for this study. 45

Figure 3.2 Map of Gauteng and surrounding provinces showing the sample locations, 1 – dolomite, 2 – andesite, 3 – quartzite, 4 – ferro quartzite and 5 – felsite (modified from Htonl, 2008). 46

Figure 3.3 Summary of the sample preparation. 47

Figure 3.4 From left to right is the rock sample, the cut sample and the thin section of felsite. 48

Figure 3.5 Grading analysis for each stone (14 ± 2 mm) aggregate. The nominal aggregate size at 13.2 mm is circled on the graph. This indicates that the K-value is 0.9. 49

Figure 3.6 Grading analysis for each sand aggregate used to determine the fineness modulus. 50

Figure 3.7 The Anton Paar Ultrapyc 3000 instrument used to measure the density of the aggregate samples. 51

Figure 3.8 Compacted bulk density apparatus with dimensions. 52

Figure 3.9 The step-by-step process to measure slump. 54

Figure 3.10 The labelled concrete cubes for rock aggregates felsite (left) and quartzite (right). Each cube was labelled with the authors initials, the initials of the rock aggregate and a number (4 or 6) that represents the w/c ratios 0.4 and 0.6, respectively, as well as the date that the cubes were cast. 56

Figure 3.11 The offcuts from the thin section preparation that were prepared for the Sessile Drop method. From left to right, the image shows the smoothed surfaces, the different thicknesses and the epoxy on the unpolished side of the samples. 57

Figure 3.12 A: each sample was mounted onto a glass plate with Prestik and levelled until the bubble was in the red circle using the apparatus. As the spring was pushed down onto the sample, it became levelled in the Prestik. To ensure the sample did not get scratched during this levelling process, the top of the stamper is covered in a microfibre cloth. The sample was fixed at a levelled position during the Sessile Drop method. B – the levelled sample. 58

Figure 3.13 The felsite and quartzite rock prisms cut with a length of ~160 mm, and widths and heights of ~40 mm. The prisms were marked at 80 mm in length to show

where it would be split. 59

Figure 3.14 Schematic diagram showing the 3-point bending test used to break the aggregate prisms to expose a rough surface. Take note of the 5 mm notch in the aggregate that assisted in breaking the aggregate in a straight, vertical line (modified from Gu et al. 2016, p.2). 60

Figure 3.15 The prisms were broken using the 3-point bending test. A – the prism before breaking; B – the prism after breaking – note the relatively vertical break due to the hardness of the rock and the notch that was cut ~5 mm deep to guide the fracture and break. 60

Figure 3.16 The 5 mm notch that was cut into the prism was painted over with yellow paint and Vaseline to prevent micro-mechanical bonding when moulded against cement paste. Note that the aggregate prism in image C was unintentionally notched greater than 5 mm. *D = dolomite, A = andesite, Aa = andesite with amygdales, FQ = ferro-quartzite, WQ = quartzite, F = felsite. 60

Figure 3.17 The aggregate-cement prisms showing the interface of the two phases in the centre of each prism. 63

Figure 3.18 A – Polarising Microscope; B – Full Section Scanning Microscope. 64

Figure 3.19 A – Carbon-coating instrument; B – Carbon-coated thin section mounted into the TIMA holder; C: TIMA instrument. 65

Figure 3.20 A concrete cube inside the chamber of the compressive strength instrument. 67

Figure 3.21 A – the setup of the Contact Angle Meter DMs-401, alongside the laptop equipped with the FAMAS software. B and C – close-up views of the syringe and needle used to dispense liquid droplets onto the smooth rock surface. 69

Figure 3.22 The measurement sheet for the SFE analysis [Component calculation B], including the solid sample (aggregate) names, the three probe liquids and their respective component values. 70

Figure 3.23 A: the Losenhausenwerk Düsseldorfer Maschinebau compression-tension testing machine showing each of the sectors (compression and tension), the scale and the lever that is used to control the sectors. B: the scale can be arranged in five ways depending on the ROM selected. C: the outer scale is used for the 1/1 and 1/10 ROM, the middle scale for the 1/2 and 1/20 ROM, and the inner scale for the 1/5 ROM. 72

Figure 3.24 A – the dimensions of the base plate and loading plate. B and C – the positioning of the base plate, the prism and the loading plate on the interface of the aggregate-cement prism. 73

Chapter 4: Results and discussion

Figure 4.1 Summary of chapter 4. 74

Figure 4.2 Hand specimen of the dolomite sample showing the dolomite-chert foliation. 75

Figure 4.3 A – PPL image showing complete and partial dolomitization, as well as the rhombohedral-shaped dolomite crystals. B – XPL image showing the high birefringent colours of the dolomite crystals. C – XPL image showing the dolomite-chert layers and the coarser-grained quartz lenses. D – XPL image showing a quartz vein.*Qtz = quartz, Dol = dolomite, Cht = chert. 76

Figure 4.4 A: TIMA image of the dolomite sample showing the dominant dolomite and SiO2-minerals, as well as diopside and minor calcite and mica crystals. B: TIMA image showing the rhombohedral dolomite crystals. 77

Figure 4.5 A – hand specimen of the aphanitic andesite sample. B and C – hand sample of the andesite sample showing the siliceous amygdales and veins. 78

Figure 4.6 A – XPL image showing the homogenous, aphinitic texture of the andesite. B – PPL image showing the quartz veins that run through the andesite. 79

Figure 4.7 TIMA image of the andesite sample showing the homogenous, aphanitic texture. 79

Figure 4.8 Hand specimen of the ferro-meta quartzite. 80

Figure 4.9 XPL image showing the inlocking quartz crystals that give the ferro-quartzite its phaneritic texture, and the scattered musovite mica. *Ms = muscovite. 81

Figure 4.10 TIMA image showing the scattered Fe-rich minerals in the ferro-quartzite. *Hm/Mg = hematite/magnetite. 81

Figure 4.11 A – hand specimen of the quartzite. B – the coarse quartz crystals of the quartzite. 82

Figure 4.12 A – XPL image showing the coarse, unsorted, anhedral quartz grains surrounded by muscovite mica. B – PPL image showing the quartz and muscovite mica. C and D – XPL images showing the polycrystalline quartz. 83

Figure 4.13 TIMA image showing the interconnected pattern of the muscovite mica around the quartz crystals. 84

Figure 4.14 Hand specimen for felsite showing phenocrysts of ~2 mm within a fine-grained groundmass. 84

Figure 4.15 A and B – XPL images showing the coarse feldspar phenocrysts embedded in a fine-grained quartz-rich matrix. C and D – TIMA images showing the feldspar phenocrysts morphed with muscovite mica and calcite. 85

Figure 4.16 The typical failure pattern that most of the concrete cubes followed. Some cubes were not cracked symmetrically, however, the cone shape is present. 88

Figure 4.17 A concrete cube that experienced explosive failure. Broken fragments of concrete are scattered and the cube crumbled upon being removed from the testing machine, leaving no discernible pattern. 88

Figure 4.18 The average compressive strengths for the concrete made with the w/c ratio of 0.4. 90

Figure 4.19 The average compressive strengths for the concrete made with the w/c ratio of 0.6. 90

Figure 4.20 The comparison between tests 1 and 2 for compressive strength of ferro-quartzite concrete cubes made with the 0.6 w/c ratio. 91

Figure 4.21 A: the droplet size (2 μL) and shape for the water and ethylene glycol probe liquids. B: the droplet size (2 μL) and shape for the diiodomethane probe liquid. 92

Figure 4.22 The rate at which water settles on the aggregate surface measured between 1 and 30 seconds with the contact angles. 94

Figure 4.23 The total SFE of the solid aggregates determined using the static contact angles. 95

Figure 4.24 A: the dimensions measured for the smooth-textured surfaces. B: the dimensions measured for the rough-textured surfaces taking into account the notch cut to break the aggregate prism (painted in yellow). 96

Figure 4.25 The mechanical, micro-mechanical and macro-mechanical bonds between each aggregate and cement. 98

Chapter 5: Comparative analysis of results

Figure 5.1 Summary of chapter 5. 99

Figure 5.2 A stacked bar graph showing the mass percentage of minerals that each rock aggregate is composed of. “Other” includes minerals that make up less than 0.01%, as well as any other unclassified minerals. 100

Figure 5.3 The relationship between the mica content present in the aggregate samples and the compressive strength of the concrete. *C/S 0.4 = compressive strength of concrete cubes made the w/c ratio of 0.4; C/S 0.6 = compressive strength of concrete cubes made the w/c ratio of 0.6. 101

Figure 5.4 Scatter plot showing that compressive strength is dependent on mica content in most aggregate types. 102

Figure 5.5 The relationship between the SFE of the aggregate samples and the compressive strength of the concrete. 103

Figure 5.6 Scatter plot showing the incoherent relationship between the compressive strength and the surface free energy. 104

Figure 5.7 The relationship between the compressive strength of concrete and the different bonds that are tested during the bending strength tests. 107

Appendices

Figure A Contact Angle Meter DMs-401 instruction guide, page 1. 120

Figure B Contact Angle Meter DMs-401 instruction guide, page 2. 121

Figure C Contact Angle Meter DMs-401 instruction guide, page 3. 122

List of tables

Preface

Table A Lists of initialisms and their meaning. xxi

Table B Abbreviations used in this study. xxii

Table C Mathematical symbols assigned to various components in this study. xxiii

Table D Accuracy specifications of instruments used in this study. xxiv

Chapter 1: Introduction

Table 1.1 The different groups of aggregates and their respective geological areas used in the Davis and Alexander (1992) experiment. 3

Chapter 2: Background

Table 2.1 A stratigraphic column of the geological units, Witwatersrand Supergroup, Ventersdorp Supergroup, Transvaal Supergroup, and Bushveld Complex, as well as their ages and aggregates (modified from Joubert & Johnson, 1998; Jones, 2003; Fuchs et al., 2017; Rammela, 2020). 8

Table 2.2 The typical mineral compositions of the aggregate types. 20

Table 2.3 The components for each liquid where γLLW is the Lifshitz-van der Waals component, γ^{LAB} is the total Lewis acid-base, γ^{L+} is the Lewis acid component, γ^{L-} is the Lewis base component, and γ^{T} is the total of these energies. 33

Chapter 3: Materials and methods

Table 3.1 The locations and coordinates for the samples 1 to 5. 46

Table 3.2 The fining modulus, relative density, compacted bulk density and stone content for each aggregate. 53

Table 3.3 The trial mixture designs for each aggregate type and each w/c ratio. Each mixture was leballed with a letter(s) that represents the aggregate type and a number (4 or 6) that represents the w/c ratios 0.4 and 0.6, respectively. 54

Table 3.4 The mass of each component in kilograms for a 10-litre concrete mix. *W = water, C = cement, St = stone, S = sand. 55

Table 3.5 The components for the cement paste. The water and cement volumes are calculated using the w/c ratio (0.35), mass and densities. The superplasticiser volume is determined using its density and the cement mass. 62

Chapter 4: Results and conclusion

Table 4.1 The compressive strength results for each age and mixture. In the instance of a malfunction, the measurement was not accurate and a dash (-) is placed. 86

Table 4.2 The average dynamic and static contact angles ($\boldsymbol{\theta}$) for each probe liquid and aggregate measured by the contact angle meter, the Lifshitz-van der Waals and Lewis acid and base components, and the total surface free energy for each solid aggregate. 93

Table 4.3 The bending strength (σ) determined using the failure load (m), the applied load (P), the width (b) and height (d) for the rough-surface prisms. 96

Table 4.4 The bending strength (σ) determined using the failure load (m), the applied load (P), the width (b) and height (d) of the prism for the smooth-surface prisms. 97

Chapter 5: Comparative analysis of results

Table 5.1 The surface free energy results from the Indian Institute of Technology–Madras. 105

Appendices

Table B-1 The components for each probe liquid, where γ^{LLW} is the Lifshitz-van der Waals component, γ^{LAB} is the total Lewis acid-base, γ^{L+} is the Lewis acid component, γ^{L-} is the Lewis base component, and γ^{L} is the total of these energies. 123

Table C-1 The failure load (m), width (b) and height (m) of the aggregate interface. 127

List of equations

Chapter 2: Background

Equation 2.1 Critical shear stress 24

Equation 2.2 Young's equation 31

Equation 2.3 Dupré equation 31

Equation 2.4 Work of adhesion 31

Equation 2.5 Surface free energy components 32

Equation 2.6 Acid-base components of surface free energy 32

Equation 2.7 Work of adhesion considering the acid-base theory 32

Equation 2.8 Young-Dupré equation 32

Equation 2.9 Bending strength 38

Equation 2.10 Bending moment 38

Equation 2.11 Force applied 38

Equation 2.12 Second moment of area 39

Equation 2.13 N.A. to surface equation 39

Equation 2.14 Bending strength simplified 39

Equation 2.15 Fining modulus 42

Equation 2.16 Stone content 43

Equation 2.17 Volume equation 44

Equation 2.18 Sand content 44

Chapter 3: Materials and methods

Equation 3.1 Density equation 50

Equation 3.2 Compressive strength 66

Abbreviations

Table A: Lists of initialisms and their meaning.

AAR	Alkali-aggregate reaction
AAV	Aggregate abrasion value
ACR	Alkali-carbonate reaction
ACV	Aggregate crushing value
AIV	Aggregate impact value
ASR	Alkali-silicate reaction
C-A-S-H	$CaO{-}Al_2O_3{-}SiO_2{-}H_2O$
CBD	Compacted bulk density
CN	Condition number
C-S-H	$CaO{-}SiO_2{-}H_2O$ / calcium silicate hydrates
CSR	Carbon-silicate reaction
c/w	Cement-to-water
FL	Failure load
ITZ	Interfacial transition zone
PC	Portland cement
PPL	Plane-polarised light
ROM	Range of measurement
SCM	Supplementary cementitious materials
SD	Sessile drop
SFE	Surface free energy
TIMA	TESCAN Integrated Mineral Analyser
UCS	Unconfined compressive strength
w/c	Water-to-cement
XPL	Crossed-polarised light

Table B: Abbreviations used in this study.

A	Andesite or Area
Aa	Andesite with amygdales
b	Width of the prism in mm
C	Cement
D	Dolomite
d	Height of the prism in mm
F	Felsite
FQ	Ferro-quartzite
g	Gravitational force
I	Second moment of area of the prisms cross-section
L	Length between support points on the base plate
M	Bending moment
m	Mass
P	Force through mass and gravitational acceleration
Q	Quartzite
S	Sand
St	Stone
T	Tensile crack
V	Volume
W	Water
y	Distance from the neutral axis to the prism surface

Table C: Mathematical symbols assigned to various components in this study.

γ (gamma)	Surface free energy
θ (theta)	Contact angle
ρ (rho)	Density
Σ (sigma)	The sum of…
σ (sigma)	Compressive strength or bending strength
ϕ (phi)	Angle of internal friction
$\tan\phi$	Coefficient of internal friction
γ^{AB}	Acid-base component
γ^{L}	Surface free energy of the liquid
γ^{L+}	Lewis's acid component of the liquid
γ^{L-}	Lewis's base component of the liquid
γ^{LW}	Lifshitz-van der Waals component
γ^{LLW}	Lifshitz-van der Waals component of the liquid
γ^{S}	Surface free energy of the solid
γ^{S+}	Lewis's acid component of the solid aggregate
γ^{S-}	Lewis's base component of the solid aggregate
γ^{SLW}	Lifshitz-van der Waals component of the solid aggregate
σ_N	Normal stress on the concrete cube
σ_o	Cohesive strength
W^{SL}	Work of adhesion

Table D: Accuracy specifications of instruments used in this study.

Instrument	Measurement type	Accuracy	Manufacturer/Model
Optical Microscope	Resolution	0.2 µm	
Full Section Scanning Microscope	Resolution	±0.1 µm to ±1 µm	Olympus
TIMA	Qualitative and quantitative mineralogy	0.01%	TESCAN
Measuring scale	Mass	±0.1 kg	
Ultrapyc 3000	True density	±0.02% (large and medium sample cells)	Anton Paar
		±0.03% (small sample cell)	
Cube Press	Compressive strength	1% of the measured load	Concrete Testing Equipment
Contact Angle Meter DMs-401	Contact angles Surface free energy	±0.2° (contact angle)	Kyowa
		±0.2 mN/m (surface energy)	
Losenhausenwerk Düsseldorfer Maschinebau	Compressive and tensile strength	1% of the measured load	Losenhausenwerk Düsseldorfer Maschinenbau A.G.

Glossary

The following terms are defined in the context of this dissertation:

- Aggregate: granular, insoluble, non-cementitious material, such as stones, used to produce concrete when mixed with water and cement.
- Admixture: chemicals or materials that enhances the concretes properties, such as strength and stability.
- Aphanitic texture: very fine-grained igneous rock with microscopic individual mineral crystals.
- Argillaceous: rocks that contain clay minerals, such as mica, or shale.
- Base plate: the plate that contains two supporting points within the 3-point bending test, on which the prism is centrally positioned.
- Bond strength: the strength that holds different atoms and molecules in a material together.
- Cement-to-water ratio: The less commonly used relationship between cement and water in a concrete mix, which is the mass of cement divided by the mass of water to create a directly proportional relationship.
- Clinker: cement before being ground into powder form and mixed with fine limestone and gypsum.
- Compressive strength: the maximum stress a concrete cube can withstand before reaching its failure.
- Condensed silica fume: a finely divided condensed vapor by-product of the ferrosilicon smelting process.
- Crystal lattice: the micro-structure of an atom or molecule crystal that contains a repeating 3D pattern.
- Curing: the process of preserving the moisture content at a maintained water temperature to stimulate hydration during the early stages in a cement prism or concrete cube.
- Durability: the ability of concrete to withstand rusting and rotting.
- Elastic modulus: the measure of stiffness of a concrete cube or cement prism which is directly proportional to the strength of concrete and cement.
- Fineness modulus: the typical fineness or roughness of an aggregate.
- Fly ash: the by-product of the combustion of crushed, powdered coal, carried by flue gases from the firebox through the boiler.

- Hydration: the chemical reaction that occurs between Portland cement and water.
- Hydrophilic: aggregates that can absorb water.
- Hydrophobic: aggregates that resist water.
- Hydroxyl group: the chemical composition of one oxygen atom and one hydrogen atom bonded covalently (-OH).
- Liberation analysis: the TESCAN Integrated Mineral Analyzer software that incorporates information from energy-dispersive X-ray spectroscopy and backscattered election images to produce quantitative and qualitative data of the mineral composition of a thin section.
- Loading plate: the plate that contains one point within the 3-point bending test, situated on the interface of the aggregate-cement prism, on which the load is applied perpendicular.
- Micro-bleeding: the movement of water rising to the top of concrete after it has been compacted but before it has started to set.
- Mohs hardness scale: the hardness on a scale from 1 to 10 that characterises the scratch resistance of a mineral.
- Mortar: the material composed of cement, sand and water.
- Phaneritic texture: large, interlocking crystals.
- Polycarboxylate-based superplasticiser: a superplasticiser that increases the workability of a concrete or cement paste without increasing the water content.
- Polycrystalline: minerals that consist of multiple small crystals.
- Portland cement: hydraulic cement made from limestone ($CaCO_3$) and a silica-rich material, such as clay.
- Porphyritic texture: the texture of an igneous rock that includes larger crystals within a fine-grained or glassy matrix.
- Pozzolan: a siliceous-aluminous or just siliceous material that has minimal cementitious properties on its own, but in its finely divided form with water, it reacts with calcium hydroxide at ordinary temperatures to form compounds with cementitious characteristics.
- Probe liquid: the selected liquids used for the Sessile Drop method that have known surface free energy components.
- Shrinkage: the volume reduction of a concrete cube due to a loss of water.
- Slump: a measure of consistency of freshly mixed concrete that uses the distance that fresh concrete moves downwards from a reference point.
- Strain: the deformation of a concrete cube due to stress.
- Stress: force applied per unit area on a concrete cube.

- Superplasticiser: additives or admixtures used to make high-strength concrete by acting as water reducers.
- Tensile strength: the greatest stress an aggregate-cement prism can withstand before breaking under a pulling force.
- Water-to-cement ratio: The more commonly used relationship between water and cement in a concrete mix, which is the mass of water divided by the mass of cement to create an inversely proportional relationship.
- Wettability: the ability of a droplet of liquid maintaining its contact with a solid aggregate surface, characterised by the contact angles measured using the Sessile Drop method.
- Workability: the ease at which concrete can be mixed, placed, compacted and set without losing its uniformity.

Chapter 1: Introduction

Concrete is one of the most widely used construction materials globally, valued for its strength and durability. While the water-to-cement (w/c) ratio has long been considered the primary determinant of compressive strength, recent studies suggest that aggregate properties also play a significant role. Understanding how different aggregates influence compressive strength is crucial for optimizing concrete performance, improving structural integrity, and reducing environmental impacts. This study aims to assess how geological characteristics, surface texture, and surface energy of crushed rock aggregates affect the compressive strength of concrete.

Concrete consists of a binding agent, such as a Portland cement (PC) based binder, in specific proportions with water and various-sized aggregates, including sand and crushed rock (Alexander and Mindess, 2005). During concrete formation, cement undergoes a chemical reaction with water in a process called hydration (John and Lothenbach, 2023). Over a curing period, this reaction binds the aggregates together, forming the solid, cohesive mass known as concrete. Compressive strength develops during this time frame and continues to grow at a decreasing rate after 28 days (Haist et al., 2021). By altering component proportions, incorporating property-enhancing additives (admixtures), and using different aggregate types, concrete can be customized for various applications (Alexander and Mindess, 2005; Chen et al., 2024).

The quality of concrete is primarily assessed by its compressive strength, a fundamental physical property. Compressive strength is relatively easy to measure and serves as an approximate indicator of other mechanical properties, such as tensile and shear strength and elastic modulus (Owens, 2009). It also provides insight into the impermeability and durability of concrete, making it a suitable measure for evaluating constituent materials (Ballim, 1983).

Ballim (1983) discussed the technological advancement made by Duff Abrams in 1918. Abrams stated that the proportion of water to cement used in concrete, or the w/c ratio, is the only variable to influence concrete compressive strength, provided that the material composition and testing conditions remain constant. These control variables included cement type, compaction and curing time, but excluded aggregate type. Abrams concluded that

compressive strength of concrete is inversely proportional to the w/c ratio (Figure 1.1), a principle still accepted today (Davis and Alexander, 1992). However, his assertion that the w/c ratio is the sole determining factor has been challenged by subsequent research. Previously, aggregates were considered inert based on Abram's theory, but it is now understood that aggregate properties significantly influence the physical characteristics of hardened concrete (Alexander and Mindess, 2005; Chen et al., 2024).

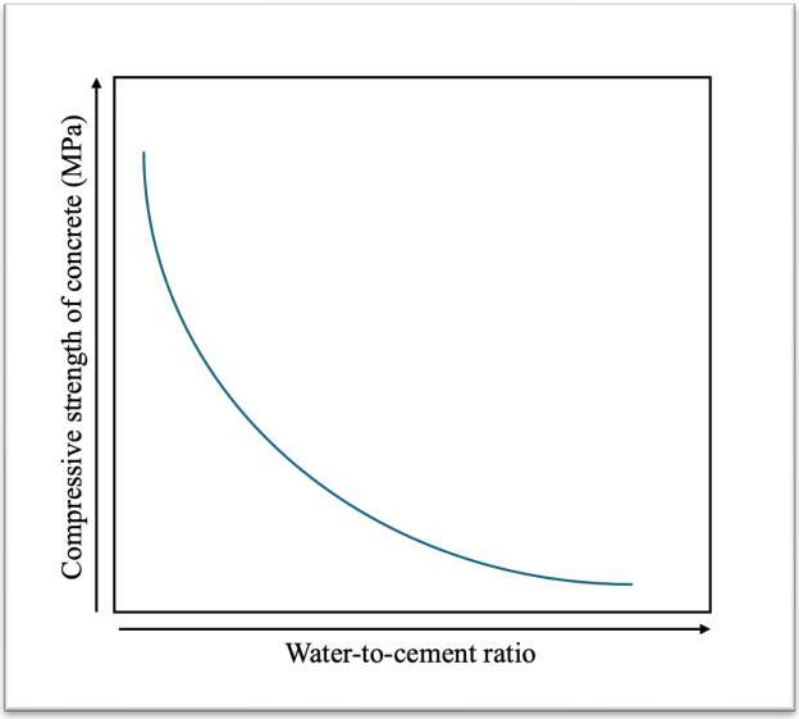


Figure 1.1: Schematic diagram showing that the relationship between the water-to-cement (w/c) ratio and the compressive strength of concrete is inversely proportional (Neville and Brooks, 1987, p.134).

Further studies (e.g. Davis and Alexander, 1992), investigated the influence of cement-to-water (c/w) ratio and different aggregate types on compressive strength. Davis and Alexander (1992) plot the compressive strength against the unconventional c/w ratio creating directly proportional trends (Figure 1.2), opposed to the curve in Figure 1.1 which shows the relationship between compressive strength and w/c ratio. Their experiment used the same PC and c/w ratios but varied the aggregate types to test concrete over a 28-day curing duration, revealing significant differences in compressive strength (Figure 1.2). The aggregates used in their experiment are listed in Table 1.1.

Table 1.1: The different groups of aggregates and their respective geological areas used in the Davis and Alexander (1992) experiment.

Group	Aggregate rock type	Locality
1	Andesite	Eikenhof
	Dolerite	Ngagane and N. Crushers
	Quartzite	Mossel Bay and Coedmore
	Felsite	Zeekoewater
	Siltstone	Leach and Brown
2	Dolomite	Olifantsfontein
	Greywacke	Malmesbury Shale, Peninsula
3	Wits quartzite	Vlakfontein
	Quartzite	Ferro
	Granite	Jukskei and Rheebok

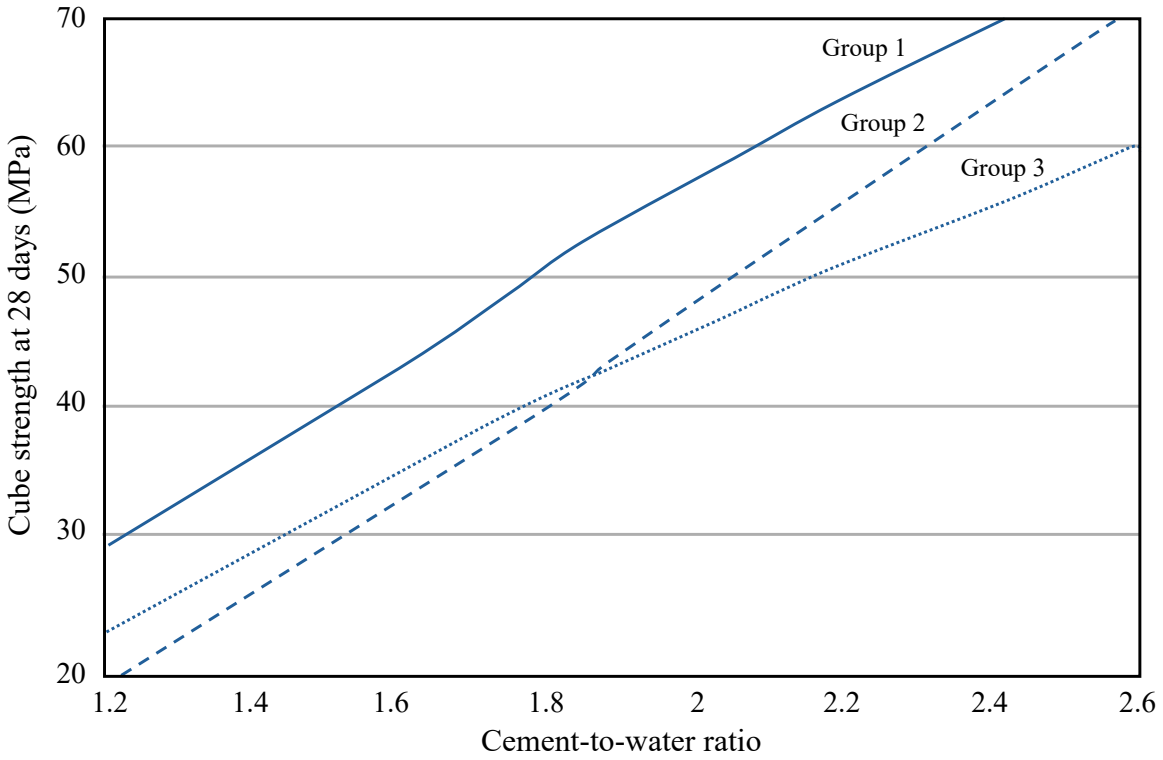


Figure 1.2: The average 28-day compressive strength performance of concrete made with three different groups of aggregates at different c/w ratios. Concrete cubes made with different groups of aggregates and the same c/w ratio yield different compressive strengths after 28 days of curing (moderated from Davis and Alexander, 1992).

The graph (Figure 1.2) demonstrates how different aggregates influence compressive strength at the same c/w ratios. To isolate the effect of aggregate properties, the c/w ratio was controlled as the independent variable. The trends in compressive strength variation suggest that different aggregate properties, such as surface texture and mineral composition, impact strength outcomes. Notably, at lower c/w ratios, aggregates from groups 2 and 3 exhibit similar performance. However, as the c/w ratio increases, the performance gap between those groups widens. Davis and Alexander (1992) also found intra-group variation, such as andesite yielding higher compressive strengths compared to dolerite within Group 1. The Davis and Alexander (1992) study is used as a base for which this research study is built on. However, the inverse of c/w ratio is used in this study – the w/c ratio. Therefore, any graphs depicting the relationship between compressive strength and w/c ratio in this research study will be inversely proportionate as shown in Figure 1.1.

While the w/c ratio is a critical factor in concrete strength, the above experimental results indicate that concrete made with different aggregates, but identical w/c (or c/w) ratios exhibit varying compressive strengths (Ballim, 1983; Davis and Alexander, 1992). Therefore, the w/c ratio is not sufficient on its own to determine the compressive strength of concrete. Rather, aggregate properties significantly influence strength, particularly the interface between the aggregate and the cement paste, i.e. the nature and quality of the surface of the aggregate. It is important to note that this study will be using the more conventional w/c ratio form instead of the c/w ratio form.

Given the significance of aggregates in concrete performance, there are three key benefits. The first benefit relates to the reduction of movement when hardened cement pastes exhibit shrinkage, elastic deformation, and creep under load. Hooke's Law states that strain is proportional to stress within elastic limits. This viscous and elastic movement of solid cement is dimensionally unstable and not functional for building constructions. The addition of aggregates assists in stiffening the concrete by diluting its elastic and time-dependent movement capacity. The concrete does not become resistant to these movements. However, the impact of these movements does become tolerable for the structural behaviour of the concrete. The second benefit relates to the reaction of heat. The cement hydration process is exothermic. Therefore, construction exclusively composed of cement and water release large amounts of heat which can lead to thermal cracking. Aggregates, having lower thermal conductivity than cement paste, help dissipate heat, reducing the likelihood of thermal damage. The third and last

benefit relates to the reduction of CO_2 emissions. The manufacture and transportation of cement is financially and environmentally costly. Therefore, cement production generates substantial CO_2 emissions. Increasing aggregate content reduces cement demand, thereby minimizing environmental impact (Owens, 2009).

This study hypothesizes that the nature and quality of the aggregate surface affects compressive strength. Specifically, surface energy and surface texture are key parameters governing the bond between cement paste and aggregate. Matsushita and Onoue (2006) found that compressive strength is inversely proportional to aggregate surface energy due to micro-crack formation, an effect exacerbated by higher w/c ratios. Additionally, Ballim (1983) observed that andesite aggregates yielded higher compressive strengths than quartzite aggregates, attributing this to the more coarse and intact surface texture of andesite, which enhances mechanical interlock (Alexander and Mindess, 2005; Chen et al., 2024).

Given the widespread use of concrete in infrastructure, understanding the impact of different rock types on its strength and durability is crucial. This study aims to assess how geological characteristics, surface texture, and surface energy of crushed rock aggregates affect the compressive strength of concrete. The research will employ Petrographic analysis, TESCAN Integrated Mineral Analyser **(**TIMA) analysis, Unconfined Compressive Strength (UCS testing, Surface Free Energy (SFE) testing and Bond Strength testing to achieve its objectives:

1. **Petrographic analysis** and **TIMA analysis** to determine mineral assemblage and textural characteristics of the aggregate samples, as well as the hydrophilicity of the sample surfaces.
2. **UCS test** to measure the physical strength of concrete.
3. **SFE test** using a Contact Angle Meter to evaluate the interaction between the aggregate and other materials, such as water.
4. **Bond strength test** to assess the texture and mechanical interaction between cement and aggregate.

Five rock aggregates were selected for this study. Four from Davis and Alexander (1992): Group 1 andesite and felsite (igneous rocks) and Group 3 quartzite and ferro-quartzite (metamorphic rocks); and one additional sedimentary rock, the Lyttelton Formation dolomite. These selections were based on geological diversity (igneous, metamorphic, and sedimentary),

availability, and prior use as concrete aggregates. The selected aggregates have been tested for suitability in previous studies, considering properties such as relative density, bulk density, water absorption, thermal expansion, strength, stiffness, and alkali-aggregate reactivity (AAR) (Davis and Alexander, 1992). The igneous rock andesite, for example, primarily comprises plagioclase feldspar, orthopyroxene, clinopyroxene and magnetite (Hutchison, 2005). Its dense mineralogy and compact texture contribute to its strength and stability as an aggregate, while its resistance to alkali reactions make it suitable for long-term structural applications (Davis and Alexander, 1992).

By integrating petrographic analysis with mechanical testing, further investigation into these materials will provide valuable insights into optimizing concrete performance for various geoscience and engineering applications. However, there are limitations to this study, such as testing only five aggregates preselected within the region of Gauteng and Mpumalanga, using only PC as a binding agent, using only two w/c ratios (0.4 and 0.6), and learning and working with a new instrument, the *Contact Angle Meter DMs-401*, that will further be discussed in Chapter 3: Materials and Methods.

This dissertation is structured as shown in Figure 1.3:

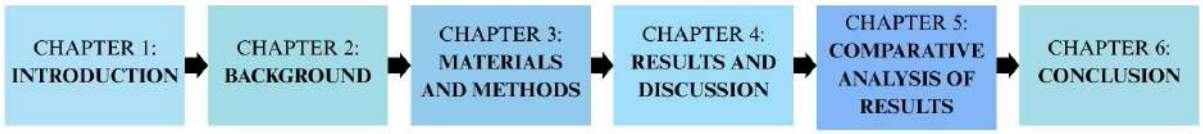


Figure 1.3: A flow diagram showing the structure of this dissertation.

Chapter 2: Background

Chapter 2 is separated into two parts: Part 2.1, which dives into the geological background of the aggregates; and Part 2.2: which characterises the components and properties of concrete (Figure 2.1).

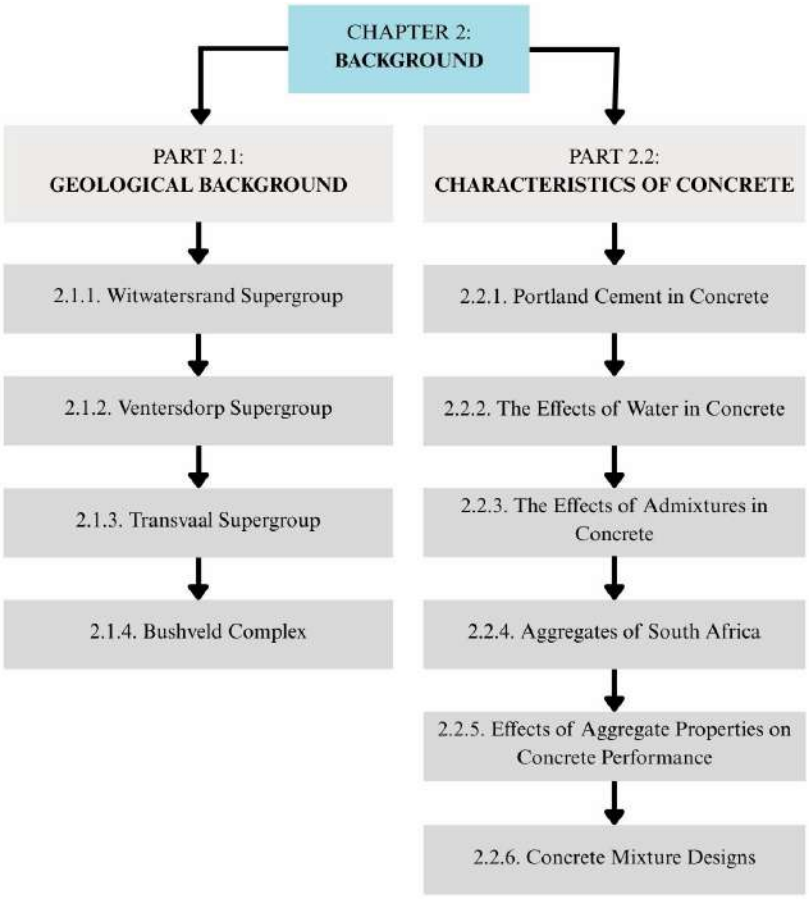


Figure 2.1: A flow diagram showing the structure of Chapter 2.

Part 2.1: Geological background

Four of the five sample aggregates used in this study were sourced from various geological units around Gauteng, while the fifth sample aggregate was sourced from Mpumalanga. Key units include the Witwatersrand Supergroup, known for its quartzite; the Ventersdorp Supergroup, which provides andesite; the Transvaal Supergroup, which contains dolomite and ferro-quartzite; and the Bushveld Complex, which supplies felsite. Table 2.1 provides a summary of these stratigraphic units. The following sections offer a detailed overview of each geological unit, arranged from oldest to youngest.

Table 2.1: A stratigraphic column of the geological units, Witwatersrand Supergroup, Ventersdorp Supergroup, Transvaal Supergroup, and Bushveld Complex, as well as their ages and aggregates (modified from Joubert and Johnson, 1998; Jones, 2003; Fuchs et al., 2017; Stamsnijder, 2017 and Rammela, 2020).

Age (Ma)	Supergroup	Group	Subgroup	Formation	Aggregate
2050	Bushveld Complex	Rooiberg			Felsite
		Pretoria		Houtenberg	
				Steenkampsberg	
				Nederhorst	
				Lakenvalei	
				Vermont	
				Rayton	
				Magaliesberg	Ferro quartzite
				Silverton	
				Daspoort	
2500 – 2100	Transvaal			Strubenkop	
				Dwaalheuwel	
				Hekpoort	
				Bospoort	
				Timeball Hill	
				Rooihoogte	
		Chuniespoort		Duitschland	
				Penge	
			Malmani	Frisco	
				Eccles	
				Lyttelton	Dolomite
				Monte-Cristo	
				Oaktree	
2620 – 2300	Ventersdorp	Pneil		Allanridge	
				Bothaville	
		Platberg		Rietgat	
				Makwassie	
				Langgeleven	Andesite
				New Kameeldoorns	

		Klipriviersberg		Edenville	Quartzite
				Loraine	
				Orkney	
				Alberton	
				Venterspost Conglomerate	
2800 – 2300	Witwatersrand	Central Rand	Turffontein	Mondeor	
				Elsburg	
				Kimberley	
			Johannesburg	Booysens Shale	
				Krugersdorp	
				Luipaardsvlei	
				Randfontein	
				Main	
				Blyvooruitzicht	
		West Rand	Jeppestown	Maraisburg	
				Roodepoort	
				Crown	
				Babrosco	
				Rietkuil	
				Koedoesdlaagte	
			Government	Afrikander	
				Elandslaagte	
				Palmietfontein	
				Tusshenin	
				Coronation	
				Promise	
			Hospital Hill	Bonanza	
				Brixton	
				Parktown	
				Orange Grove	
>2800		Dominion			
	Basement				

2.1.1. Witwatersrand Supergroup

The Witwatersrand Supergroup is an Archean-aged geological formation forming part of the Witwatersrand Triad alongside the Ventersdorp Supergroup and the Dominion Group (Bowen et al., 1986; Altermann and Lenhardt, 2012). Situated on the Kaapvaal Craton, this supergroup significantly contributes to the sedimentary Witwatersrand Basin (Burke, 1986; Altermann and Lenhardt, 2012). Although its exact age is debatable, the Witwatersrand Supergroup is dated between the Ventersdorp Supergroup (2620–2300 Ma) and the Dominion Group (>2800 Ma) (Bowen et al., 1986; Paprika et al., 2024). The length of the basin and its northeast-trending formation align with a tectonic event approximately 2700 Ma, when the Kaapvaal and Zimbabwe Cratons collided, forming a foreland basin as a result of the lithospheric flexure from peripheral loading and compression of the rock. This formation comprises two main groups, the West Rand and Central Rand, which primarily contain clastic sedimentary sequences overlying the Dominion Group (Burke, 1986; Paprika et al., 2024).

The West Rand Group is deposited over a larger area compared to that of the Dominion Group (Burke, 1986; Paprika et al., 2024), and includes the Jeppestown, Government and Hospital Hills Subgroups. The Jeppestown Subgroup comprises the Koedoeslaagte, Rietkuik, Babrosco, Crown, Roodepoort and Maraisburg Formations, and contains greywacke, dolerite, shale, quartzite, mafic lava, conglomerate and diamictite at its base. The Government Subgroup comprises the Promise, Coronation, Tusschenin, Palmietfontein, Elandslaagte and Afrikander Formations, and contains quartzite, dolerite, shale, greywacke and conglomerate. The Hospital Hill Subgroup comprises the Orange Grove, Parktown, Brixton and Bonanza Formations, and contains minor conglomerate and subequal shale and quartzite (Joubert and Johnson, 1998; Stamsnijder, 2017). The Orange Grove Formation provided the coarse-grained quartzite for this study, which is the product of intense diagenesis and low-grade metamorphism of a quartz-rich sandstone deposited in an ancient fluvial-deltaic environment. The formation features mature quartzites and pale green fuchsite associated with detrital chromite, suggesting an ebb-dominated tidal environment. The quartzite is composed primarily of interlocking quartz grains with minor feldspar and lithic fragments, and exhibits conchoidal fracture, as well microfractures due to tectonic overprinting (Burke, 1986; Altermann and Lenhardt, 2012).

The Central Rand Group, which comprises the Johannesburg and Turffontein Subgroups (Joubert and Johnson, 1998; Stamsnijder, 2017), has greater stratigraphic thicknesses towards

the centre of the basin. This shows evidence of tectonic activity, igneous intrusions, and erosional alterations, especially along its southeastern margin. In the northwest, thrust faults and greenschist facies minerals indicate low-grade metamorphism, contributing to the unique geology of the basin and its rich gold deposits, especially north of Johannesburg (Burke, 1986; Phillips et al., 2024). More specifically, the Johannesburg Subgroup comprises the BIyvooruitzicht, Main, Randfontein, Luipaardsvlei, Krugersdorp and Booysens Shale Formations, and contains quartzite, dolerite, conglomerate, diamictite, shale and amygdaloidal lava. The Turffontein Subgroup comprises the Kimberley, Elsburg and Mondeor Formations, and contains quartzite and conglomerate (Joubert and Johnson, 1998; Stamsnijder, 2017).

2.1.2. Ventersdorp Supergroup

The Ventersdorp Supergroup, also part of the Witwatersrand Triad, developed after the Kaapvaal Craton stabilized around 3000 Ma. This sequence comprises sedimentary and volcanic rocks, forming a thick, faulted layer that lies atop the gold-bearing Witwatersrand Supergroup. The debated age range for the Ventersdorp Supergroup is between 2620 and 2300 Ma (Bowen et al., 1986; Altermann and Lenhardt, 2012). The supergroup is divided into the Klipriviersberg, Platberg and Pniel Groups and contains basalt, andesite, quartz/feldspar porphyry, tuff and agglomerate volcanic rocks and conglomerate, shale and sandstone sedimentary rocks (Joubert and Johnson, 1998; Stamsnijder, 2017). Key formations within the Klipriviersberg Group include the Venterspost Conglomerate Formation which separates the Ventersdorp Supergroup from the underlying Witwatersrand Supergroup (Bowen et al., 1986; Altermann and Lenhardt, 2012), as well as the Alberton, Orkney, Loraine and Edenville Formations. The Platberg and Pniel Groups include the New Kameeldoorns, Langgeleven, Makwassie, Rietgat, Bothaville and Allanville Formations (De La and Winter, 1976; Altermann and Lenhardt, 2012). The Langgeleven Formation consists of the andesite used in this study. The andesite originates from volcanic eruptions during the Paleoproterozoic era, associated with rifting events. It is fine-grained with phenocrysts of pyroxene and plagioclase set in a fine crystalline groundmass. Alteration minerals within the andesite include chlorite and epidote from hydrothermal processes, as well as albite, amphibole, and magnetite. The andesite displays amygdaloidal textures, vesicles and silica-rich clasts, adding to its structural diversity (Alexander and Ballim, 2011).

2.1.3. Transvaal Supergroup

The Transvaal Supergroup spans the late Archean to early Proterozoic eras, with formations in the Transvaal Basin covering 140,000 km^2 (Eriksson et al., 1991). Its two primary subdivisions, the Chuniespoort and Pretoria Groups, provide significant geological insights. The Chuniespoort Group contains the Malmani Subgroup with Oaktree, Monte-Cristo, Lyttelton, Eccles, Frisco, Penge and Duitschland Formations, comprising predominantly dolomite and subordinate chert, as well as limestone, banded iron and minor carbonaceous shale. Of particular interest, the Lyttelton Formation, which supplied dolomite for this study, is characterized by a 120 to 290 m (Joubert and Johnson, 1998) thick dolomite layer with stromatolites that weathers to a distinct dark brown colour. This suggests the dolomite formed within a shallow marine environment and had undergone diagenesis that includes chert nodules and recrystallisation. The rock is primarily composed of the mineral dolomite, with significant porosity and the potential for dissolution features such as vugs and micro-cavities. It often contains stylolites and secondary calcite veins, which may act as planes of weakness (Rammela, 2022).

The Pretoria Group, which serves as the base of the 2050 Ma Bushveld Complex, includes lacustrine and deltaic deposits containing quartzite, shale and andesitic basaltic lava. This ~7000 m thick group comprises the Rooihoogte, Timeball Hill, Boshoek, Hekpoort, Dwaalheuwel, Strubenkop, Daspoort, Silverton, Magaliesberg, Rayton, Vermont, Lakenvalei, Nederhorst, Steenkampsberg and Houtenbek Formations (Joubert and Johnson, 1998). The Magaliesberg Formation, containing quartzite and shale, is of particular interest as it is the source of the ferro-quartzite aggregate utilized in this study. It is a silica-rich, iron-bearing sedimentary rock, often derived from feldspathic sandstones. It contains iron-oxides that produce a dark hue and magnetic properties, a tightly-packed intergranular texture, and secondary structures such as joints and veins, which influence fracture behaviour and permeability (Eriksson et al., 1991).

2.1.4. Bushveld Complex

Located in the northern sector of the Karoo Basin, the Bushveld Complex is a prominent geological formation known for its mineral wealth, especially in platinum group metals (Du Plessis, 2008). It contains acidic, basic and ultrabasic intrusive rocks (Joubert and Johnson, 1998). The Bushveld Complex intruded into the Transvaal Supergroup, creating a layered

structure characterized by valleys and ridges that formed by ancient volcanic and tectonic activities (Eriksson et al., 1991). The extensive mineral deposits and unique geological features of this region, shaped by the surrounding Kaapvaal Craton and Cape Fold Belt, add significant geological value to the mineral wealth of South Africa (Du Plessis, 2008). The complex comprises the Rustenburg Layered Suite, Rashoop Granophyre Suite, Lebowa Granite Suite (Joubert and Johnson, 1998), and the Rooiberg Group that forms the top of the complex. The Rooiberg Group overlays the Transvaal Supergroup and contains basaltic andesite, minor shale, agglomerate, and felsite. This felsite was mined as aggregate and used for this study. It is fine-grained and contains quartz and feldspar microlites in a silica-rich matrix, typically of rhyolitic to dacitic composition, with flow banding or spherulitic textures. Fractures and joints formed during cooling are common and influence particle strength and shape (Eriksson et al., 1991).

Understanding the geological background of the rocks facilitates the identification of aggregate properties and their impact on concrete. Subsequently, a comprehensive review of concrete and aggregate characteristics are presented in the following Part 2.

Part 2.2: Characteristics of concrete

Concrete consists of cement, water, often admixtures and aggregates (Figure 2.2) (Alexander and Mindess, 2005; Chen et al., 2024). Cement is a fine, grey-coloured powder material used together with water as the binding agent within concrete. Various cementitious materials are available around South Africa, such as PC, pre-mixed PC with supplementary cementitious materials (SCM), and specialty cements designed for plaster and mortar applications. SCMs that conform to SANS-standards include fly ash (FA), ground granulated blast furnace slag (GGBS), and condensed silica fume (CSF) (Grieve, 2009). Admixtures are chemicals or materials that may be in the form of powders or liquids. These chemicals are specially designed to enhance specific properties in concrete, such as strength and stability (ASTM International, 2020). Aggregates are crushed natural rock, which were once thought of as a filler material, but are now crucial in concrete manufacture. This material may be in the form of sand (fine aggregate) or various sized stone (coarse aggregate) and acts as diluents to the cement paste. It makes up approximately 60 to 80% of the concrete volume and improves stability and durability of the concrete, impacting the physical attributes, such as compressive strength of cured concrete (Grieve, 2009).

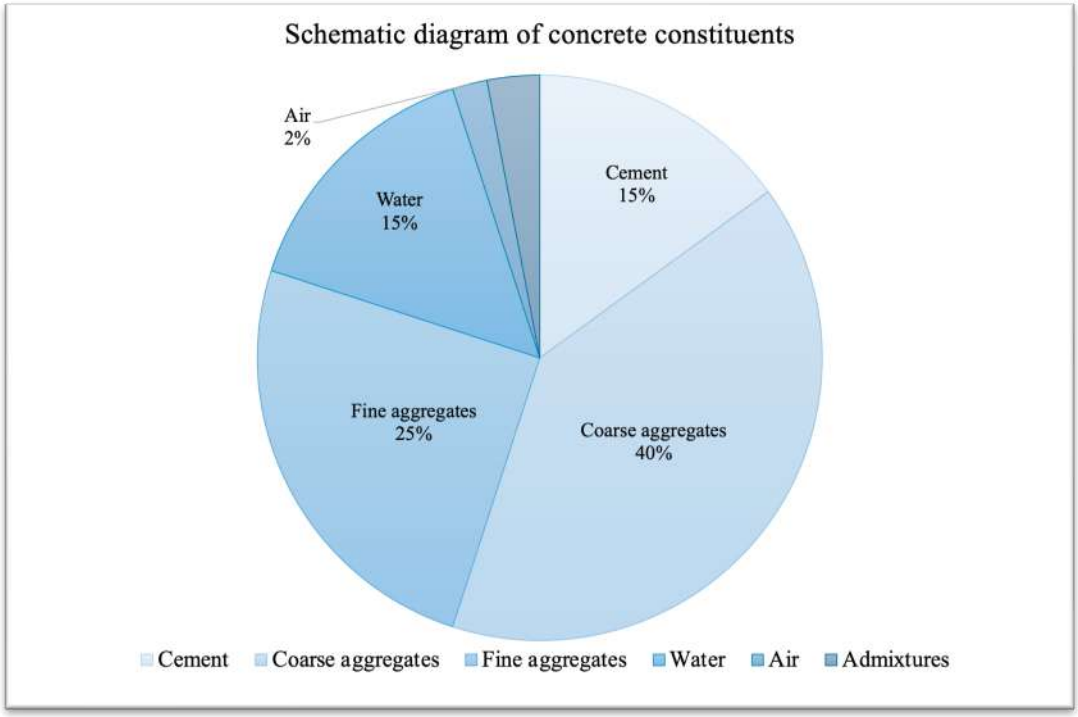


Figure 2.2: A schematic diagram showing the constituents of concrete and their approximate volumes in concrete (modified from Pedreros et al., 2020).

In this study, the following components were used to prepare samples for various testing methods:

1. PC, water, five different rock aggregates (dolomite, andesite, quartzite, ferro-quartzite and felsite) and their respective sands were used to make concrete cubes for the UCS tests.
2. PC, water and a plasticising admixture (Sika Visococrete-3088) were used to make cement paste to mould against rock prisms for the bond strength tests.

2.2.1. Portland cement in concrete

Cement is commonly described as the adhesive or binding agent in concrete. With a 9000-year history, cementitious materials are the most ancient manmade building material. PC is the second most frequently used building material globally (after water), surpassing the usage of asphalt, wood and steel (Alexander and Mindess, 2005). PC is primarily composed of clinker, a mixture of phases such as tri-calcium silicate or alite (C_3S), dicalcium silicate or belite (C_2S), aluminate (C_3A), and ferrite (C_4AF) (Neville and Brooks, 1987; Rossen, 2014). These phases react with water during hydration to form a binding matrix that strengthens the concrete by holding particles together (Alexander and Mindess, 2005; Chen et al., 2024). Hydration is stimulated during the early stages of concrete strength development through curing, which is the process of preserving the water available for hydration reactions in concrete or cement at a maintained water temperature.

Cementitious materials are available in different forms depending on their composition. Figure 2.3 shows the composition of various cementitious materials. It illustrates how PC and SCM like fly ash and slag contribute to hydration products, such as calcium silicate hydrate (C-S-H) and calcium hydroxide (CH) phases which form due to the reactions between alite and belite with water (Rossen, 2014; Haist et al., 2021). In Figure 2.3, C-A-S-H ($CaO{-}Al_2O_3{-}SiO_2{-}H_2O$) are the primary minerals that make up cementitious materials, along with SCM.

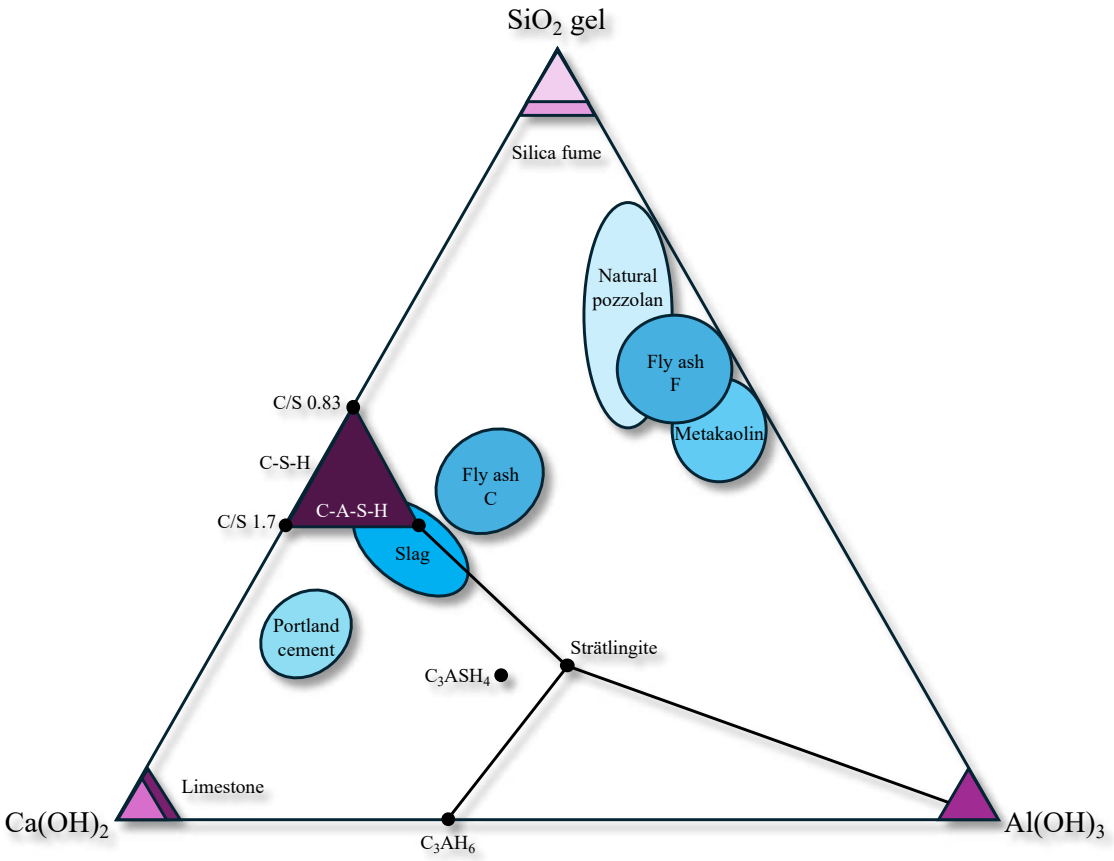


Figure 2.3: Ca-Si-Al ternary diagram for cementitious materials. The material used for this study, Portland cement, is near the Ca-rich corner. Other cementitious materials that are also Ca-rich and hydraulic include slag and calcareous (C) fly ash. Materials that are Si- and Al-rich, as well as pozzolanic, include silica fume, natural pozzolan, siliceous (F) fly ash and metakaolin (modified from Rossen, 2014).

Concrete made with PC can be engineered to possess specific strengths and durability (Grieve, 2009). The strength of concrete and cement grows over the curing period and PC exhibits representative strength development in concrete over specific curing durations. After 7 days of curing, the compressive strength of the concrete and cement serves as a critical reference point in evaluating early-stage strength development and establishes the quality of the concrete mixture. Depending on the w/c ratio, aggregate and cement type, and curing conditions, approximately 65% (Mishra, 2014) of strength has developed at this point. After 28 days of curing, the strength of the concrete is widely recognised as the critical period for reaching the hydration peak of the cement and directly impacts how the mechanical properties of concrete or cement develop (Haist et al., 2021). Alexander (1994) explained that during a curing period

of 28 days, major changes in the properties of the concrete and cement paste occur due to the hydration reactions that take place. These changes improve durability and increase strength (Mishra, 2014). When this 28-day period is reached, a decrease in the rate of property improvement tends to occur and changes thereafter are less pronounced (Alexander, 1994; Chen et al., 2024). Therefore, the 28-day curing period serves as a benchmark in assessing the structural performance of concrete or cement and captures the critical strength development. As mentioned, the rate of strength improvement decreases after 28 days, however, this does not mean that the strength does not continue to grow. At day 56, the strength is tested in this study to show the decreasing rate of improvement; results are expected to show only small increases in strength. PC is the favoured cementitious material because of its cost-effectiveness, its capacity to set underwater when necessary, and its ability to set and harden at standard pressures and temperatures in a relatively short period.

Additional information regarding the different cementitious materials, and the segments labelled C-S-H and C-A-S-H in particular (Figure 2.3), are covered in Rossen's 2014 thesis titled '*Composition and morphology of C-A-S-H in pastes of alite and cement blended with supplementary cementitious materials'* (Rossen, 2014).

2.2.2. The effects of water in concrete

In a concrete mixture, enough water for a specific mixture design ensures that all the aggregates are sufficiently covered in cement paste. The amount of water in a mixture is determined by the w/c ratio, which is the quotient between the mass of water and the mass of cement, necessary to provide the required strength at a specified concrete age. Most w/c ratios range between 0.4 and 0.6 (Vu et al., 2009). A lower w/c ratio, such as 0.4, indicates less water in the mixture, therefore a higher proportion of cement and a higher compressive strength of the concrete. Some aggregate characteristics, such as the grading and the maximum size, influence the w/c ratio and workability. Larger aggregate sizes require less water for a given workability, while smaller aggregates have a more prominent effect on workability (Alexander and Mindess, 2005).

Water quality is an important factor as contaminated water can disrupt hydration, affecting the concrete strength. Contaminants and impurities in both the mixing water and the moisture on the aggregate surface should be accounted for by using appropriate water and air drying

processes on all aggregates before mixing. Different types of waters, including aggressive and mixing water, affect hardened concrete differently. Aggressive waters, known to be soft (low levels of dissolved minerals) and acidic, are not hazardous during mixing (Neville and Brooks, 1987; Haist et al., 2021) but can lead to the corrosion of reinforcing steel which will affect the strength of the concrete. Mixing water used in concrete should be free from impurities and safe to drink (Roxburgh, 2021), therefore should not contain dissolved solids greater than 1000 parts per million (ppm). Nevertheless, water that is suitable for drinking may not always be suitable for mixing concrete, especially if there are high levels of sodium (Na) and/or potassium (K) which cause alkali-aggregate reactions (AAR). Other unsuitable waters include those with organic acids which affect the hardening process of concrete, and algae which reduces concrete strength due to air entrainment. Water that is acceptable for mixing concrete include those with a pH range of 6 to 8, little salt content and natural acidity (Dooner, 2019). Therefore, the quantity and quality of water in a mixture directly affects the workability and strength of the concrete.

Clean, drinking water generally requires no testing as it conforms to the SANS 51008 requirements (Roxburgh, 2021). Therefore, tap water was used to make the concrete and cement paste in this study.

2.2.3. The effects of admixtures in concrete

There are various admixtures for different purposes in concrete. Different admixtures are used to enhance the air entrainment or detrainment, to accelerate the setting time (ASTM International, 2020), to improve the workability or to increase the strength of concrete. The type of admixture that was used in this study to prepare samples for the bond strength tests is a polycarboxylate-based superplasticiser called Sika Viscocrete 3088 (Sika South African (Pty) Ltd., 2020). Plasticisers and superplasticisers are types of admixtures that enhance the workability of a mixture without increasing the w/c ratio (Martin, 2006). This yellowish, aqueous solution (Sika South African (Pty) Ltd., 2020) works as a water-reducing admixture that increases the flow of the cement paste used to prepare the samples for the bond strength tests. This was necessary so that the paste runs smoothly into the grains of the aggregate. The density (1.05 kg/L) and recommended dosage (0.2-1.5% of the cement weight) (Sika South African (Pty) Ltd., 2020) of the admixture is important to calculate the appropriate amount of solution needed to prepare the cement paste.

2.2.4. Aggregates of South Africa

Aggregates are the granular mineral components of concrete that are made up of fine and coarse pieces of natural rock and account for 60 to 80% of the mass of concrete. Aggregates are vital in concrete production due to their influence on economic and financial alleviation, durability, compressive strength, and overall stability (Alexander and Mindess, 2005; Owens, 2009). In South Africa, aggregates are sourced from a variety of geological formations, each imparting unique properties to the concrete. Natural aggregates, i.e. rocks, originate from various sources, such as land and sea deposits, gravel pits, rock quarries, sand dunes and riverbeds; and come in different forms, such as crushed or uncrushed gravel, crushed stone, and sand. Their properties, such as relative density, strength, stiffness, hardness, permeability, porosity, chemical composition, and crystal structure, are derived from the physical and chemical properties of their parent rocks and determine the processes (breaking or crushing) they must undergo to become viable engineering materials or aggregates (Alexander and Mindess, 2005; Chen et al., 2024). Most aggregates for concrete in South Africa originate from solid rock that has been broken down through natural weathering or mechanical crushing processes (Grieve, 2009).

Quality control standards require aggregates for concrete to meet a criteria for cleanliness, strength and durability, while properties such as softness, flakiness, excessive porosity or potential reactivity in concrete should be avoided. Hard, igneous rocks are given preference over sedimentary and certain metamorphic rocks. However, any of these three rocks are suitable as aggregates in concrete if they exhibit sufficient physical and chemical stability (Alexander and Mindess, 2005). As mentioned in Chapter 2, Part 2.1, dolomite, andesite, quartzite, ferro-quartzite and felsite have been selected as aggregates for this study. The locations from where the aggregates were excavated and the properties of the aggregates are discussed below. Table 2.2 summarises the typical mineral compositions of each aggregate.

Table 2.2: The typical mineral compositions of the aggregate types.

Aggregate	Mineral composition	Chemical symbol
Dolomite	Calcium magnesium carbonate Occasionally chert and secondary quartz veins (Hein, 2014)	$CaMg(CO_3)_2$ SiO_2
Andesite	Plagioclase Augite Orthopyroxene Hornblende Olivine Ilmenite Titanomagnetite Garnet (Alex Strekeisen, 2020)	$(Na,Ca)(Si,Al)_4O_8$ $(Ca,Na)(Mg,Fe,Al,Ti)(Si,Al)_2O_6$ $(Mg,Fe)_2Si_2O_6$ $(Ca,Na)_2(Mg,Fe,Al)_5(Al,Si)_8O_{22}(OH)_2$ $(Mg,Fe)_2SiO_4$ $(Fe,Ti)_2O_3$ $Fe^{2+}(Fe^{3+},Ti)_2O_4$ $R_3R_2(SiO_4)_3$
Quartzite	Majority quartz Lithic fragments (e.g. shale) Feldspar and matrix: Muscovite Pyrophyllite Chlorite (Law et al., 1990)	SiO_2 $KAl_2(Si_3Al)O_{10}(OH)_2$ $Al_2Si_4O_{10}(OH)_2$ ClO^{2-}
Ferro meta-quartzite	Majority quartz Concentration of iron-oxide minerals: Hematite Magnetite	SiO_2 Fe_2O_3 Fe_3O_4
Felsite	Quartz Alkali feldspar	SiO_2 $(K,Na)AlSi_3O_8$

2.2.4.1. Lyttelton Dolomite Mine

Dolomite, or calcium magnesium carbonate ($CaMg(CO_3)_2$), is a carbonate mineral formed through diagenetic disintegration of magnesium-rich calcites (Holmén, 2000; Haist et al., 2021). The sedimentary rock mined from the Lyttelton Dolomite Mine formed through dolomitization and is a highly beneficial aggregate suitable for concrete production. Beyond demonstrating easier handling and placement of fresh dolomite concrete, this aggregate effectively strengthens the durability of concrete subjected to sulphate and acidic environments. Its acid-neutralizing property is represented by its successful reduction of sewer pipe corrosion, providing an economic benefit (Davis and Alexander, 1992a). Dolomite requires little mixing water in concrete mixtures which increases the compressive strength of the concrete (Gusain et al., 2023). Dolomite has an advantage for high-strength concrete mixture designs because of its high elastic modulus which enhances compressive strength; and a disadvantage from weak planes and fractures which lowers its flexural strength and water durability. Despite this, these qualities create significant economic advantages across different structural applications (Davis and Alexander, 1992a).

2.2.4.2. Eikenhof Andesite Quarry

Andesite is primarily composed of plagioclase feldspar and pyroxene crystals (Hutchison, 2005). The Meta-Mela andesite is extracted from the Eikenhof Quarry. This extrusive volcanic rock is dense and competent, predominantly used as an aggregate in high-quality concrete around the Witwatersrand area. It usually displays high compressive strengths and elastic moduli (96 – 105 GPa), often exceeding that of most other rock types, with the exception of dolomite. Furthermore, the andesite from the Eikenhof Quarry does not pose any harmful threats regarding alkali-reactivity when used in concrete (Davis and Alexander, 1992b), therefore can be used in structures exposed to different environments.

2.2.4.3. Sub-Nigel Quartzite Quarry

The quartzite is a strong, durable metamorphic rock, mainly composed of quartz grains. Quartz generally has a ranking of 7 (Blue Pearl Stone, 2016) on the Mohs hardness scale, making it resistant to weathering and abrasion, which is essential for preserving the integrity of concrete structures under high traffic loads. Poorly sorted quartzites have a low porosity, preventing water from being trapped within the rock, and is resistant to chemical weathering which helps to strengthen concrete overall by avoiding deterioration over time. The quartzite has been

integral to the concrete production history in Johannesburg and nearby regions, often sourced from abundant quartzite deposits in mine waste dumps and quarries, such as the Sub-Nigel Quartzite Quarry. While these aggregates contribute to high-quality concrete, it is important to recognize their limitations. Some quartzites, especially from the West Rand, contain shale, siltstone and lava (Joubert and Johnson, 1998). However, studies show that these materials generally have minimal impact on concrete properties. Pyrite traces may also be present, but their effect on concrete integrity is usually insignificant, except for potential discoloration on exposed aggregate surfaces due to pyrite oxidation. A notable portion of the quartzite is alkali reactive, requiring precautions in critical concrete applications using this aggregate (Davis and Alexander, 1992b).

2.2.4.4. Ferro Meta-quartzite Quarry

Ferro meta-quartzite, sourced mainly from the Pretoria Group quartzites and the Ferro Metaquartzite Quarry, consists of a significant amount of pink and red coloured aggregate that is widely used in concrete manufacture in and around Pretoria. The use of sand derived from this rock tends to produce very visible colour changes in the final concrete product. The ferro quartzite is crushed at the Ferro facility and is known for its toughness, rivalling the durability of quartzite. Concrete produced with this aggregate usually displays comparable compressive strength (31 – 57 MPa at 28 days) to that of the quartzite concrete (31 – 66 MPa at 28 days), with a slightly higher elastic modulus performance (42 – 98 GPa). Additionally, it has the advantage of being non-reactive with alkalis, distinguishing it from quartzite in this aspect (Davis and Alexander, 1992b).

2.2.4.5. Zeekoewater Felsite Quarry

Felsite is an igneous rock that has a high silica concentration and a fine-grained texture. Felsite aggregates are also suitable for high-traffic locations like roadways because they offer good resistance to weathering and abrasion. Felsite sourced from Zeekoewater Quarry shows non-reactivity with alkalis and produces concrete with high strengths and elastic moduli (77 – 89 GPa) (Davis and Alexander, 1992b). However, these felsite aggregates tend to have a flaky and elongated morphology, which can create harshness in fresh concrete. However, this disadvantage can be corrected by using a well-graded natural sand in place of crusher sand, or a combination of these sands. At the Zeekoewater facility, flaky felsite aggregates have reduced as a result of advancements in crushing techniques. Felsite reveals a peculiar behaviour wherein

adhesion does not readily occur in the concrete matrix during early stages, however, later stages do experience improved bond strength (Davis and Alexander, 1992a).

Each of these rocks have certain qualities that make them suitable aggregates in concrete. Concrete properties are governed by the properties of the aggregate. Thus far, the typical qualitative mineral composition of the aggregates have been discussed. The quantitative compositions are determined through petrography and TIMA.

2.2.5. Effects of aggregate properties on concrete performance

Traditional concrete has already been defined as a composite material made from mineral aggregates in a cement-based matrix (Alexander and Mindess, 2005; Wittmann et al., 2010). Concrete can further be described as a three-phase material (Ollivier et al., 1995; Alexander and Mindess, 2005; Sahu et al., 2016; Chen et al., 2024) constituting a primary bulk cement-paste phase, an aggregate phase and an intermediary phase known as the interfacial transition zone (ITZ), which is weaker than the other two phases (Alexander and Mindess, 2005; Chen et al., 2024). Characteristics such as shrinkage or expansion, compressive or tensile strength (Wittmann et al., 2010), and the overall performance of concrete are governed by the microstructure of the concrete (Alexander and Mindess, 2005; Chen et al., 2024). The properties of the microstructure of concrete develops during the hydration process of cement (Wittmann et al., 2010), and it describes the nature of the solid, as well as the pore phases at the micron scale. Within this microstructure, larger-scale components interact between the aggregates and cement (Alexander and Mindess, 2005; Chen et al., 2024), highlighting the importance of aggregate properties in concrete.

The strength, durability and workability of concrete are directly influenced by the physical, mechanical and chemical properties of its aggregates. Understanding these properties is crucial for optimizing concrete formulations to meet specific performance requirements. Testing methods like compressive and bending strength tests, along with Mohr's stress circles (Twagira and Jenkins, 2009), are commonly used to evaluate concrete strength and predict failure mechanisms. Mohr's circles illustrate the relationship between normal and shear stresses on a sample, with Coulomb’s Law of Failure defining the slope and height of the failure envelope (Figure 2.4) (Gibbs, 2023). The critical shear stress ($\sigma(c)$) necessary for faulting is derived in Equation 2.1.

$$\sigma(c) = \sigma(o) + \sigma(N)tan(\phi) \qquad \textit{Equation 2.1}$$

where:

- *σ(c)* = critical shear stress (Pa or N/m^2),
- *σ(o)* = cohesive strength (Pa or N/m^2),
- *σ(N)* = normal stress on the concrete cube (Pa or N/m^2),
- ϕ = internal friction angle (°),
- *tan(ϕ)* = coefficient of internal friction (slope of the failure envelope).

Stresses within the failure envelope are stable, while those beyond it lead to fracture and failure (Gibbs, 2023).

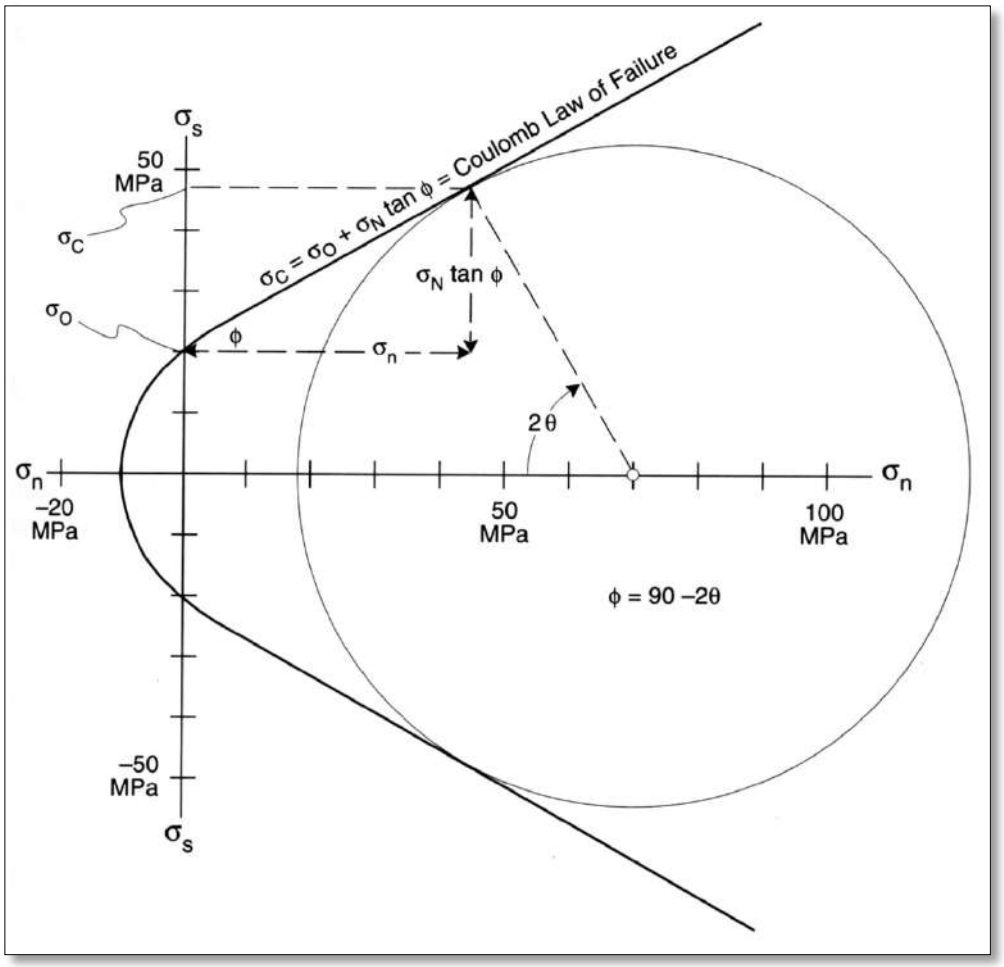


Figure 2.4: Schematic diagram of the failure envelope defined by Coulomb's Law of Failure (Gibbs, 2023).

2.2.5.1. Physical and mechanical properties of aggregates in concrete

Physical and mechanical properties such as density, porosity, morphology, surface texture, grading, permeability, and mechanical robustness are essential indicators of aggregate performance. Testing methods, including Aggregate Crushing Value (ACV), Unconfined Compressive Strength (UCS), Los Angeles Abrasion tests, and the Aggregate Impact Value (AIV) gauge aggregate strength and resilience in concrete. When concrete surfaces are exposed to abrasive forces, characteristics like abrasion resistance, wear resistance, and hardness become significant. Tests such as the Aggregate Abrasion Value (AAV), Los Angeles Abrasion Value, sulphur soundness tests, and wet absorption tests, are essential for assessing these properties. Understanding fracture properties, such as fracture energy and fracture toughness, is important for interpreting aggregate behaviour under stress (Alexander and Mindess, 2005; Chen et al., 2024).

Since this study focuses on the effects of geological characteristics, surface texture and surface energy of crushed rock aggregates on the compressive strength of concrete, the UCS test is applied to evaluate aggregate performance in concrete.

2.2.5.2. Compressive strength of concrete

Compressive strength is a primary measure of concrete strength, widely used in global standards. In South Africa, the SANS standards 5860, 5861-2, 5861-3, and 5863 (Grieve, 2009) are followed for compressive strength evaluation. Concrete composed of cement, water and aggregates are made into 100×100×100 mm cubes that are cured in water tanks for a given number of days, usually between 7 and 56 days. Once cured, the cubes are subjected to external compressive forces (Figure 2.5) to test the compressive strength of the concrete. The stress-strain relationship of concrete forms a nonlinear curve (Figure 2.6), distinct from the linear stress-strain relationships of aggregate and cement paste phases (Ghadafi and Kankam, 2022). This nonlinearity arises because, as stress is applied, microcracks form and propagate at the ITZ between aggregate particles and cement paste (Alexander and Mindess, 2005; Chen et al., 2024).

The ITZ is the area adjacent to the aggregates (Figure 2.5) in fresh concrete that adopts a rising w/c ratio, creating a different microstructure compared to that of the surrounding hydrated cement paste (Ollivier et al., 1995; Alexander and Mindess, 2005; Sahu et al., 2016; Chen et

al., 2024). The ITZ constitutes between 30 and 60% of the hardened paste phase (Alexander and Mindess, 2005; Chen et al., 2024). The formation of the ITZ in the three-phase model, can be explained by the Wall Effect, where micro-bleeding occurs during concrete vibration to release air bubbles before setting (Huang et al., 2023). This allows water to accumulate around the aggregates and the fresh cement paste surrounding the aggregates adopt a higher water gradient (Ollivier et al., 1995; Sahu et al., 2016). Another potential formation mechanism for the ITZ is the One-sided Growth Effect which states that the growth activity of the cement particles take place only from the cement paste side, instead of from all directions. Nevertheless, both formation mechanisms produce the high porosity characteristic of the ITZ relative to the cement paste, which is dependent on the amount of water trapped in the aggregates (Alexander and Mindess, 2005; Chen et al., 2024).

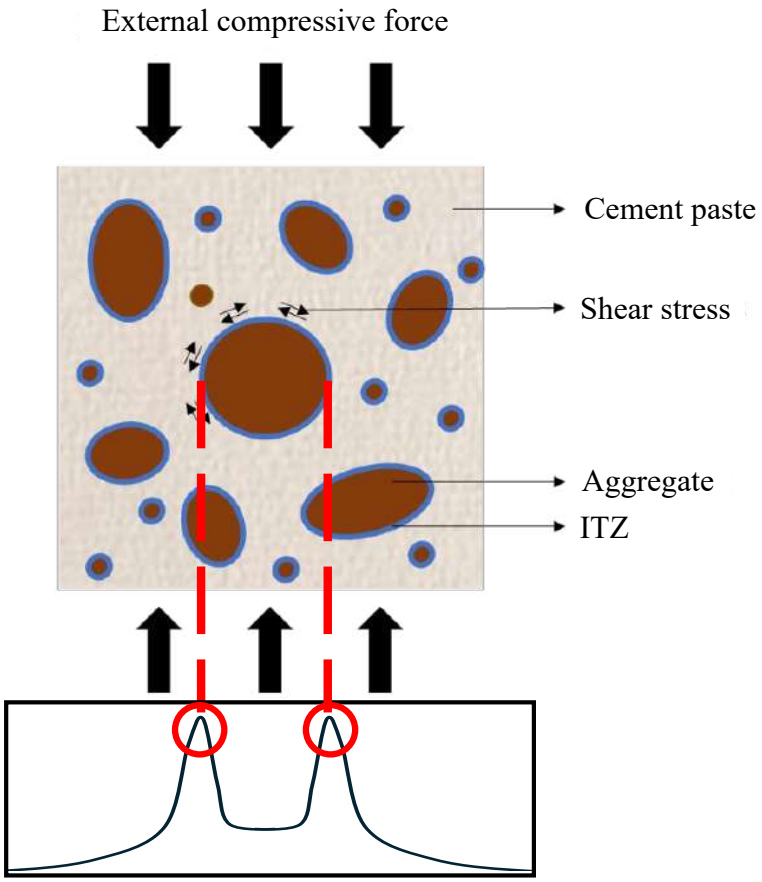


Figure 2.5: Schematic diagram showing how cracking may form under shear stress.

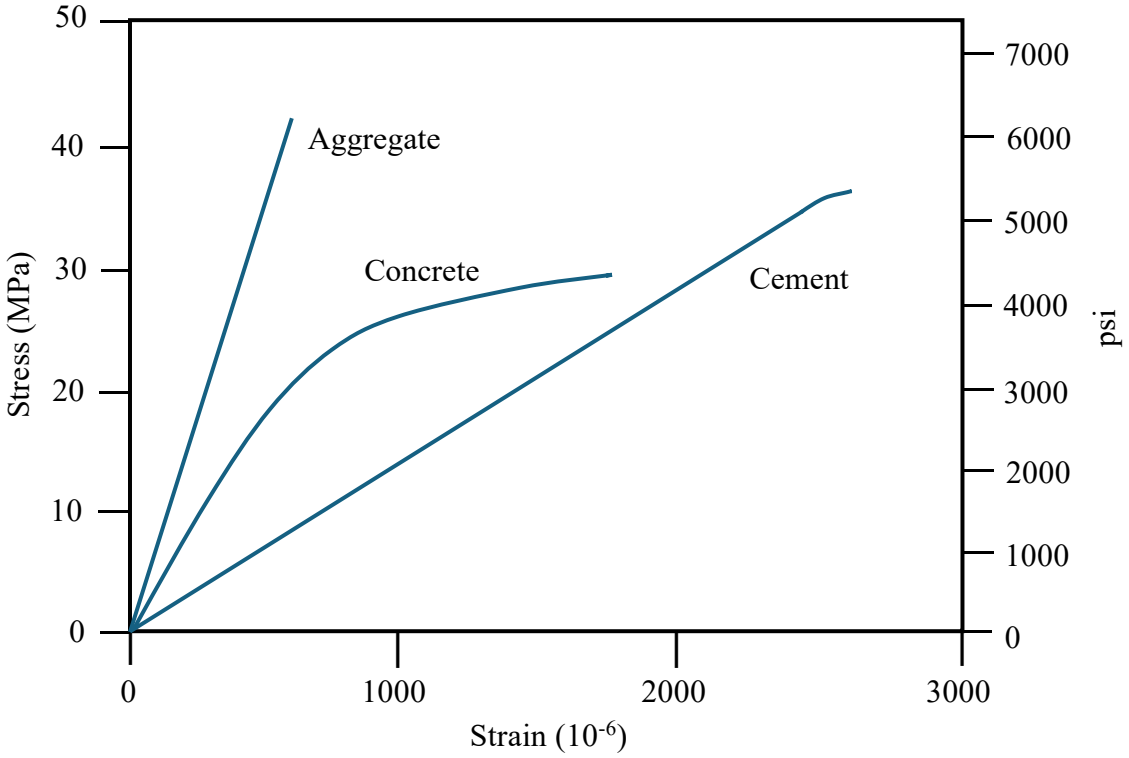


Figure 2.6: Schematic diagram showing the stress-strain relationship for aggregate, concrete and cement paste (modified from Ghadafi and Kankam, 2022).

The presence of a higher w/c ratio at the ITZ suggests a diffusion process during hydration (Ollivier et al., 1995; Sahu et al., 2016), resulting in a roughly 50 μm zone characterized as a heterogeneous region with increased porosity due to larger pores (Alexander and Mindess, 2005; Chen et al., 2024) and a corresponding gradient of anhydrous and hydrated phases (Ollivier et al., 1995; Sahu et al., 2016). As a result of a higher porosity and increased w/c ratio, this zone is weaker than the aggregate and prone to cracking due to shear stresses (Figure 2.5). Therefore, in concrete, when a load is applied to a three-dimensional framework (i.e. concrete cube) of micro-particles, a complex state of shear stress builds up at the ITZ when an external compressive force is exerted onto a concrete cube (Figure 2.5). The rock aggregate is much more stiff and stronger than the cement paste (Figure 2.5) and may retain more stress without faulting. Therefore, a portion of the concrete wants to move under compression (the cement paste), and another portion wants to remain stationary (the aggregate). At the sites circled in red on Figure 2.5, where the stresses are above the local load bearing capacity, damage will occur in the form of micro-crack formation. Under continuous loading, this process leads to progressive damage and to macroscopic cracks (Wittmann et al., 2010), affecting the performance of concrete (Ghadafi and Kankam, 2022).

Circling back to the UCS tests, concrete cubes can fail in different ways depending on the concrete composition and quality, as well as the rate of the applied load and the positioning. However, according to BS 1881-116:1983, there are only three acceptable failure patterns – shown in Figure 2.7, row 1 – in which all four exposed faces crack relatively evenly, with minimal damage to the faces that are in contact with the testing apparatus. Any other failure patterns are deemed unsatisfactory according to BS 1881-116:1983, shown in Figure 2.7, rows 2 – 4 (Premakumara, 2020).

One way of strengthening the ITZ is the utilization of fine and well-dispersed mineral additives which lowers the initial w/c ratio gradient around the aggregates, densifying the ITZ. Particularly in the vicinity of calcareous aggregates, the microstructure of the ITZ may be enhanced through reactions with calcium aluminates in the PC paste, forming calcium carboaluminates (Ollivier et al., 1995; Sahu et al., 2016).

Other properties that have an influence on the ITZ or the bond between the cement and aggregate phases are surface energy and surface texture. Surface energy refers to how an aggregate interacts with different materials, such as liquids, i.e. water in the cement phase; and urface texture refers to the roughness of a fresh aggregate surface which bonds with the cement phase in concrete.

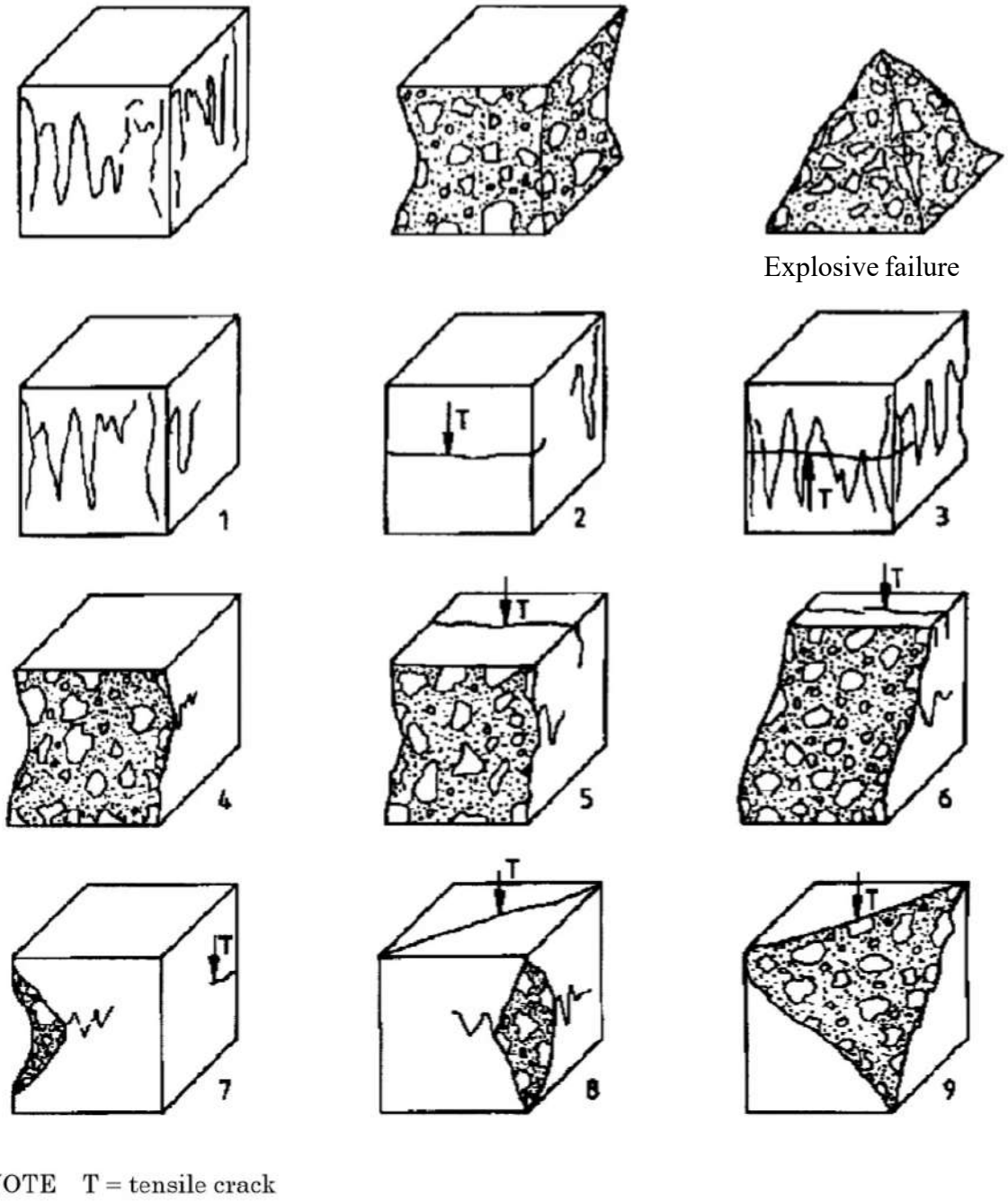


Figure 2.7: Row 1 – satisfactory failure patterns according to BS 1881-116:1983. Failure patterns labelled 1 to 9 – unsatisfactory failure pattern. Note that T represents the tensile crack (Premakumara, 2020).

2.2.5.3. Surface free energy (SFE)

The SFE quantifies the intermolecular forces at the surface of a solid (Bhardwaj and Singh, 2023). Contact angle measurements are increasingly becoming the starting point for analysing the interaction energy between different geological materials and different liquids (Koc and Bulut, 2012). Moisture damage, characterized by the work of adhesion or weakening of the bonding strength between aggregates and cement can be analysed using the Sessile Drop (SD) method. This method measures dynamic (instantaneous) and static contact angles (Wei and Zhang, 2012) directly on aggregate samples. The SD method is simple, accurate and reliable, making it suitable for measuring contact angles and calculating SFE components.

The atoms and molecules at the surfaces of the aggregates are in distinct states of chemical equilibrium compared to those within the aggregate. These surface atoms and molecules were previously thought to only involve Van der Waals forces that are responsible for interfacial interactions between aggregates and cement. However, the Good-van Oss-Chaudhury, or acid-base theory, clarified that surface forces include both Van der Waals (apolar) forces and Lewis acid-base (polar) interactions (Koc and Bulut, 2012).

SFE components of solid materials, like aggregates, are usually determined indirectly using contact angle measurements from the SD method, which involves depositing small droplets of appropriate probe liquids on the solid surface. Probe liquids are selected liquids of known SFE used for the SD method. The equilibrium forces between a known liquid droplet and a solid material (Figure 2.8) was first described by Young in 1805. Young's theory, however, is not sufficient on its own as it requires solving two equations with three unknowns. Therefore, the Dupré equation (Equation 2.3), which represents the SFE of the interaction between a solid and a liquid, can be used alongside Young's equation (Equation 2.2) to determine the SFE (Koc and Bulut, 2012).

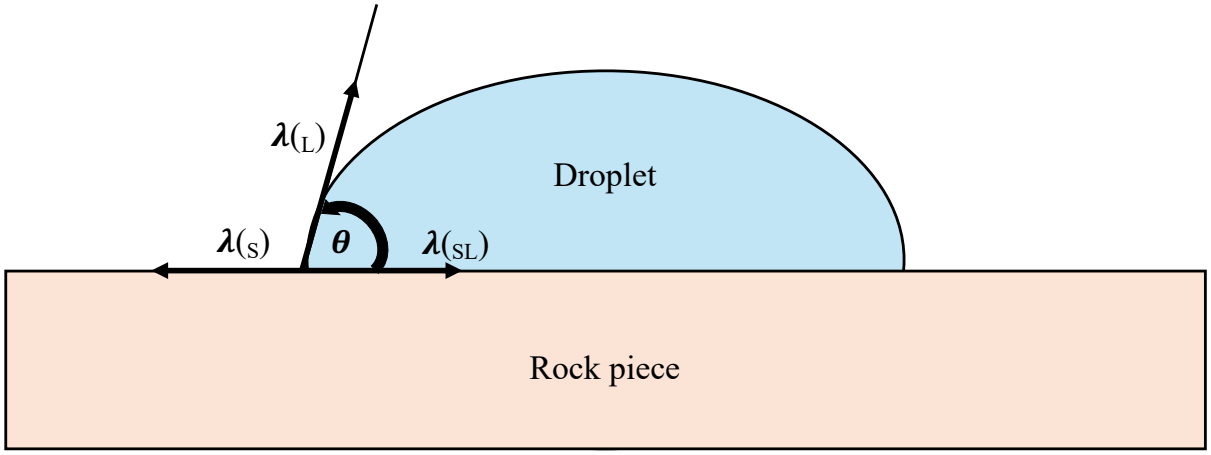


Figure 2.8: Schematic diagram showing the equilibrium forces described by Young in 1805 between a liquid droplet and a solid surface, in this case, a piece of rock aggregate (modified from Koc and Bulut, 2012).

The Young's equation (Equation 2.2) encompasses the surface free energies of the solid rock aggregate (γ^S) and the liquid (γ^L), the interface free energy (γ^{SL}), and the contact angle (θ).

$$\gamma^S = \gamma^L cos\theta + \gamma^{SL} \qquad \textit{Equation 2.2}$$

The Dupré equation (Equation 2.3) that encompasses the work of adhesion (W^{SL}), or the energy required to separate the solid from the liquid at the interface, is as follows.

$$\gamma^S + \gamma^L = W^{SL} + \gamma^{SL} \qquad \textit{Equation 2.3}$$

Using Equation 2.2, Equation 2.3 can further be simplified into Equation 2.4 which directly links the contact angle of the liquid on the aggregate surface to the work of adhesion.

$$W^{SL} = \gamma^L(1 + cos\theta) \qquad \textit{Equation 2.4}$$

The acid-base theory extends Equation 2.4 by considering the acid (γ^+) and base (γ^-) components of the surface energies and is commonly used for SFE characterization of materials (Koc and Bulut, 2012). According to this theory, the total surface energy (γ) of the solid aggregate and liquid considers both Lifshitz-van der Waals (γ^{LW}) and acid-base components

(γ^{AB}) (Equation 2.5), while the acid-base component is further divided into the Lewis acid (γ^{+}) and Lewis base (γ^{-}) (Equation 2.6).

$$\gamma = \gamma^{LW} + \gamma^{AB} \qquad \textit{Equation 2.5}$$

and

$$\gamma^{AB} = 2\sqrt{\gamma^{+}\gamma^{-}} \qquad \textit{Equation 2.6}$$

The work of adhesion considering the acid-base theory reflects the Lifshitz-van der Waals components, resulting the Equation 2.7.

$$W^{SL} = \gamma^{LLW} + \gamma^{SLW} + 2(\sqrt{\gamma^{S+}\gamma^{L-}} + \sqrt{\gamma^{S-}\gamma^{L+}}) \qquad \textit{Equation 2.7}$$

The total interaction energy comprising the Lifshitz-van der Waals and Lewis acid-base interactions, leads to the widely-used Young-Dupré equation (Equation 2.8) incorporating the acid-base theory (Koc and Bulut, 2012) and the work of adhesion in Equation 2.4.

$$\gamma^{L}(1 + cos\theta) = 2(\sqrt{\gamma^{SLW}\gamma^{LLW}} + \sqrt{\gamma^{S+}\gamma^{L-}} + \sqrt{\gamma^{S-}\gamma^{L+}}) \qquad \textit{Equation 2.8}$$

where:

- θ = contact angle (°),
- γ^{L} = total surface energy of the liquid (N/m),
- γ^{SLW} = Lifshitz-van der Waals component of the solid aggregate (N/m),
- γ^{LLW} = Lifshitz-van der Waals component of the liquid (N/m),
- γ^{S+} = Lewis acid component of the solid aggregate (N/m),
- γ^{L-} = Lewis base component of the liquid (N/m),
- γ^{S-} = Lewis base component of the solid aggregate (N/m),
- γ^{L+} = Lewis acid component of the liquid (N/m).

The three unknown γ-components for an aggregate (γ^{SLW}, γ^{S+}, γ^{S-}) is determined simultaneously using the measured contact angles from three different probe liquids, two polar

and one apolar. In this study, water and ethylene glycol were chosen as polar liquids, while diiodomethane (DIM) was used as the apolar liquid (W-E-D) (Koc and Bulut, 2012).

To select the probe liquids, a condition number (CN), a numerical measure of sensitivity in the system of equations, and an R^2 value, should be considered. A CN less than 10 is recommended, along with a high R^2 value that is close to 1. A high CN indicates that the system is poorly conditioned and that even small errors in the contact angle measurements could cause significant inaccuracies in the calculated surface energy (Mishra et al., 2020). To attain a low CN, the selected probe liquids should have distinctly different polar and apolar components, ensuring that the equations used to calculate the SFE are independent from one another. The R^2 value is the proportion of variance in the dependent variable (contact angle) explained by the independent variable (surface tension of the probe liquids). A higher R^2 value shows that the selected set of probe liquids closely fit the experimental data and that the set conclusively describes the relationship between the contact angles and the SFE components. The selected combination of probe liquids used in this study provides a CN of 4.47 and an average R^2 of 0.48 (Mishra et al., 2020; Bhardwaj and Singh, 2023). Table 2.3 shows the components for each probe liquids.

Table 2.3: The components for each liquid where γ^{LLW} is the Lifshitz-van der Waals component, γ^{LAB} is the total Lewis acid-base, γ^{L+} is the Lewis acid component, γ^{L-} is the Lewis base component, and γ^{T} is the total of these energies.

Probe liquid	γ^{LLW}	γ^{LAB}	γ^{L+}	γ^{L-}	γ^{T}
Water	21.8	51.0	25.5	25.5	72.8
Ethylene Glycol	29.0	18.9	1.9	47.0	47.9
Diiodomethane	50.8	0.0	0.0	0.0	50.8

The SD method measures contact angles directly and the Contact Angle Meter DMs-401 automatically generates the SFE. However, Appendix B contains the manual calculations using Equations 2.5, 2.6 and 2.8 to determine the SFE of an aggregate sample. To ensure representative contact angles, aggregate surfaces must be flat, smooth, and clean.

The contact angles measured from the liquid droplets on the solid surface provide important insights into the surface properties of the different aggregates. It differentiates between hydrophilic and hydrophobic surfaces or the wettability of the aggregate surface. Hydrophilic surfaces are characterized by smaller contact angles, higher interfacial tension, higher SFE and better wettability. Good wettability means that water spreads more easily across these surfaces which displays good adhesiveness or bonding between aggregates and cement. Hydrophobic surfaces are characterized by larger contact angles, lower interfacial tension, lower SFE and poor wettability. It is unknown whether these surface interactions are best quantified by measuring the dynamic contact angle at 1 second, or the static contact angle that is reached when the droplet seizes to expand on the solid aggregate surface, allowing the droplet to exist in its most stable state. This static angle is measured after 22 to 30 seconds. Another factor affecting the accuracy of contact angle measurements is the size of the liquid droplet. Hydrophobic surfaces require larger droplets (up to 10 µL) (Ramé-hart instrument co., 2024), while smaller droplets (2 to 3 µL) are better suited for hydrophilic surfaces to prevent absorption on the aggregate surface.

2.2.5.4. Surface texture

The two components present in SFE are Lewis acid-base interactions and Lifshitz-van der Waals interactions. These components are used to estimate the work of cohesion within the same material and the work of adhesion needed to separate the physical bond between two surfaces, such as aggregate and cement. In addition to these intermolecular interactions, bonding is also dependent on the mechanical and chemical bond. Mechanical bonding is defined by the interlocking that occurs when rough-textured surfaces bond with cement. Chemical bonding relies on the interactions between PC minerals with various aggregate minerals which occur when smooth-textured surfaces bond with cement (Bhardwaj and Singh, 2023).

The surface texture is dependent on the surface area of the individual crystals that make up the aggregate. Fine-grained aggregates expose a larger total surface area when broken due to the formation of small, irregular, jagged fragments and create a microscopically rougher surface texture. The coarse-grained aggregates tend to break along natural crystal boundaries creating planar surfaces and smoother surface textures on individual crystal grains. An exception to this is the porosity factor that states that coarse-grained aggregates may have a rougher texture

when a high porosity creates open spaces for cement paste to run through, allowing bonding to take place.

For modern-day advanced concretes that are made specially for certain structures, enhancing the density of the ITZ is the key component to increasing the compressive strength. The texture of aggregate surfaces play a crucial role in determining this component (Grieve, 2009). Aggregate surface texture has an effect on the properties of concrete, influencing the plastic properties of the mixture, mainly due to the surface area effect and interparticle friction effect. Rough aggregate surfaces have a greater surface area, equating a higher interparticle friction which demands a greater external force to move aggregate particles over one another within a concrete mixture. Therefore, rough-textured aggregates require more water in a concrete mixture (Alexander and Mindess, 2005; Chen et al., 2024) which increases the workability of the concrete.

The bond between two materials is influenced by mechanical interlocking, where rough-textured surfaces bond more effectively with cement, defining the mechanical and chemical bond, better known as the macro-mechanical bond. This is compared to smooth-textured surfaces which reduce the mechanical bond and favour the chemical bond, better known as the micro-mechanical bond. The chemical bond between aggregates and cement can be measured when the smooth surface is polished to a high fineness and mechanical bond is eliminated.

Bending tests are commonly used to measure the bond strength at the interface of two materials, accounting for physical, chemical, and mechanical interactions (Bhardwaj and Singh, 2023). One way of measuring these strengths is through the 3-point bending test. This involves exerting a load on a sample, which in this study would be a prism made from aggregate and cement, that is supported at two points at the base (Figure 2.9) (Gu et al., 2016). The point of loading would be exerted directly on the interface of these two phases, i.e. the ITZ. According to bending theory, the test measures the load (kg) required to reach failure that is directly proportional to the bending forces that act on the prism sample. From previous studies, the bending strengths for different aggregates in concrete vary between 1 and 7 MPa (Neville, 2011).

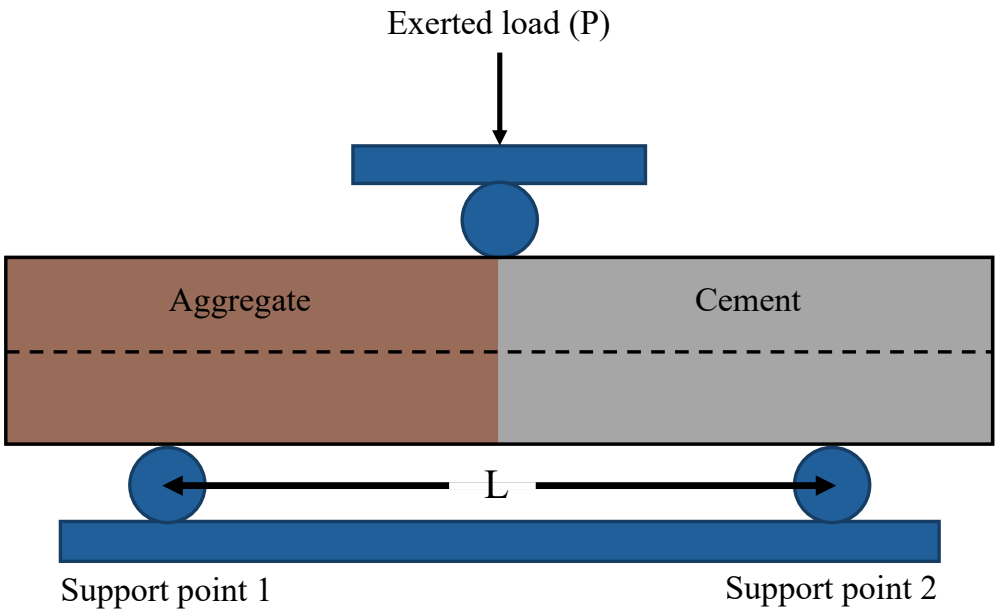


Figure 2.9: Schematic diagram of the 3-point bending test showing the aggregate-cement prism with the load exerted vertically at the interface and the two support points of the system (modified from Gu et al., 2016, p.2).

When a prism is deformed by bending, the atoms and molecules making up the material (aggregate-cement prism) starts to move apart through tension or move closer together through compression (Figure 2.10A). The chemical bonds which form through molecular reactions between the aggregates and cement are strong, holding the prism together (Gordon, 1978; Ferreira et al., 2022). Therefore, when the prism is undergoing tension at the base and compression at the top, these strong chemical bonds that resist deformation are stretched and compressed until failure occurs. Failure is caused by these longitudinal stresses (tension and compression) that act equally but opposite (Gu et al., 2016) on the surface of the prism.

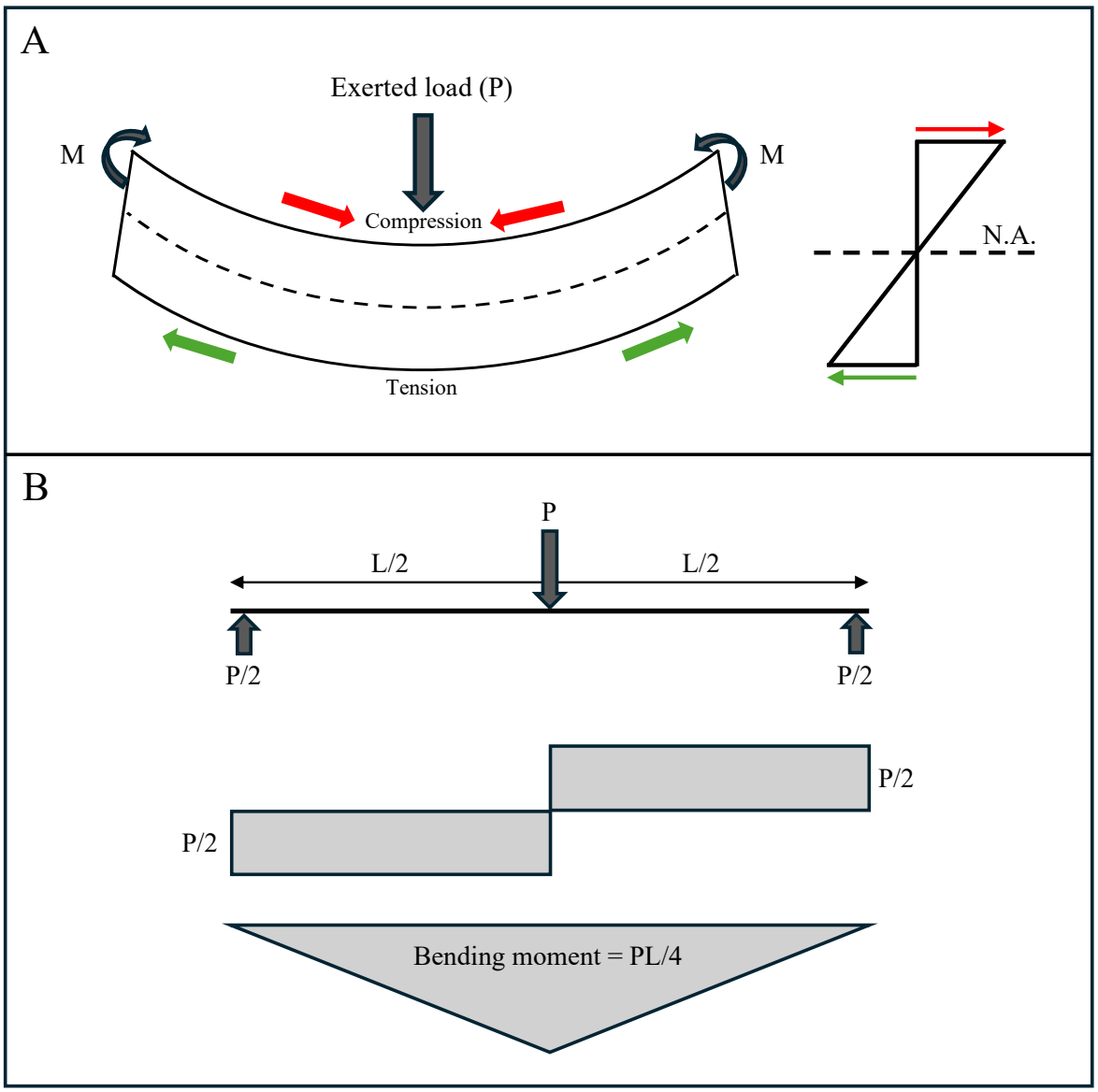


Figure 2.10: Schematic diagram of the bending theory. A – the longitudinal tension and compression forces acting on the surface of the prism that are equal in size but opposite in direction, reversing at the neutral axis (N.A.). B – the bending moment diagram for a 3-point bending test (modified from Gu et al., 2016, p. 2).

The prism deforms under an applied load, distorting it into a bent or curved shape. Atoms and molecules on the compression side of the bending prism will experience shortening, whereas on the tension side, the prism will experience lengthening (Gordon, 1978; Ferreira et al., 2022). If the material of the prism follows Hooke's law (Gordon, 1978; Owens, 2009) which states that the strain of the material (aggregate-cement prism) and the applied stress is directly proportional within the elastic limit (Kumar, 2020), then the stress and strain across any part of the prism will be a straight line. The neutral axis (N.A.) (Figure 2.10) which lies at the

gravitational center of a rectangular prism experiences neither stress nor strain in the form of tension or compression, rather, it is zero at this point (Gordon, 1978; Ferreira et al., 2022).

The tensional and compressional stresses (σ) increase proportionally with the distance away from the neutral axis (y). Therefore, material that lies near the N.A. carry little to no stress. The longitudinal stress (σ) due to bending is determined using Equation 2.9.

$$\sigma = \frac{My}{I} \qquad \textit{Equation 2.9}$$

where:

- σ = longitudinal stress (MPa),
- M = bending moment (N.mm),
- I = second moment of area of the cross-section of the prism (mm^4),
- y = distance from the N.A. to the surface (mm).

The components that make up Equation 2.9 can further be explored. The bending moment (M) is the rotational force measured when an applied force (P) is exerted on the prism perpendicularly to the length between the two support points of the base plate (L) (Figure 2.10) (Liang, 2024). Bending moment is determined using the following Equation 2.10.

$$M = \frac{PL}{4} \qquad \textit{Equation 2.10}$$

where:

- P = applied force (N),
- L = length between the support points of the base plates (mm).

The applied force (P) is calculated using Equation 2.11.

$$P = m \times g \qquad \textit{Equation 2.11}$$

where:

- P = applied force (N),

- m = load at failure (kg),
- g = force of gravity = 9.81m/s^2.

The second moment of area (I) reflects how the area of the cross section of a rectangular prism (Figure 2.10) is distributed relative to the neutral axis and is determined by the following Equation 2.12.

$$I = \frac{bd^3}{12} \qquad \textit{Equation 2.12}$$

where:

- b = width of the prism (mm),
- d = height of the prism (mm) (Figure 2.8).

The distance from the N.A. to the surface of the prism (y) is defined by Equation 2.13.

$$y = \frac{d}{2} \qquad \textit{Equation 2.13}$$

These equations can be simplified into Equation 2.14 to calculate the bending strength of the prisms. This equation is typically used when the load is applied directly in the centre of the prism, i.e. when the cement and aggregate making up the prism are equal in length.

$$\sigma = \frac{3PL}{2bd^2} \qquad \textit{Equation 2.14}$$

Surface texture involves both mechanical and chemical properties of aggregates. The chemical properties play a crucial role when smooth aggregate surfaces are moulded against cement paste to form prisms and influence the bond between the two phases.

2.2.5.5. Chemical properties of aggregates in concrete

The chemical composition and properties of aggregates are crucial in ensuring the prolonged strength and effectiveness of concrete structures. These properties include chemical compatibility, resistance against external corrosive agents, and the influence of aggregates on

cement hydration reactions. The general mineralogy of aggregates, the occurrence of specific minerals and alkali-silica reactions (ASR) can significantly affect the durability and strength of concrete. Moreover, other characteristics that affect these concrete properties include resistance to freeze-thaw cycles, soundness and detrimental minerals. Understanding these properties is important for aggregate selection that enhance the longevity and functionality of concrete structures (Alexander and Mindess, 2005; Chen et al., 2024).

Changes in concrete structures can become permanent from environmental and operational stresses and some of these changes originate from complex chemical processes (Gu et al., 2016). Detrimental minerals and salts in aggregates threaten construction projects (Alexander and Mindess, 2005; Chen et al., 2024) by causing structural degradation (Gu et al., 2016). Such minerals include chlorides, iron oxides (Aligizaki et al., 2000; Huang et al., 2023), sulphates and micas, all of which have an impact on the strength of concrete. Chlorides and iron oxides increase the risk of corrosion in concrete that have reinforcing steel, especially when fine aggregates are used due to the increase in surface area. Sulphates influence the hydration of cement which affects the compressive strength (Alexander and Mindess, 2005; Chen et al., 2024). The amount of calcium sulphate in PC has an impact on different aspects of concrete, such as the hydration, rheology, setting time, phase composition, distribution of porosity, and the strength of cement-based materials (Neto et al., 2021). Micas, such as biotite and muscovite, have a flaky texture due to its cleavage and soft nature, which influences the strength and workability of concrete (Alexander and Mindess, 2005). Moreover, the occurrence of weathering minerals (Earle, 2015), organic waste in surface deposits, and base material contamination or harmful substances during stockpiling or transportation can weaken the quality of aggregates (Alexander and Mindess, 2005; Chen et al., 2024). The interior deterioration of concrete structures primarily stems from interior weaknesses due to flawed mixture design, inadequate aggregates, deficient construction practices, and bad usage and upkeep of concrete structures. Consequently, continuous dysfunctionality of concrete before and after hardening ultimately poses a safety hazard (Gu et al., 2016). Therefore, certain minerals, rocks, organic matter, and soluble salts are deemed undesirable, further underscoring the importance of aggregate quality control, aggregate selection and handling processes (Alexander and Mindess, 2005; Chen et al., 2024). Figure 2.11 summarises some of the main causes of the deterioration in concrete.

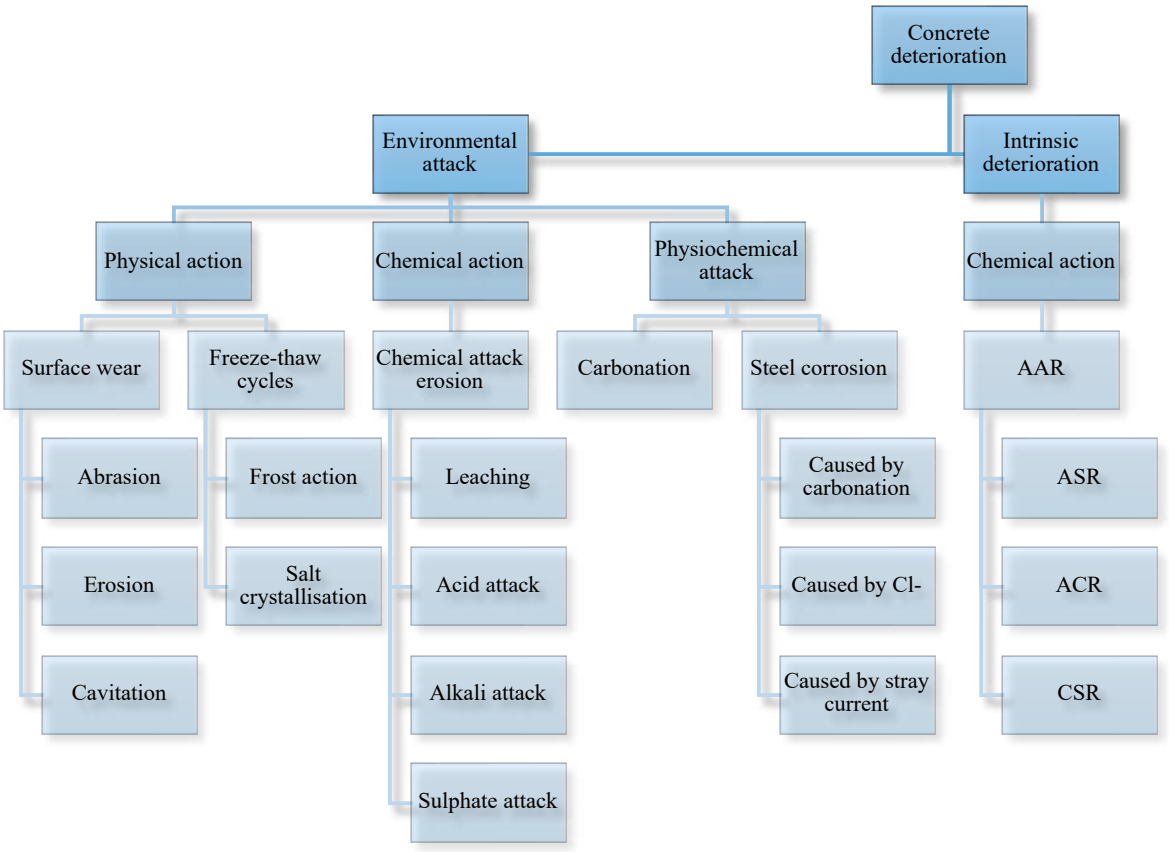


*Figure 2.11: Schematic diagram of the various forms of deterioration that may occur in concrete structures (modified from Gu et al., 2016). *AAR: Alkali-aggregate reaction; ASR: Alkali-silicate reaction; ACR: Alkali-carbonate reaction; CSR: Carbon-silicate reaction.*

2.2.6. Concrete mixture designs

Now that the fundamentals of concrete properties have been laid out, the process of making concrete can be explained following four preparatory methods:

- Grading analysis (coarse and fine aggregate)
- Tests for compacted bulk density (CBD)
- Relative density (RD) measurement
- Trial mixtures

2.2.6.1. Grading and fineness modulus

Grading refers to the sizes of aggregate particles and distribution of materials across various sizes (Addis, 1998). To assess the grade of aggregate, the samples run through a series of

standard sieves (Figure 2.12) to ascertain the proportion of the aggregate that passes through sieves with different sized holes. There are two types of aggregates used in concrete: coarse aggregates which are stone, and fine aggregates which are sand. The sieve size 4.75 mm separates coarse stone from fine sand aggregates (Grieve, 2009). The grading of stone aggregate shows the nominal aggregate size, which assists in determining a K-value used to adjust the mixture design.

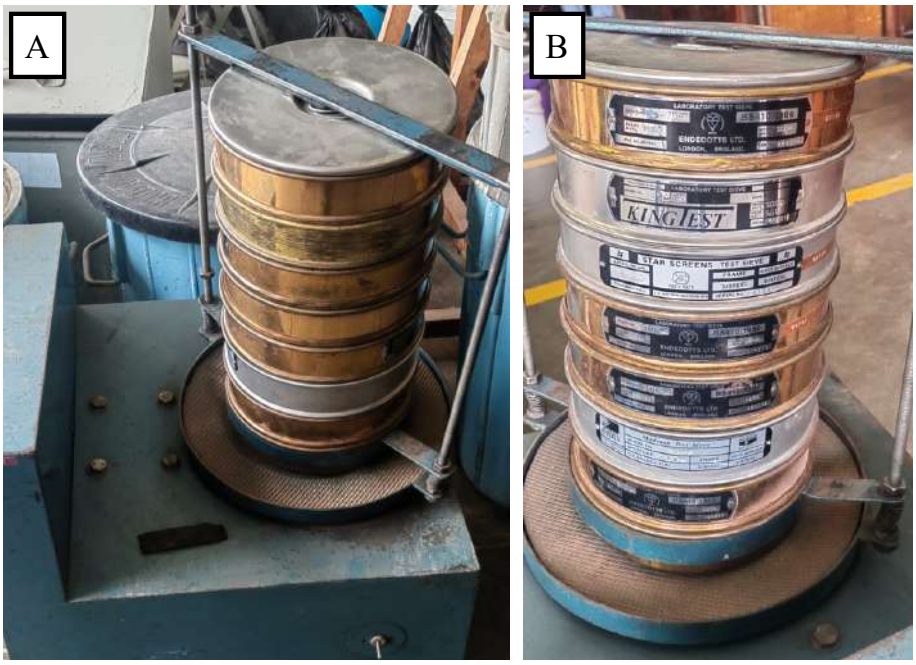


Figure 2.12: A – shaking apparatus to carry out a grading analysis. B – the sieves are mounted from largest at the top to the smallest at the bottom.

The fineness modulus (*FM*) estimates the roughness or fineness of sand (Addis, 1998). It is calculated using the following Equation 2.15.

$$FM = \frac{\Sigma(cumulative\ \%\ retained\ on\ the\ sieves)}{100} \qquad \textit{Equation 2.15}$$

where:

- *FM* = fining modulus
- *Σ (cumulative % retained on the sieves)* = the sum of the cumulative percentage of material left on the sieves with holes less than 4.75 mm and greater than 0.15 mm.

Therefore, the *FM* is determined through the grading of sand. The *FM* is not a direct measurement in millimetres, but rather a position on a scale where the numbers correspond to sieve sizes (Addis, 1998).

2.2.6.2. Compacted bulk density (CBD)

The *CBD* of aggregate is the ratio of its mass (g) to its volume (cm^3) (Akbaş, 2012). This density is determined manually. The only apparatus needed is a scale, a container of known mass and volume, and a long metal rod for stamping.

2.2.6.3. Relative density (RD) measurement

The quantity of mass contained in a specific volume is referred to as density. These densities are usually measured using a digital density meter that relies on the Mechanical Oscillation Principle (Rudolph Research Analytical, 2025) which refers to the repetitive movements of a system around an equilibrium point (Vaia, 2019), and the Gravimetric Method (Rudolph Research Analytical, 2025) which is a quantitative technique that measures a change in mass (Harvey, 2000; Science Ready, 2019).

2.2.6.4. Trial mixture and slump test

The w/c ratio (in this study: 0.4 and 0.6), K-value, FM, CBD and RD of the aggregates are used to design different mixtures called trial mixture designs. The water content is first selected for a 1 m^3 cube. The cement content is determined using the w/c ratio and the stone content (*St*) is determined using the following Equation 2.16.

$$St = CBD(K - 0.1FM) \qquad \textit{Equation 2.16}$$

where:

- *St* = stone content (kg/m^3),
- *CBD* = compacted bulk density (kg/m^3),
- *K* = K-value,
- *FM* = fining modulus.

The mass and density of water, cement and stone are used to determine their volumes using Equation 2.17.

$$V = \frac{m}{\rho}$$ *Equation 2.17*

where:

- V = volume (m^3),
- m = mass of the stones (kg),
- ρ = density (kg/m^3),

Finally, the sand content (S) is determined using the following Equation 2.18.

$$S = 1 - (Vwater + Vcement + Vstone)$$ *Equation 2.18*

where:

S = sand content (m^3),

V_{water} = volume of water (m^3),

V_{cement} = volume of cement (m^3),

V_{stone} = volume of stone (m^3).

After a suitable mixture design is determined, a trial mixture and slump test are conducted. A trial mixture involves weighing and batching the concrete components (cement, water, coarse aggregate and fine aggregate) and mixing fresh concrete. The slump test is used to assess the workability of fresh concrete and determine whether a mixture requires more or less water. The standard slump for concrete is ~75 mm. If the measure exceeds 75 mm, the mixture has too much water; if it is less than 75 mm, there is insufficient water (Concrete Exchange, 2023). However, some concrete mixtures are designed to achieve a certain slump depending on its application.

Chapter 3: Materials and methods

Chapter 3 discusses the preparation of the samples that were used for the methods of this research project, as well as the methods themselves (Figure 3.1).

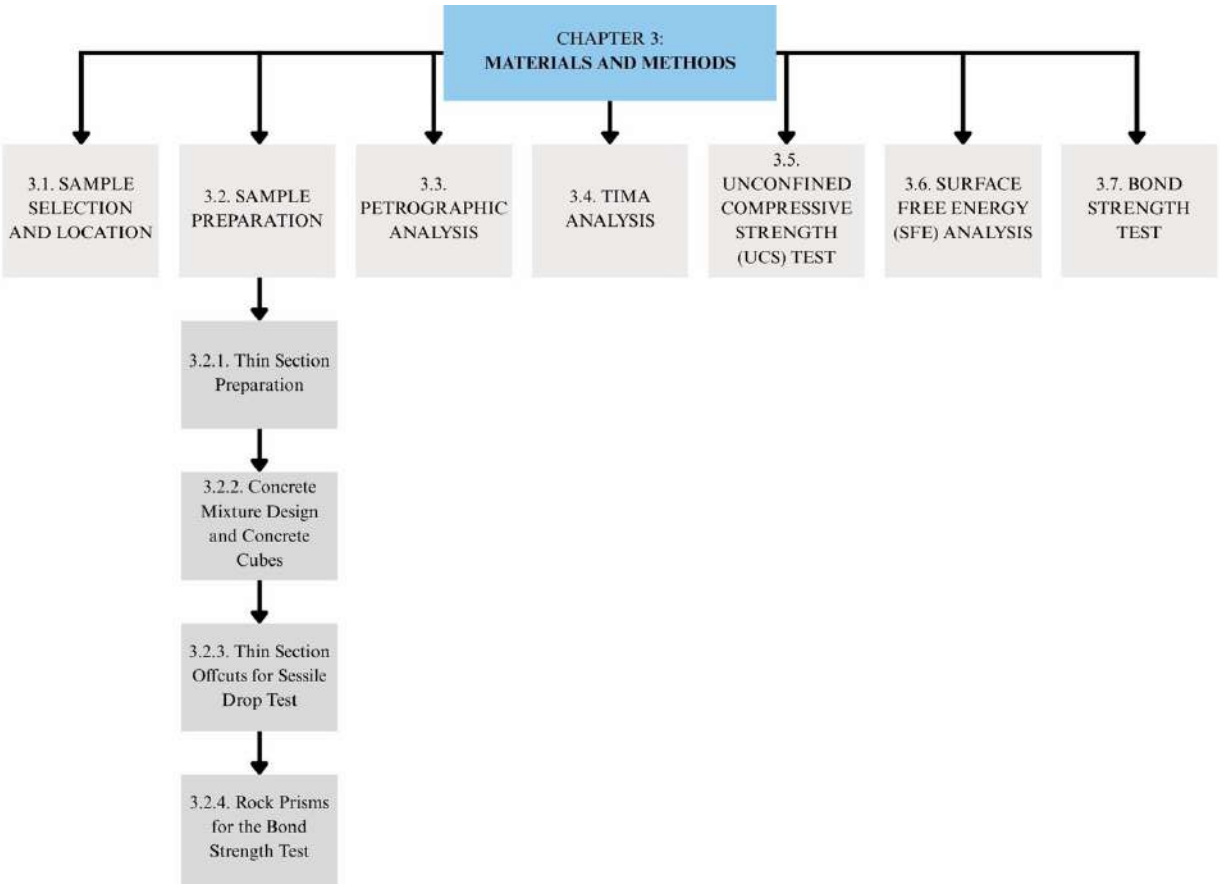


Figure 3.1: A flow diagram showing the structure of Chapter 3.

3.1. Sample selection and location

Five aggregates were collected from five quarries (Table 3.1) across Gauteng and Mpumalanga, South Africa (Figure 3.2). Each rock type was supplied in the aggregate size 14 ± 2 mm, as well as sand and large dump rocks of various sizes.

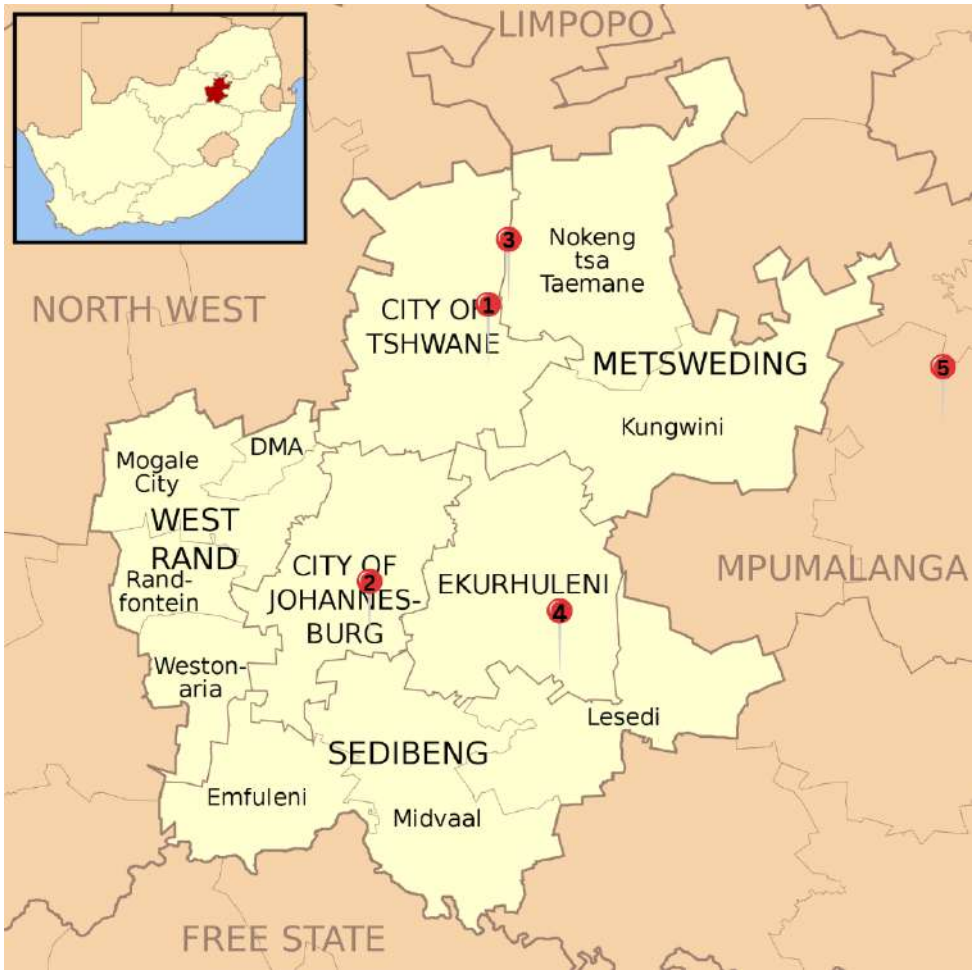


Figure 3.2: Map of Gauteng and surrounding provinces showing the sample locations, 1 – dolomite, 2 – andesite, 3 – quartzite, 4 – ferro quartzite and 5 – felsite (modified from Htonl, 2008).

Table 3.1: The locations and coordinates for the samples 1 to 5.

Aggregate type	Location	Coordinates
1. Dolomite	Lyttelton Dolomite Mine	(-25.84, +28.21)
2. Andesite	Eikenhof Andesite Quarry	(-26.30, +27.99)
3. Ferro meta-quartzite	Ferro Meta-quartzite Quarry	(-25.69, +28.28)
4. Quartzite	Sub-Nigel Quartzite Quarry	(-26.37, +28.44)
5. Felsite	Zeekoewater Quarry	(-25.88, +29.24)

3.2. Sample preparation

From the 14 ± 2 mm aggregates, sand and dump rocks, samples were prepared for each of the following methods: Petrography, TIMA, UCS test, SFE test and Bond Strength test (sections 3.3 – 3.7 of this chapter), that will be discussed in more detail.

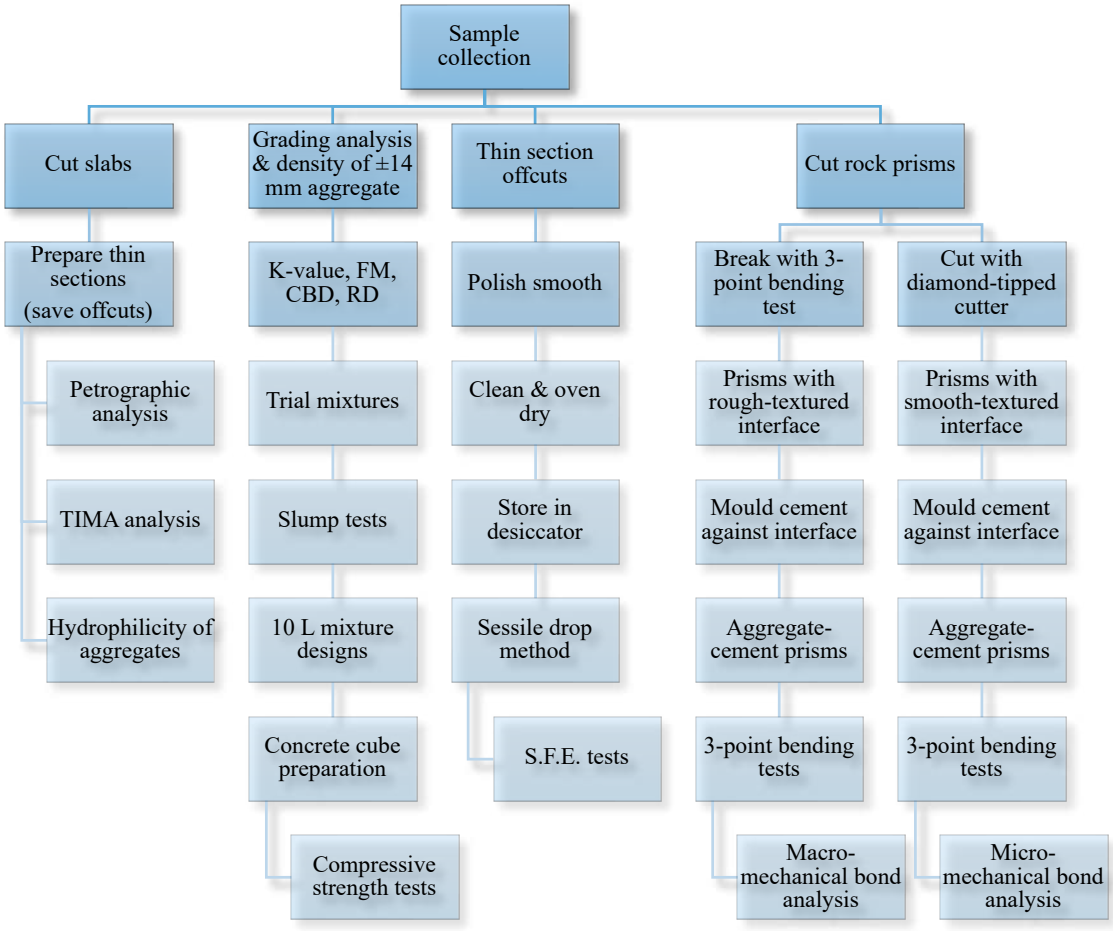


Figure 3.3: Summary of the sample preparation.

3.2.1. Thin section preparation

Five rock samples were mounted and cut with a water-cooled saw to produce 30-micron rock slices. These sliced samples were placed between two glass slides and held together with epoxy to create polished thin sections (40 mm × 25 mm) at the Wits Earth Lab, University of the Witwatersrand. Figure 3.4 shows the rock sample, the cut sample and the thin section. The thin sections were used to carry out the petrographic and TIMA analysis. The mineral assemblages identified were used to analyse how detrimental minerals influence the compressive strength

of concrete, and determine the hydrophilicity of the samples to select an appropriate droplet size for the SD method.



Figure 3.4: From left to right is the rock sample, the cut sample and the thin section of felsite.

3.2.2. Concrete mixture design and concrete cubes

Four preparatory methods were employed to create the concrete mixture designs and ready the concrete cubes for UCS testing. These methods included grading analysis, *RD* measurement, tests for *CBD* and trial mixtures and slump tests.

3.2.2.1. Grading and fineness modulus

The following sieve sizes (mm) were utilised to perform the grading analysis for coarse and fine aggregates:

- 6.7, 9.5, 13.2, 16, 19 and 26.5 for coarse aggregate (Addis, 1998),
- 0.075, 0.15, 0.30, 0.60, 1.18, 2.36 and 4.75 for fine aggregate (Addis, 1998).

The graphs below show the grade for coarse stone (Figure 3.5) and fine sand (Figure 3.6) for each aggregate. The graphs were used to determine the K-value and the *FM* of each aggregate. Figure 3.5 shows that the nominal size for each coarse aggregate is 13.2 mm. According to

Addis (1998), this indicates that the K-value is 0.9. The *FM* for each aggregate was calculated and the values are shown in Table 3.2.

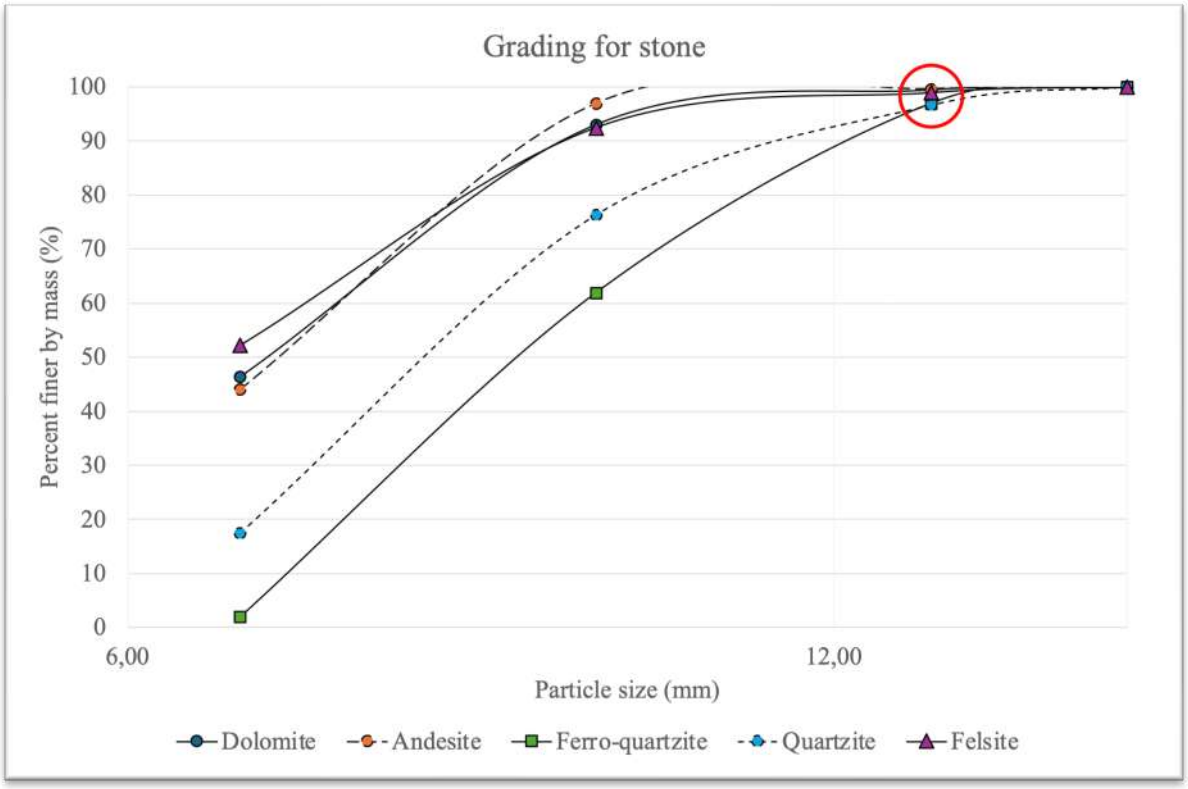


Figure 3.5: Grading analysis for each stone (14 ± 2 mm) aggregate. The nominal aggregate size at 13.2 mm is circled on the graph. This indicates that the K-value is 0.9.

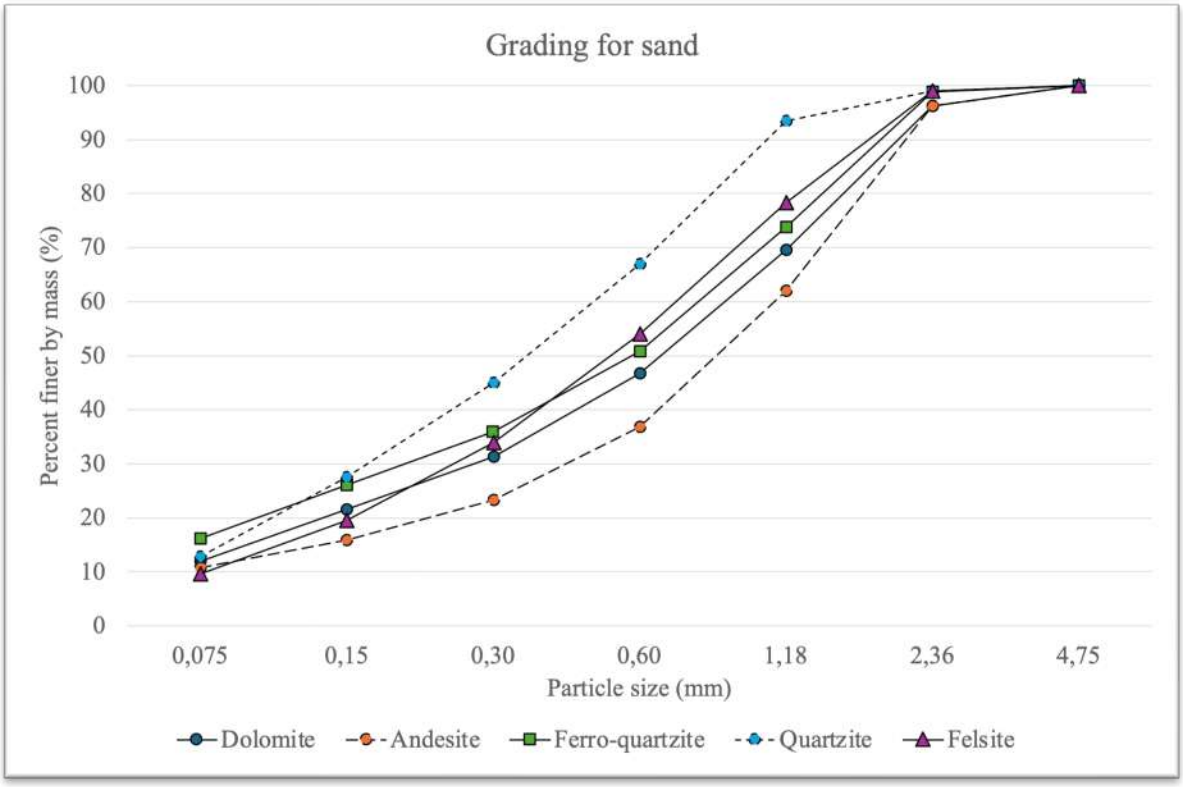


Figure 3.6: Grading analysis for each sand aggregate used to determine the fineness modulus.

3.2.2.2. Relative density (RD) measurement

The Anton Paar Ultrapyc 3000 (Figure 3.7) was used to determine the *RD* of dolomite, andesite, quartzite, ferro-quartzite and felsite. This instrument is ideal for determining actual, absolute, and skeletal volume and density since it uses helium gas pycnometry, a non-destructive method that depends on gas displacement to measure volume (Anton Paar GmbH, 2025). The instrument cup holder with known volume was weighed, tarred, and filled with 14 ± 2 mm stones (dolomite, andesite, quartzite, ferro-quartzite and felsite) before being weighed once more. The filled holder was then placed into a chamber within the pycnometer, which was sealed and pressurized while helium gas filled the voids inside and between the stones. A first valve in the pycnometer then opened and closed until the equilibrium pressure was achieved. When the pressure was balanced, a second valve opened which allowed the helium gas to enter a second chamber. The volumes of the samples were measured by change in pressure and the instrument automatically computed density using Equation 3.1. The densities are shown in Table 3.2.

$$\rho = \frac{m}{V} \qquad \textit{Equation 3.1}$$

where:

- ρ = density (g/cm^3),
- m = mass of the stones (g),
- V = volume (cm^3).



Figure 3.7: The Anton Paar Ultrapyc 3000 instrument used to measure the density of the aggregate samples.

3.2.2.3. Compacted bulk density (CBD) test

The first step to measure *CBD* was to record the initial mass (m_i), width, and depth of the empty apparatus (Figure 3.8) to determine its volume.

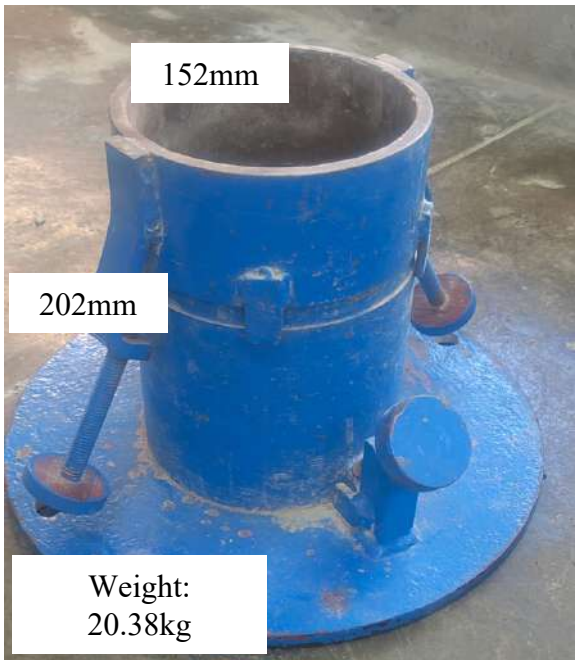


Figure 3.8: Compacted bulk density apparatus with dimensions.

One-third of the apparatus was filled with the aggregate and stamped 25 times with a metal rod along the inner edges of the apparatus to compact the aggregate. This was repeated twice to fill the apparatus. Once filled, any excess aggregate in the apparatus was cleared to achieve a flat layer of aggregate (Akbaş, 2012). Finally, the apparatus filled with the aggregate was weighed again (m_f). The density was calculated using Equation 3.1 where mass was the difference between the final and initial weight of the apparatus ($m_f - m_i$) and volume was determined using the dimensions of the apparatus. The *CBD* for each aggregate is shown in Table 3.2.

The K-value (0.9), *FM*, and *CBD* were used to calculate the stone content (*St*).

Table 3.2: The fining modulus, relative density, compacted bulk density and stone content for each aggregate.

	Dolomite	Andesite	Ferro meta-quartzite	Quartzite	Felsite
FM	3.23	3.55	2.98	2.55	3.05
RD (kg/m^3)	2805.1	2986.0	2658.2	2787.9	2681.7
CBD (kg/m^3)	1678.68	1594.06	1564.04	1588.60	1534.01
***St* (kg/m^3)**	**968.6**	**868.8**	**941.5**	**1024.6**	**912.7**

3.2.2.4. Trial mixtures

Once the stone content was determined, design mixtures for each aggregate were calculated for a 1 m^3 cube. After a suitable mixture design was determined (Table 3.3), a trial mixture and slump test (Figure 3.9) was conducted. Conducting the trial mixture began by calculating the mixture ratios based on the design requirements. The mass (kg) of each component (water, cement, stone, and sand) was determined and carefully measured. Before starting the mixing process, the concrete mixer was made wet to prevent components from sticking. The dry components (stone, sand, and cement) were added to the mixer and mixed for one minute. After this initial mixing, water was slowly added and mixing continued for an additional minute. Once the concrete mixture was prepared, one-third of the slump-testing cone was filled with the concrete while the cone was held firmly on the ground. A metal rod was used to stamp the mixture 25 times (Figure 3.9A), and the process was repeated twice until the cone was full (Figure 3.9B and C). After the third stamping, the cone was held down and lifted swiftly to expose the concrete mixture. The slump was measured by setting the cone upside down beside the concrete slump and placing the rod on top of the cone as a reference point (Figure 3.9D). The distance from the rod to the highest point of the concrete was measured as the slump.

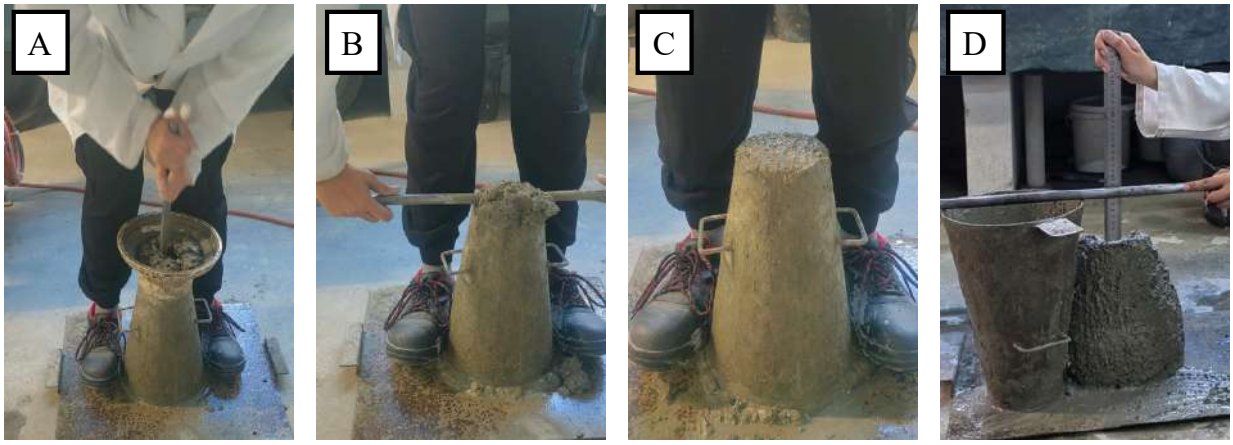


Figure 3.9: The step-by-step process to measure slump.

Table 3.3: The trial mixture designs for each aggregate type and each w/c ratio. Each mixture was leballed with a letter(s) that represents the aggregate type and a number (4 or 6) that represents the w/c ratios 0.4 and 0.6, respectively.

Aggregate	Mix no.		Water	Cement	Stone	Sand
Dolomite		ρ (kg/m^3)	1000	3140	2805.1	2805.1
	D4	m (kg)	245.0	612.5	968.6	602.1
		V (m^3)	0.25	0.20	0.35	0.22
	D6	m (kg)	240.0	400.0	968.6	805.9
		V (m^3)	0.24	0.13	0.35	0.29
Andesite		ρ (kg/m^3)	1000	3140	2986	2986
	A4	m (kg)	245.0	612.5	868.8	803.2
		V (m^3)	0.25	0.20	0.29	0.27
	A6	m (kg)	240.0	400.0	868.8	1020.2
		V (m^3)	0.24	0.13	0.29	0.34
Ferro-quartzite		ρ (kg/m^3)	1000	3140	2658.2	2658.2
	FQ4	m (kg)	245.0	612.5	941.5	546.9
		V (m^3)	0.25	0.20	0.35	0.21
	FQ6	m (kg)	240.0	400.0	941.5	740.1
		V (m^3)	0.24	0.13	0.35	0.28

Quartzite		ρ (kg/m^3)	1000	3140	2787.9	2787.9
	WQ4	*m* (kg)	245.0	612.5	1024.6	536.4
		V (m^3)	0.25	0.20	0.37	0.19
	WQ6	*m* (kg)	240.0	400.0	1024.6	739.0
		V (m^3)	0.24	0.13	0.37	0.27
Felsite		ρ (kg/m^3)	1000	3140	2681.7	2681.7
	F4	*m* (kg)	245.0	612.5	912.7	588.8
		V (m^3)	0.25	0.20	0.34	0.22
	F6	*m* (kg)	240.0	400.0	912.7	783.7
		V (m^3)	0.24	0.13	0.34	0.29

The trial mixture designs produced acceptable slumps. To conduct the UCS tests, two w/c ratios (0.4 and 0.6) were used to mix the concrete for each of the five aggregates, therefore ten mixtures were made in total. Each mixture produced nine 100×100×100 mm concrete cubes. The components for the 10-litre concrete mixtures were calculated for each mixture design and the values are recorded in Table 3.4.

*Table 3.4: The mass of each component in kilograms for a 10-litre concrete mix. *w/c = water-to-cement ratio, W = water, C = cement, St = stone, S = sand.*

	Dolomite		Andesite		Ferro meta-quartzite		Quartzite		Felsite	
w/c	0.4	0.6	0.4	0.6	0.4	0.6	0.4	0.6	0.4	0.6
W	2.45	2.40	2.45	2.40	2.45	2.40	2.45	2.40	2.45	2.40
C	6.13	4.00	6.13	4.00	6.13	4.00	6.13	4.00	6.13	4.00
St	9.69	9.69	8.69	8.69	9.42	9.42	10.25	10.25	9.13	9.13
S	6.02	8.06	8.03	10.20	5.47	7.40	5.36	7.39	5.89	7.84

The water, cement, stone, and sand components were batched. Plastic moulds with a hole at the bottom were used to cast the concrete cubes. Prior to mixing the concrete, each hole was temporarily blocked to prevent concrete from running out, and the moulds were oiled with hydraulic oil to prevent the concrete from sticking to the mould once set. Casting then began by mixing the concrete, filling the moulds, vibrating them to remove air bubbles, and then labelling each cube. Once cast, the moulds were covered with a plastic sheet to prevent water from escaping during the 24-hour hydration process. The cubes were demoulded the following day using a high-pressure hydraulic blowgun. Finally, the cubes were labelled (Figure 3.10) and submerged in a curing tank with water maintained at 23 ± 2°C.



Figure 3.10: The labelled concrete cubes for rock aggregates felsite (left) and quartzite (right). Each cube was labelled with the authors initials, the initials of the rock aggregate and a number (4 or 6) that represents the w/c ratios 0.4 and 0.6, respectively, as well as the date that the cubes were cast.

3.2.3. Thin section offcuts for Sessile Drop test

The preparatory process for these samples involved reading literature and trial-and-error to determine the most effective approach. To make the best of resources already available and to save time, the offcuts from the thin section preparation were prepared for the SD test samples. The offcuts produced during the thin section preparation were smoothed down by polishing them with 1000 grade Silicon Carbide (SiC) abrasive papers and cleaned with distilled water

and ethanol (Wei and Zhang, 2012) to remove any contaminants (Koc and Bulut, 2012). They were then dried in an oven at 105°C (Koc and Bulut, 2012; Bhardwaj and Singh, 2023) for 24 hours to eliminate any trapped water. After drying, the pieces were allowed to cool to room temperature (Bhardwaj and Singh, 2023) and stored in a desiccator to avoid moisture absorption until ready for testing. The thickness of the samples (Figure 3.11) was not crucial for determining the SFE, provided that the epoxy used in the thin section preparation did not come into contact with the probe liquids during the contact angle measurements. To measure the contact angles of the different rock aggregates, the smoothed samples had to be levelled on the Contact Angle Meter instrument to avoid inaccurate results. Therefore, the samples were stuck onto Prestik and levelled using a levelling apparatus prior to testing (Figure 3.12).

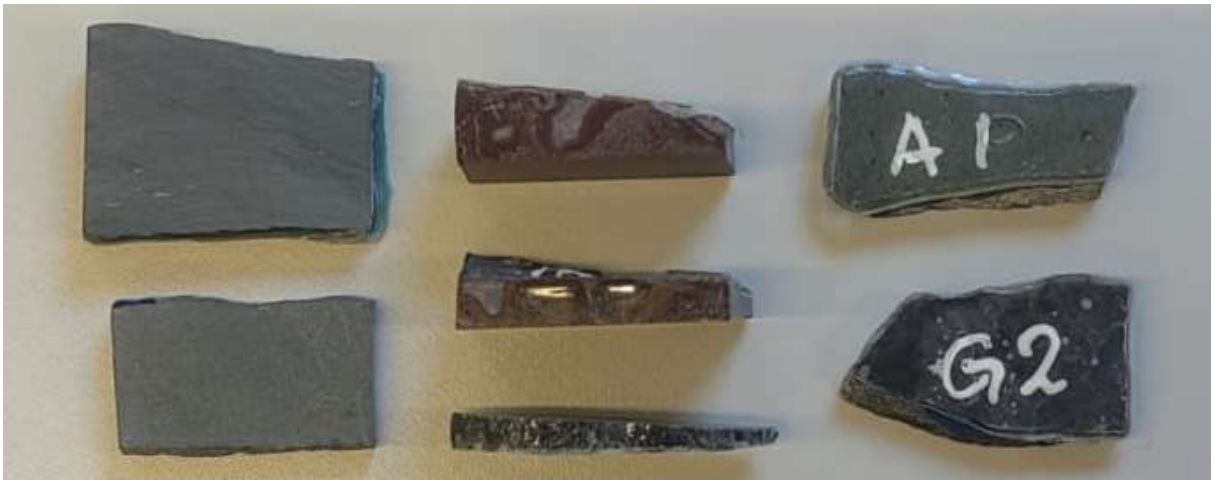


Figure 3.11: The offcuts from the thin section preparation that were prepared for the Sessile Drop method. From left to right, the image shows the smoothed surfaces, the different thicknesses and the epoxy on the unpolished side of the samples.

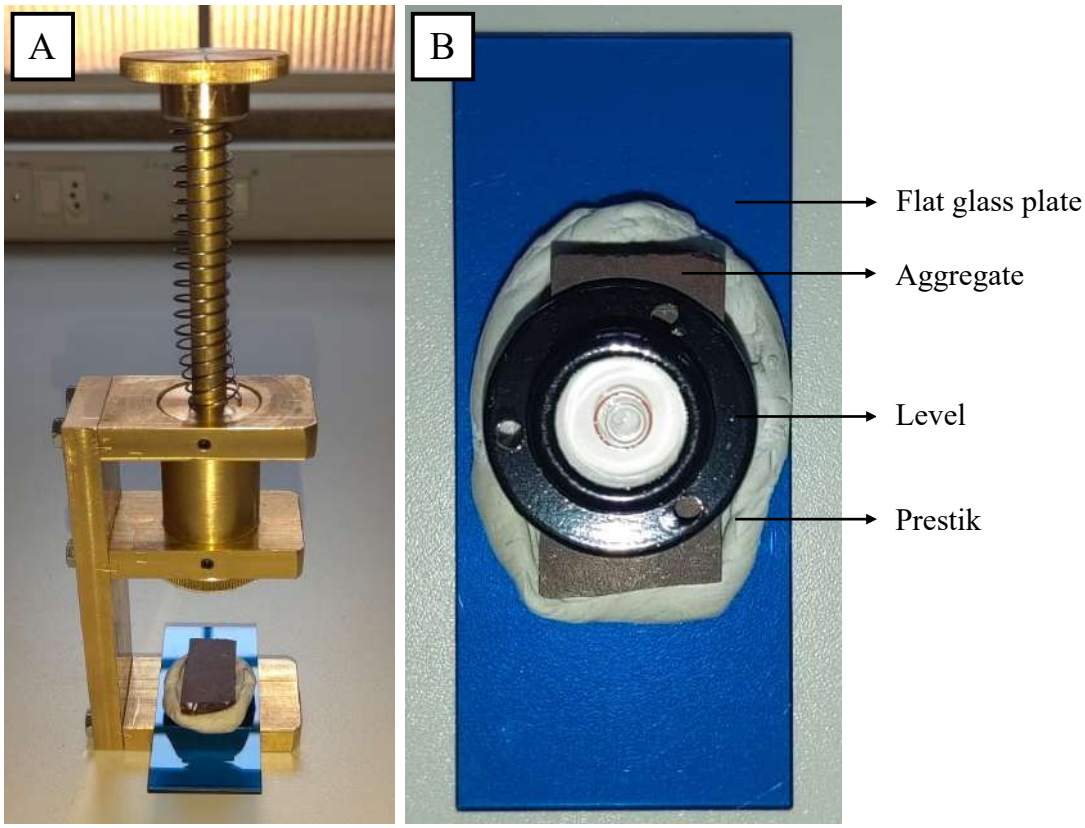


Figure 3.12: A – each sample was mounted onto a glass plate with Prestik and levelled until the bubble was in the red circle using the apparatus. As the spring was pushed down onto the sample, it became levelled in the Prestik. To ensure the sample did not get scratched during this levelling process, the top of the stamper is covered in a microfibre cloth. The sample was fixed at a levelled position during the Sessile Drop method. B – the levelled sample.

3.2.4. Rock prisms for the bond strength test

To perform the bond strength tests, two rock prisms with dimensions 160×40×40 mm were cut from boulder samples collected from each of the quarries/mines. These prisms were cut using a diamond-tipped electric cutter (Figure 3.13). Two types of andesite rocks were prepared for this test, one with amygdales and one without.

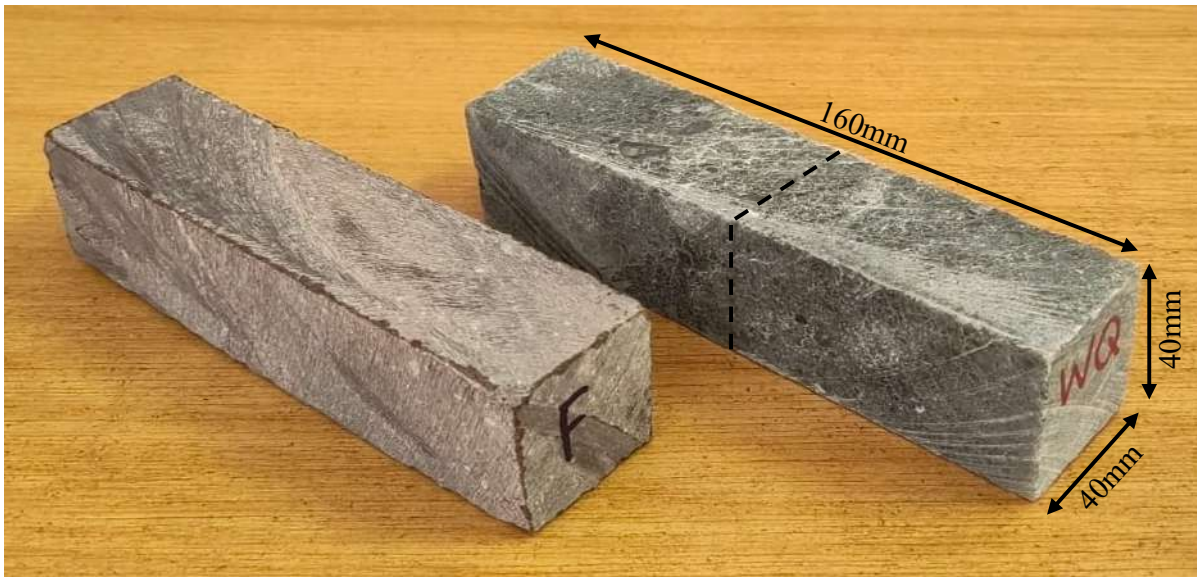


Figure 3.13: The felsite and quartzite rock prisms cut with a length of ~160 mm, and widths and heights of ~40 mm. The prisms were marked at 80 mm in length to show where it would be split.

These prisms were then split at the 80 mm mark: one prism (for each aggregate type) was cut with the diamond-tipped cutter to expose a smooth, fresh surface; and the other prism was broken in a 3-point bending test (Figures 3.14 and 3.15) to expose a rough, fresh surface. The surface of the samples broken in the bending test represents a freshly broken surface, similar to that of a crushed aggregate particle, and demonstrates macro-mechanical bonding once moulded against cement paste. The cut surfaces represent a reasonably smooth surface with macro-unevenness removed, and demonstrates micro-mechanical bonding once moulded against cement paste. This distinguishes adhesion bond from macro-mechanical bond.

The prisms that were broken in the 3-point bending test were notched in 5 mm to guide the failure pattern and ensure that the prism breaks relatively vertical. This method was appropriate and successful for rock samples with few fractures, laminations and bedding layers. Rocks that exhibit these features, such as the dolomite, broke along the weakness lines and not the notch guide.

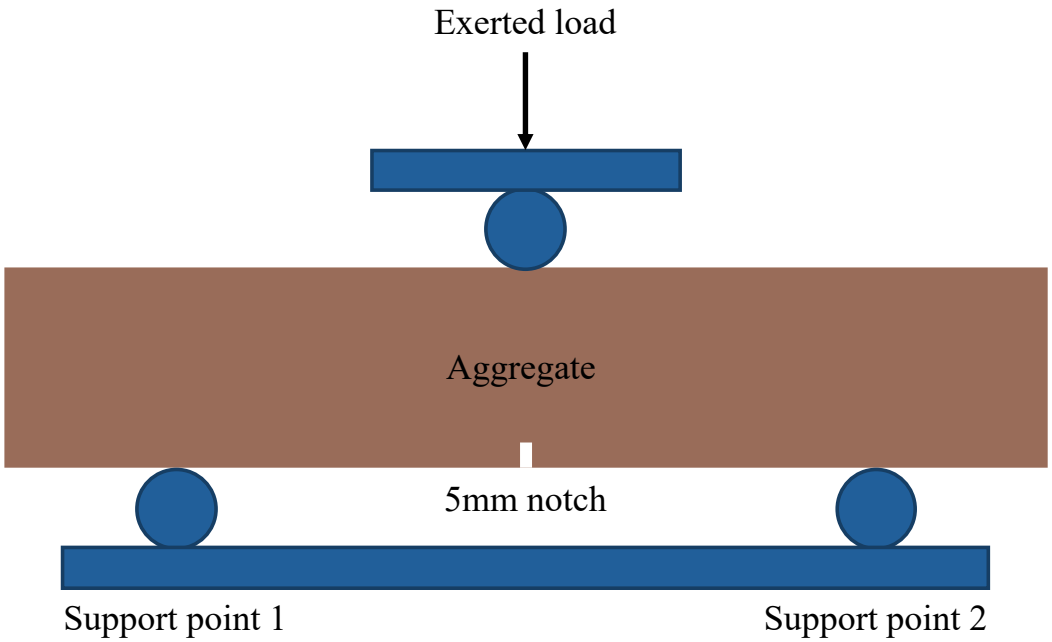


Figure 3.14: Schematic diagram showing the 3-point bending test used to break the aggregate prisms to expose a rough surface. Take note of the 5 mm notch in the aggregate that assisted in breaking the aggregate in a straight, vertical line (modified from Gu et al., 2016, p.2).

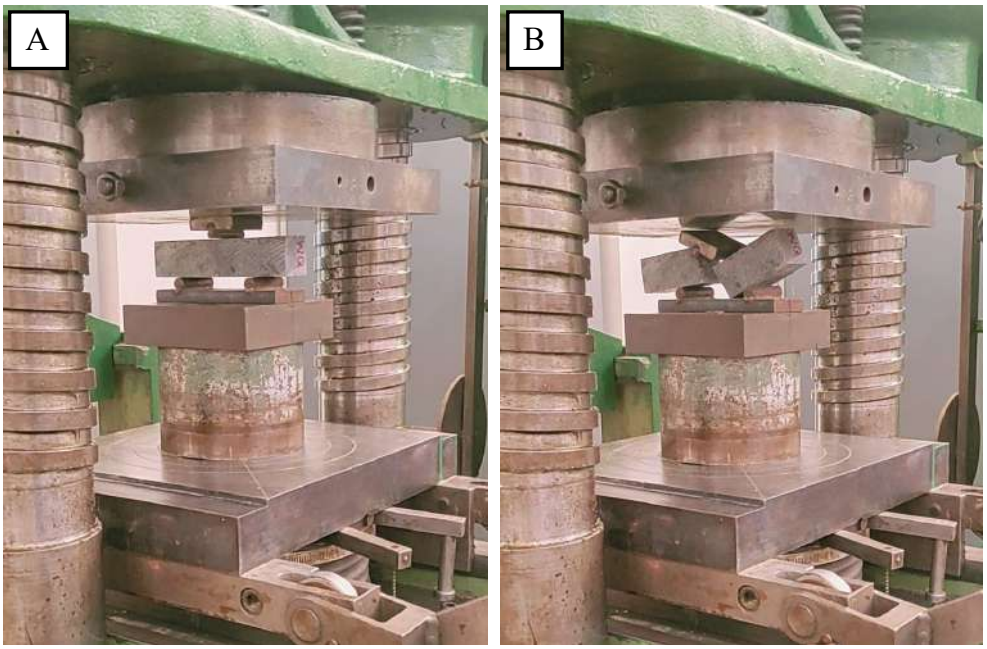


Figure 3.15: The prisms were broken using the 3-point bending test. A – the prism before breaking; B – the prism after breaking – note the relatively vertical break due to the hardness of the rock and the notch that was cut ~5 mm deep to guide the fracture and break.

The half-prisms were thoroughly cleaned with pure iso-propyl alcohol and the notches were painted over with yellow paint and a layer of Vaseline to prevent bonding over smooth surfaces on the rough-surfaced prisms (Figures 3.16A, C, E, G, I, K). Figure 3.16 shows the rough-textured surfaces (A, C, E, G, I and K), and the smooth-textured surfaces (B, D, F, H, J, L) for each aggregate type. The 3-point break for the dolomite (Figure 3.16A) is not vertical due to layering within in the rock.

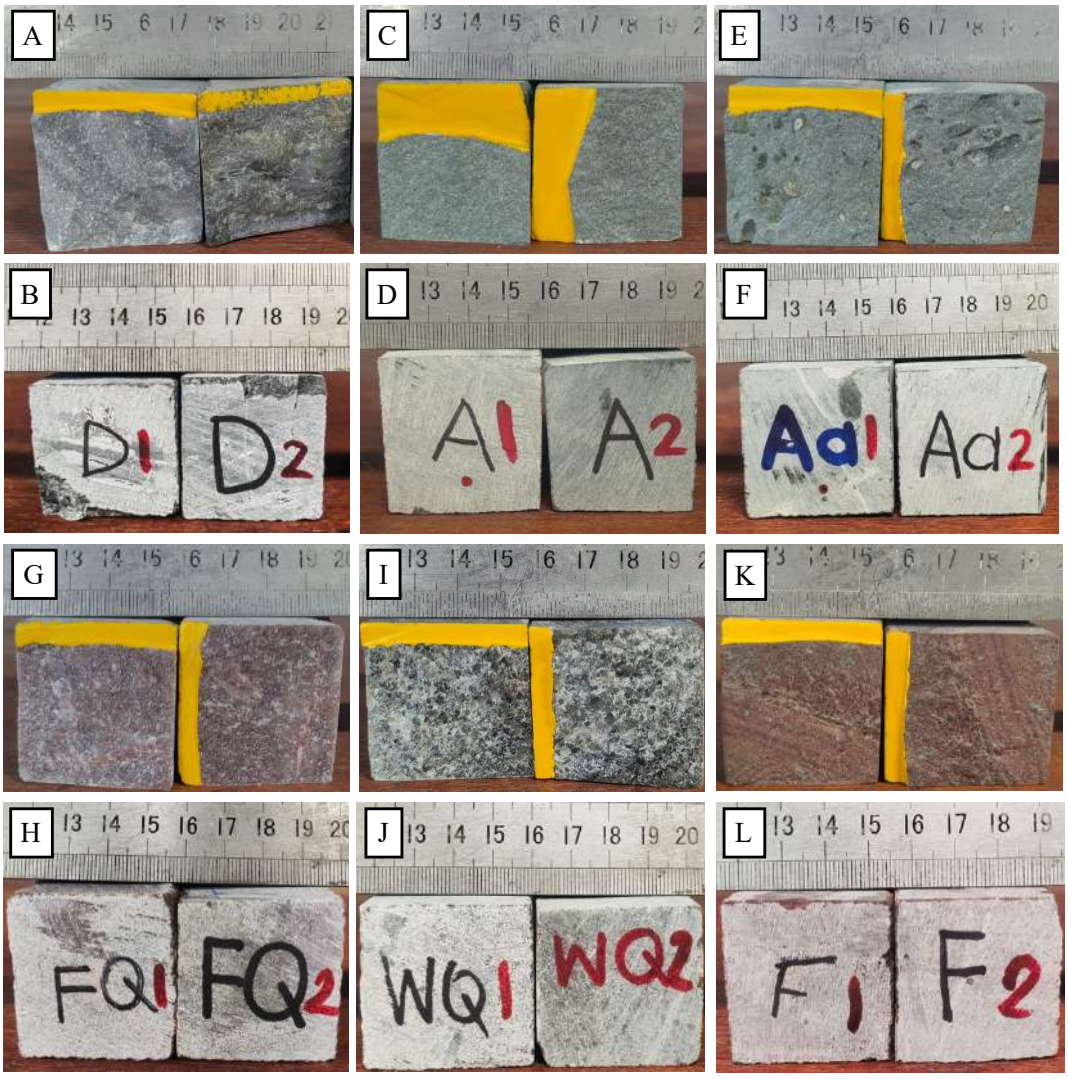


*Figure 3.16: The 5 mm notch that was cut into the prism was painted over with yellow paint and Vaseline to prevent micro-mechanical bonding when moulded against cement paste. Note that the aggregate prism in image C was unintentionally notched greater than 5 mm. *D = dolomite, A = andesite, Aa = andesite with amygdales, FQ = ferro-quartzite, WQ = quartzite, F = felsite.*

To make 24 aggregate-cement prisms, 3.5 L (0.0035 m^3) of cement paste was prepared with a w/c ratio of 0.35. This ratio mixed a relatively stiff cement paste. To enhance the workability of the mixture, the Sika Viscocrete-3088 superplasticizer was added. The volume of superplasticizer required was calculated using the density and recommended dosage of Sika Viscocrete 3088 (Chapter 2, Section, 2.3).

Table 3.5 shows the calculations used to determine the cement, water and Sika Viscocrete-3088 components.

Table 3.5: The components for the cement paste. The water and cement volumes are calculated using the w/c ratio (0.35), mass and densities. The superplasticiser volume is determined using its density and the cement mass.

	Mass (kg)	**Density (kg/m^3)**	**Volume (m^3)**
Cement	100	3140	0.032
Water	35	1000	0.035
Total			0.067
$\frac{0.0035m^3}{0.0668m^3} = 0.0524$			
Cement	**5.240**	3140	0.0017
Water	**1.834**	1000	0.0018
Total			0.0035 = 3.5L
Sika Viscocrete-3088	0.2% of cement mass	1050	0.0105 = 10.5mL

This mixture created a pancake-batter cement paste which was moulded against each smooth and rough surface, covered with plastic and allowed to hydrate for 24 hours. The aggregate-cement prisms were then demoulded (Figure 3.17) and left to cure for 28 days until testing.

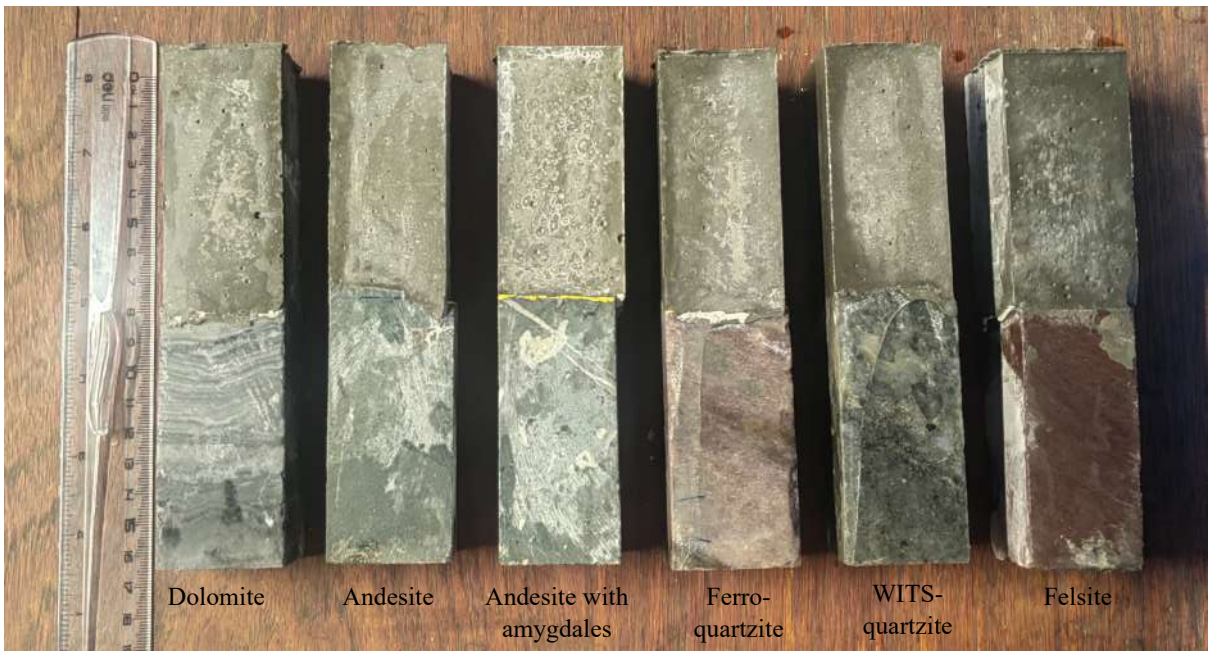


Figure 3.17: The aggregate-cement prisms showing the interface of the two phases in the centre of each prism.

3.3. Petrographic analysis

The five polished thin sections were studied using transmitted and reflected light microscopy (Figure 3.18A) at the University of the Witwatersrand (WIM Lab). A Full Section Scanning Microscope (Figure 3.18B) was used to analyse these thin sections at different magnifications and high-resolution photomicrographs of the thin sections were captured using a camera attached to the microscope. These photomicrographs provided visual representations of each thin section and its associated mineral assemblages. Individual descriptions of each sample regarding their texture, mineral assemblages, grain sizes, and alteration were conducted.

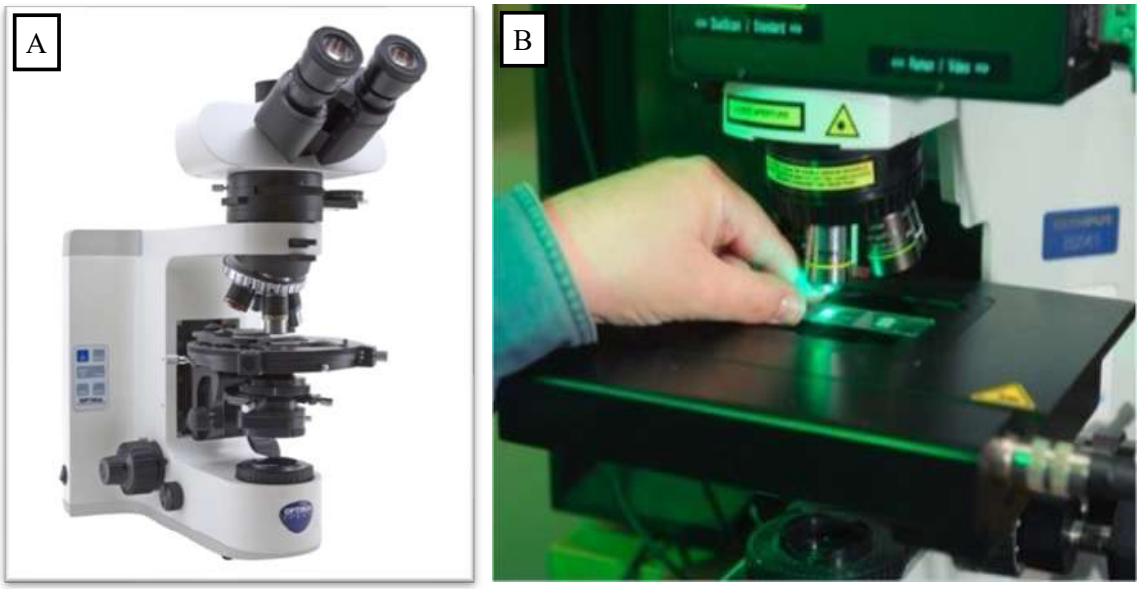


Figure 3.18: A – Polarising Microscope; B – Full Section Scanning Microscope.

3.4. TIMA analysis

Using the thin section samples, the mineral assemblages of the five aggregate samples were characterized using TIMA with VegaTCx64 tungsten hardware and TIMA software version 2.9.0 at the School of Geosciences, University of the Witwatersrand. TIMA is an automated system capable of rapidly analysing the mineral assemblage of samples. This system utilizes both Energy Dispersive X-ray Spectrometry (EDS) and Backscattered Electron (BSE) signals to identify minerals. The TIMA analysis was conducted after petrographic work, and the results from both mineral analyses were used to characterize the aggregates.

Prior to data acquisition, the thin sections were prepared and TIMA was carefully calibrated to ensure accurate and reliable measurements. The thin sections were first coated with a thin layer of carbon (Figure 3.19A). This was important to protect the integrity of the thin section sample, improve conductivity and imaging, prevent charging effects, and make accurate elemental analysis easier (Hrstka et al., 2018). The coated thin sections were fixed into a holder (Figure 3.19B) and inserted into the TIMA instrument (Figure 3.19C).

During quantitative analyses, the beam conditions on the VegaTCx64 were set at 25 kV for the electron beam, with a beam current of 4.2 nA, beam intensity of 17.5 and spot size of 533.62 nm, while maintaining a working distance of 15.00 mm. The analysis parameters on the TIMA

software including the acquisition mode, analysis type and pixel spacing were defined using (1) liberation analysis and (2) both dot and high-resolution mapping with pixel spacing set at 1 µm and 3 µm, respectively. The maximum and the minimum BSE intensities were set at 100% and 10%, respectively. The X-ray counts were set at 1000 per pixel and dot spacing was adjusted to 9.00 microns to ensure optimal resolution and coverage. BSE imaging speed was configured to 4 sµ, ensuring efficient data acquisition and analysis.

After the process ran to completion, the data was analysed during a post-processing session. This involved classifying any unclassified pixels, colour-coding the minerals and saving the desired images which included mineral maps.

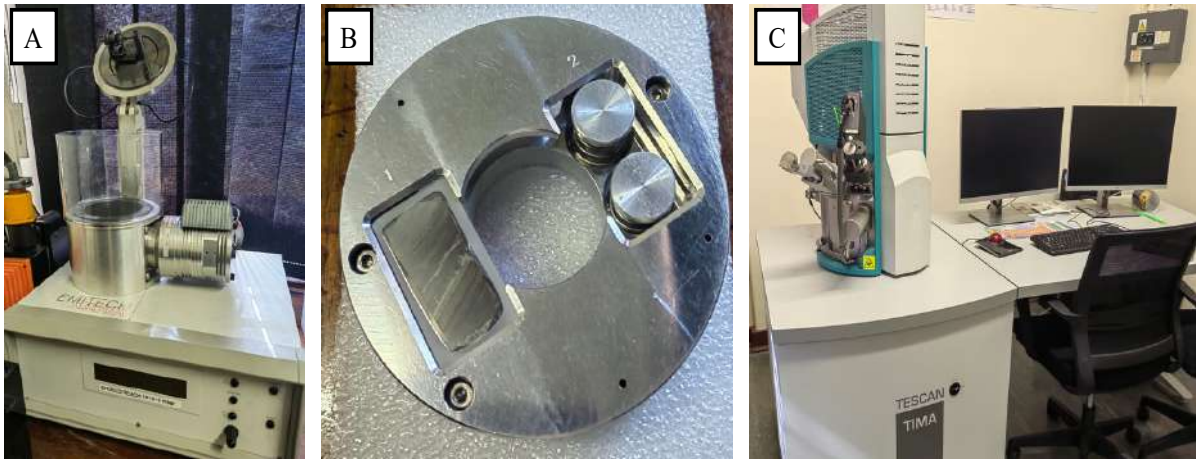


Figure 3.19: A – Carbon-coating instrument; B – Carbon-coated thin section mounted into the TIMA holder; C – TIMA instrument.

Thin sections for petrographic and TIMA analysis provided qualitative and quantitative data which was critical for understanding the mineralogical assemblages and texture of the rock. Petrography was performed prior to TIMA to serve as a foundational step, which offered a comprehensive understanding of the mineral composition, textural relationships and possible metamorphism and alteration of each sample. The petrographic baseline assisted in interpreting the qualitative and quantitative mineral assemblages, and better identify and classify the minerals detected by TIMA. TIMA identified minerals that were difficult to recognise under the microscope due to their low abundance or complex textural relationships. The TIMA analysis also provided quantitative data of major and trace minerals that were present in <0.01%. During the post-processing session, any unknown pixels were classified as best as

possible. Those that were unable to be classified remained unknown in a category named 'Other'. This category included unknown pixels, as well as minerals <0.01%

This combined approach of petrographic analysis and quantitative TIMA analysis provided a broad understanding of the mineralogical and textural characteristics of the aggregate which was important for interpreting the geological history and processes that shaped the sample. TIMA phase maps display the distribution of mineral assemblages found in a sample and provide an understanding of detrimental minerals and their potential effect on the aggregates in concrete.

3.5. Unconfined Compressive Strength (UCS) test

The compressive strength was recorded as the average of three test measurements. The concrete cubes for each rock aggregate were made with the two w/c ratios, 0.4 and 0.6. The cubes were tested over 7, 28 and 56 days after casting. Therefore, a total of 90 cubes were made for the UCS tests.

On the day of testing, each concrete cube was taken out of the water tank, wiped off of any excess water, and weighed on the measuring scale.

The compressive strength instrument has a lever that had be open at all times when concrete cubes were placed in or removed from the chamber. Rectangular spacer blocks with a dimension of 100 mm were inserted into the chamber first to ensure that the cubes were positioned in the centre of the loading plate. The cube edges were smoothed before being placed into the compressive strength instrument (Figure 3.20). The load was exerted in the normal direction in relation to the direction of casting. The test began when the lever was closed and the 'Start' button was selected. Once the concrete cube had reached its failure, the instrument automatically stopped and the failure load (kN) measurement on the screen was recorded. To remove the broken cube, the 'Stop' button was selected and the lever was opened. The interior of the chamber was cleaned and the process was repeated for each concrete cube. To calculate the compressive strength (σ) of the cube, Equation 3.2 is applied.

$$\sigma = \frac{FL}{A} \qquad \textit{Equation 3.2}$$

where:

- σ = compressive strength (MPa),
- FL = failure load (kN),
- A = area of cube face (mm^2).

The compressive strength was calculated for each of the ninety samples, provided that no malfunctions occurred during the test. An average compressive strength was recorded per mixture.

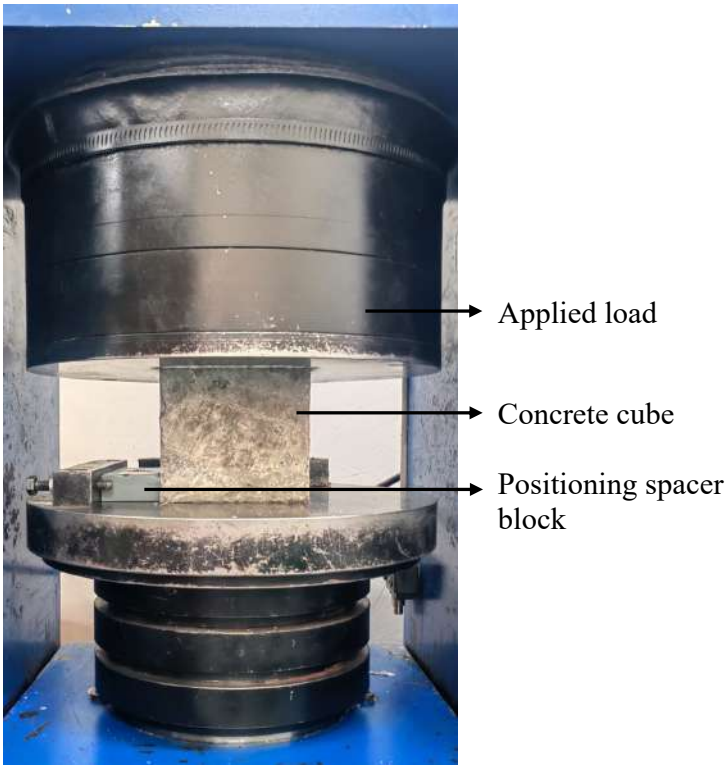


Figure 3.20: A concrete cube inside the chamber of the compressive strength instrument.

3.6. Surface free energy (SFE) analysis

The SFE of solids, surface and interfacial tension of liquids, and dynamic and static contact angles can all be measured using the small and highly effective Contact Angle Meter DMs-401 surface measuring tool. Figure 3.21 illustrates the setup of the Contact Angle Meter alongside the laptop that the InterFAce Measurement and Analysis System (FAMAS) software is installed on, and close-up images of the needle that the probe liquid is dispensed from. Its advanced modular architecture makes it simple to expand its functionality. Accessory options

include an external tilting stage system, temperature control devices, and a computer-controlled dispenser (Kyowa, 2008).

The setup and operation of the instrument and its software were relatively simple. A descriptive manual to set up the instrument and FAMAS software is available in Appendix A. Before the SFE tests began, an appropriate droplet size was determined using a trial and error method and the hydrophilicity of the aggregates.

Once the instrument was ready for operation and the droplet size was determined, a measurement sheet was selected. For this study, the [Component calculation B] (Figure 3.22) measurement sheet was opened and prepared to perform the SD method and determine the SFE. The syringe was filled with the desired liquid (water, ethylene glycol, diiodomethane) and placed in the dispenser. The dispenser and syringe were turned upside-down to remove any air bubbles by turning the discharge/suction knob. Once all the air bubbled were pushed out, the dispenser was secured onto the column of the instrument and tightened into place.

A prepared sample from the desiccator was placed onto the stage ensuring that the needle was not touching the surface of the sample. It was important to make sure that the sample was levelled and that there were no dust particles on its surface as that would affect the measurements. The green ‘Measure’ icon was selected to start a measurement. The on-screen instructions were then easily followed to form a droplet by turning the discharge/suction knob. The droplet was carefully deposited onto the sample using the stage movement handle while monitoring the screen. This motion should be performed slowly and carefully ensuring that the drop does not fall abruptly onto the sample. This process was then repeated ten times in order to calculate an average result for each aggregate and each probe liquid. Both the dynamic and static contact angles were measured as it was still uncertain which angle is more effective to record. The system then determined the SFE results of each solid based on the Lewis acid-base theory once all the contact angles were measured. The manual calculations for SFE can be found in Appendix B.

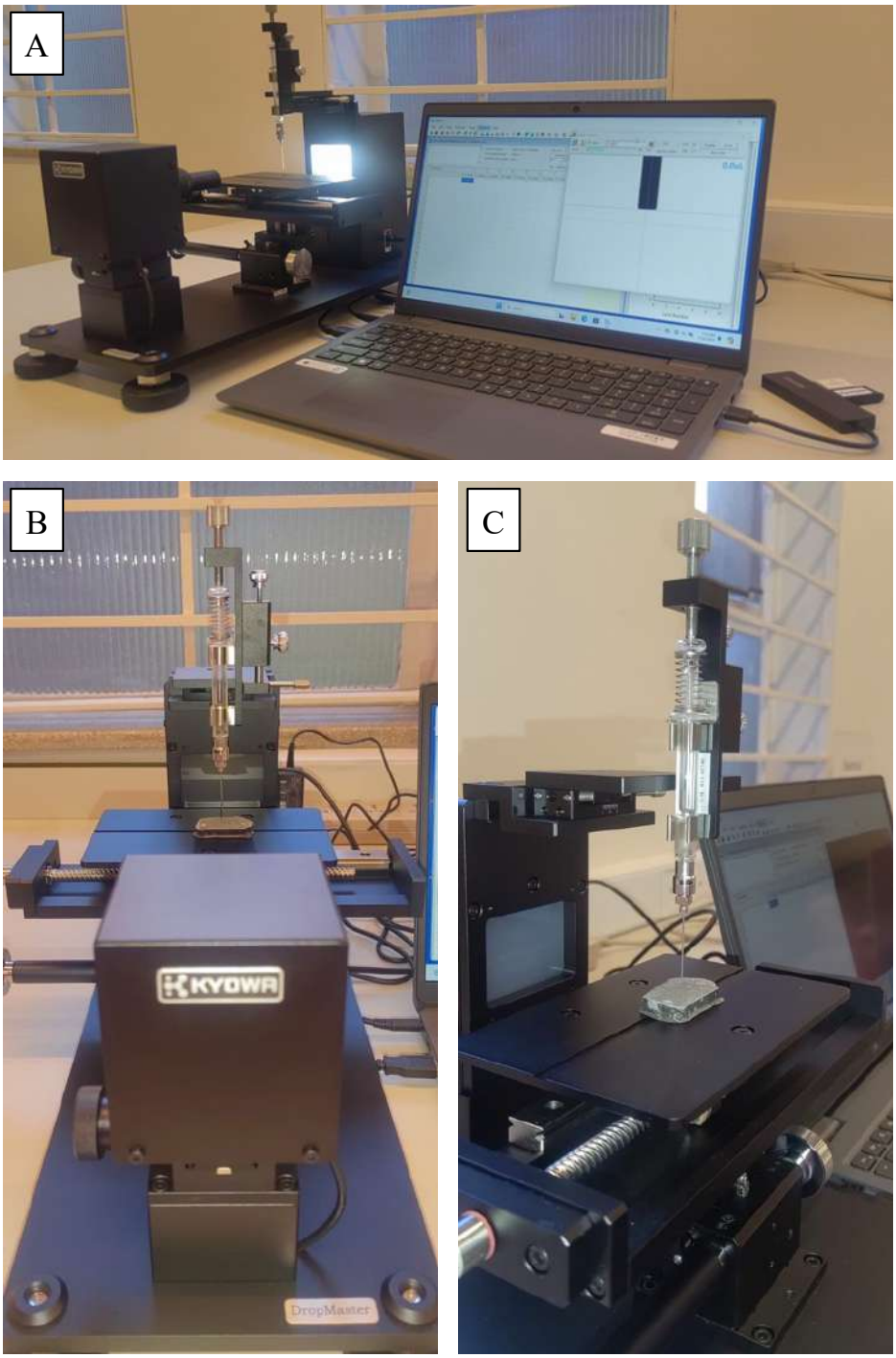


Figure 3.21: A – the setup of the Contact Angle Meter DMs-401, alongside the laptop equipped with the FAMAS software. B and C – close-up views of the syringe and needle used to dispense liquid droplets onto the smooth rock surface.

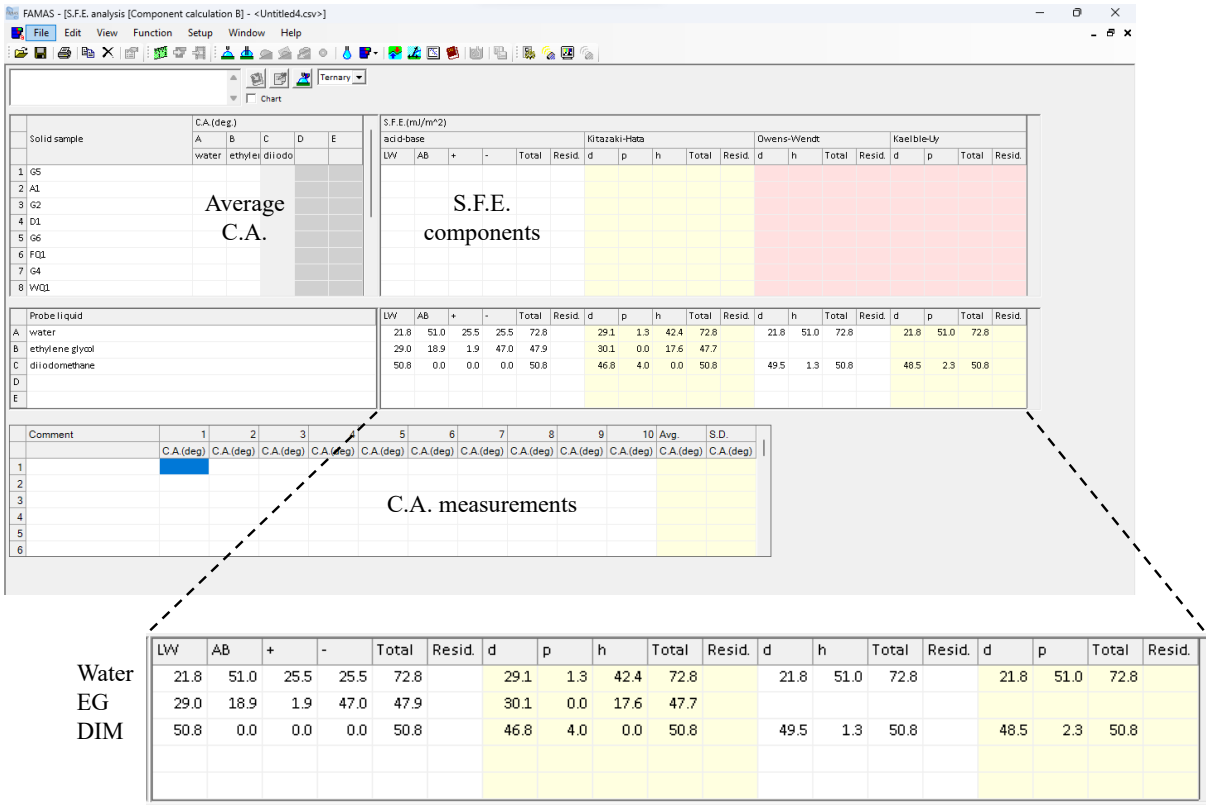


Figure 3.22: The measurement sheet for the SFE analysis [Component calculation B], including the solid sample (aggregate) names, the three probe liquids and their respective component values.

3.7. Bond strength test

Aggregate-cement prisms (~160×40×40 mm) were prepared to study the influence of the macro-mechanical and micro-mechanical bonds of adhesion and strength. The bond strength was assessed by testing the bending strength of the aggregate-cement bond, i.e. the ITZ. The smooth textured surfaces exhibited micro-mechanical bond strength, whereas the rough surfaces exhibited macro-mechanical bond strength.

After the 28-day curing period had passed, the aggregate-cement prisms (Figure 3.17) were removed from the curing tank and weighed. The bending tests were conducted on the *Losenhausenwerk Düsseldorfer Maschinebau* (Figure 3.23A). This compression-tension machine has five range of measurements (ROM) (1/1, 1/2, 1/5, 1/10 and 1/20) (Figure 3.23B) which control the maximum load applied, measured as mass (kg). ROM 1/5 and 1/10 were used to perform the tests effectively and collect accurate data.

A base plate and loading plate were chosen and their dimensions measured (Figure 3.24A). The base plate was placed at the centre of the compression section. The aggregate-cement prism was then positioned centrally on the base plate, followed by the loading plate, which was aligned with the interface of the aggregate-cement prism (Figures 3.24B and C). This positioning ensured an even load was being applied to the prism. Once the machine and sample was set up, the load was applied by pulling the lever backwards at small rates to avoid shocking the prism. When the aggregate-cement bond failed and the prism broke, the load (kg) on the scale was recorded. This load, together with the height (b) and width (d) of the fresh aggregate surface, the base plate dimensions and the force of gravity, were used to calculate the force (P) and the bending strength (σ). These component values were calculated using Equations 2.11 and 2.14, respectively.

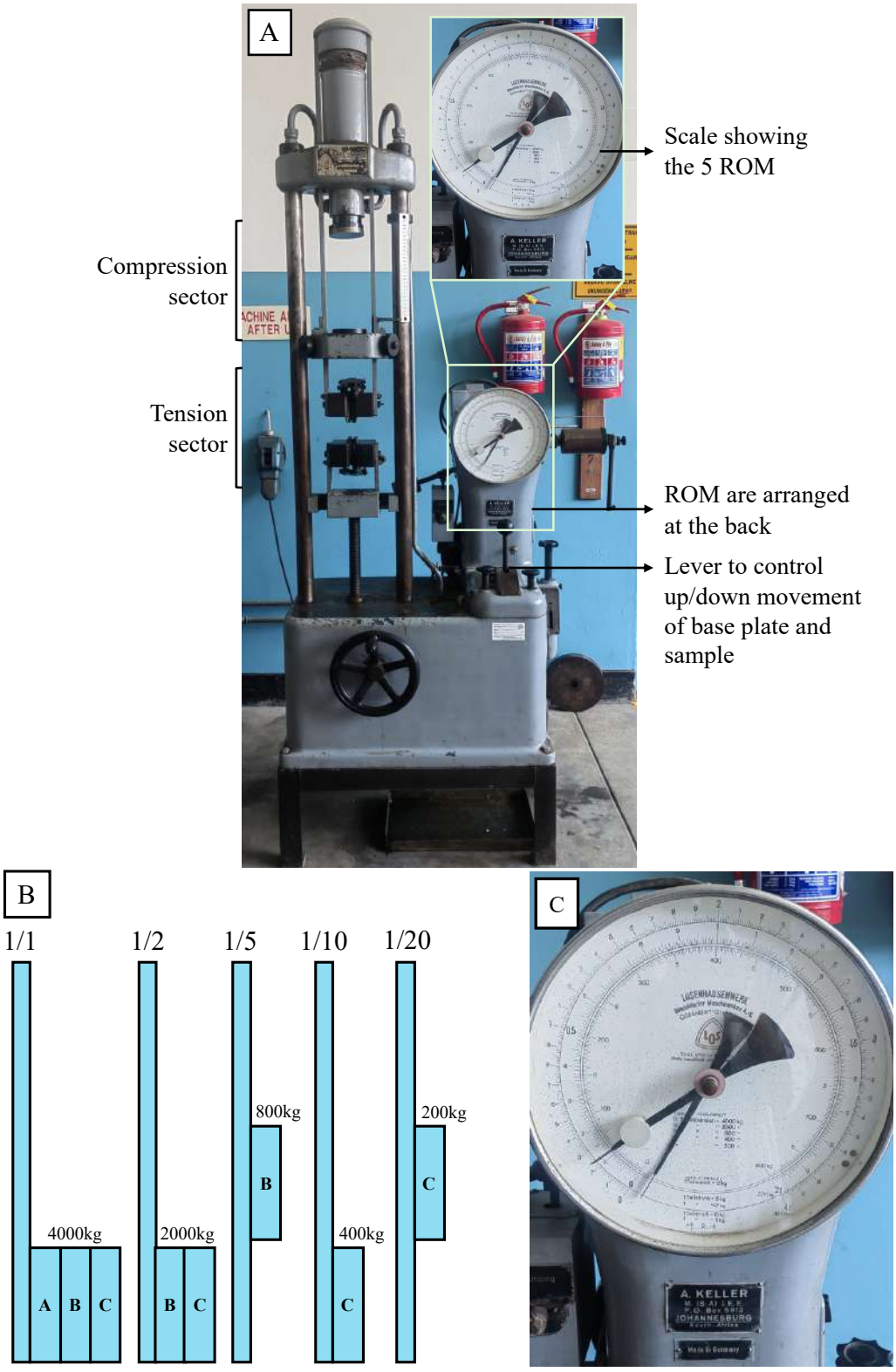


Figure 3.23: A – the Losenhausenwerk Düsseldorfer Maschinebau compression-tension testing machine showing each of the sectors (compression and tension), the scale and the lever that is used to control the sectors. B – the scale can be arranged in five ways depending on the ROM selected. C – the outer scale is used for the 1/1 and 1/10 ROM, the middle scale for the 1/2 and 1/20 ROM, and the inner scale for the 1/5 ROM.

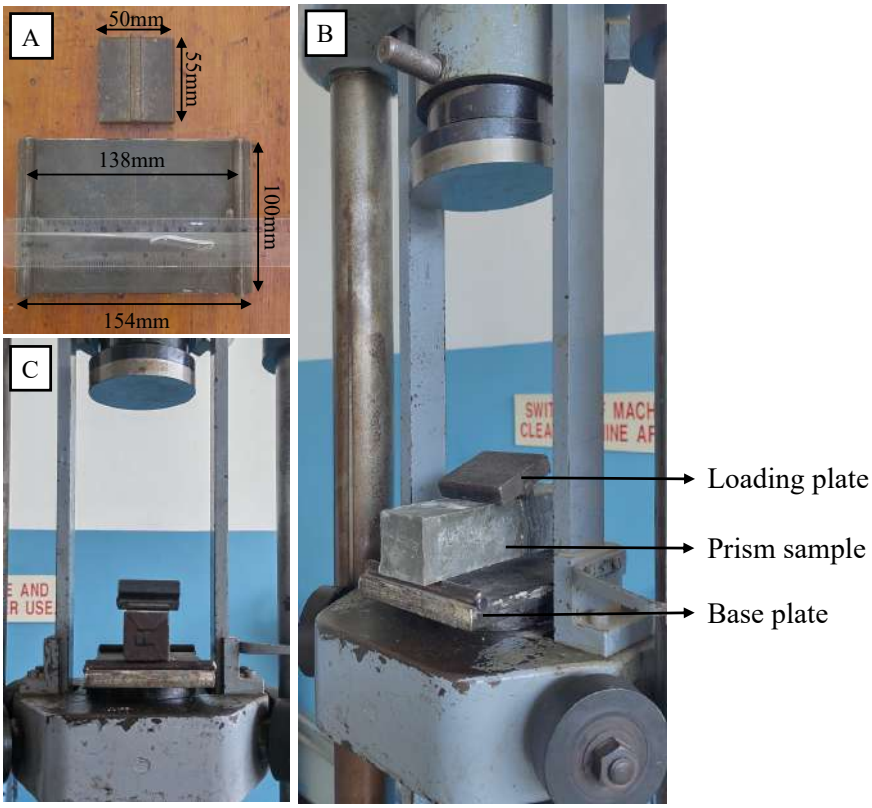


Figure 3.24: A – the dimensions of the base plate and loading plate. B and C – the positioning of the base plate, the prism and the loading plate on the interface of the aggregate-cement prism.

While this study employed the 3-point bending test to assess the bond strength between aggregate and cement, it is acknowledged that this method induces both bending moment and shear force, particularly in the central region of the beam. As illustrated by the bending moment diagram in Chapter 2 (Section 2.2.5.4), the peak moment in a 3-point test coincides with the region of maximum shear stress. This is unlike the 4-point bending test where a constant moment region allows for the reduction of shear influence. Therefore, the 3-point test does not completely isolate the tensile bond strength from shear effects. Nevertheless, the aim of this study was not to eliminate shear or mechanical interlock effects, but rather to ensure a consistent surface condition across aggregate types. While the cut surfaces may still exhibit micro-mechanical bond, they provide a more uniform and controlled macroscopic roughness compared to the variability in broken surfaces. A more accurate comparison of micro-mechanical bonding would require further polishing to a glass-like finish, and testing isolated tensile strength would require the 4-point bending test, both of which were outside the scope of this study.

Chapter 4: Results and discussion

The results collected in this study is recorded and discussed in Chapter 4 (Figure 4.1). A comparative analysis of the results follows in Chapter 5.

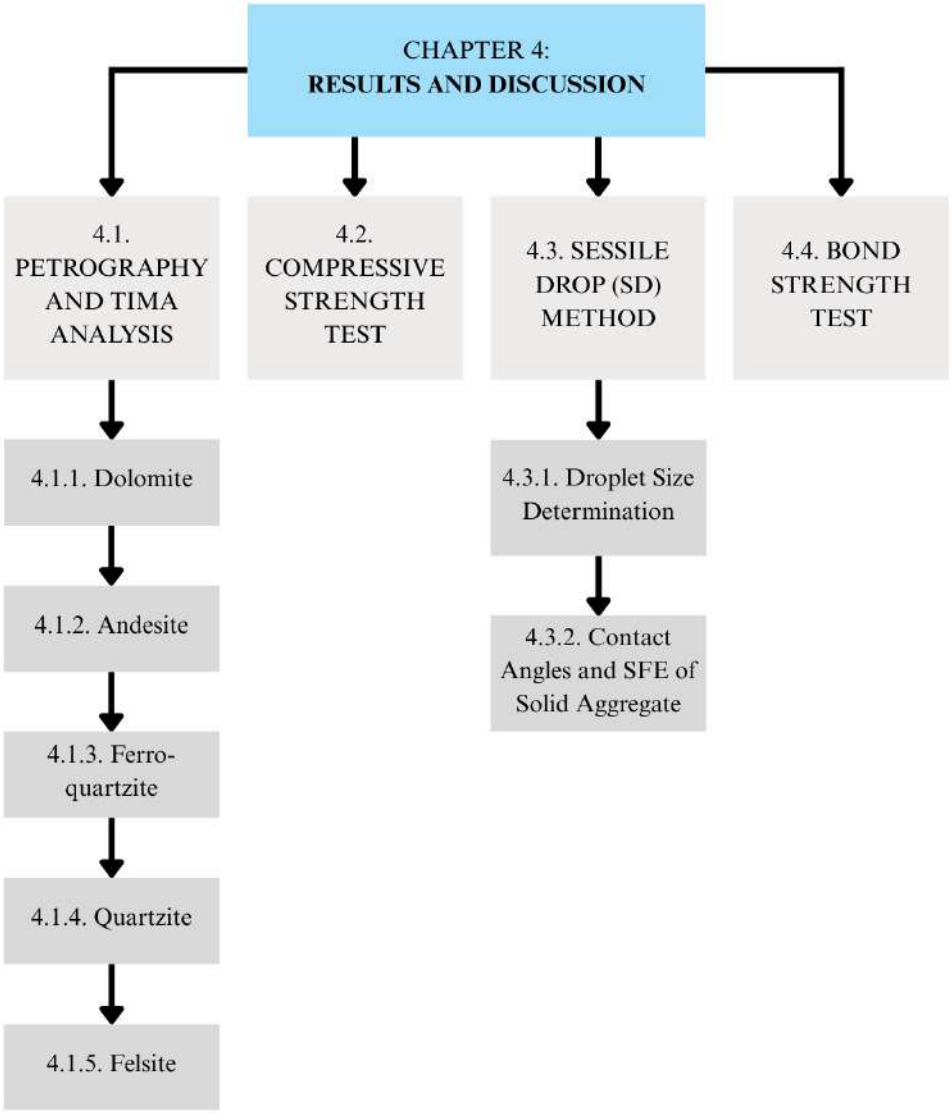


Figure 4.1: A flow diagram showing the structure of Chapter 4.

4.1. Petrography and TIMA

Each aggregate sample was characterised by colour on the weathered and fresh surfaces, the structural features, the mineral composition, the grain/crystal size and shape, the texture, as well as the alteration and the degree of alteration.

4.1.1. Dolomite

The dolomite aggregate appears dark grey on the weathered surface and produces a white streak. On the fresh surface, it exhibits various shades of grey and is primarily composed of the mineral dolomite, interlayered with chert, with minor quartz veins present. Banding is evident characterized by alternating layers of dolomite and chert (Figure 4.2).

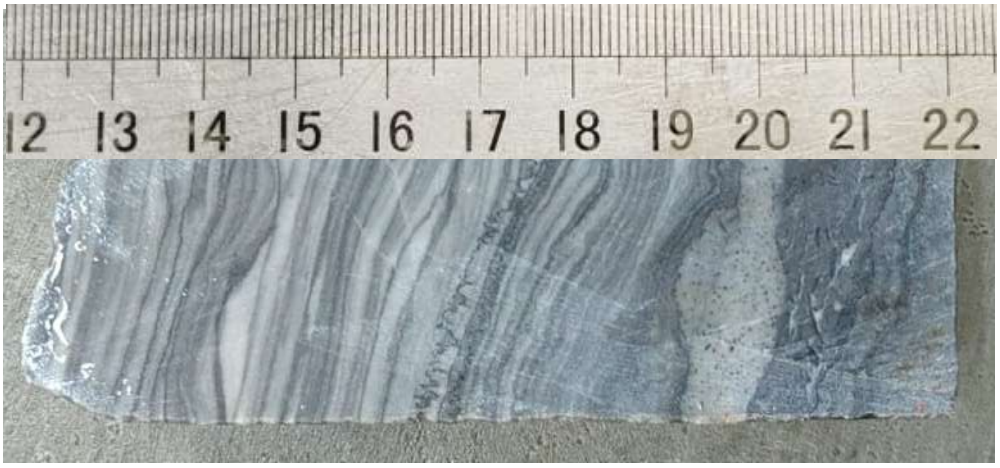


Figure 4.2: Hand specimen of the dolomite sample showing the dolomite-chert foliation.

Figure 4.3A of the plane-polarized light (PPL) image displays the layers of complete and partial dolomitization. In partially dolomitized regions, the dolomite crystals retain its rhombohedral crystal shape. This habit is obscured in areas of complete dolomitization and crystal overgrowth. This overgrowth results in a distinctive high birefringence under crossed-polarized light (XPL) (Figure 4.3B), producing a spectrum of colours (black, blue, green, purple and white) that indicate the interaction between dolomite mineralogy and polarized light. The dolomite crystals appear interlayered with finer chert and, in some areas, are surrounded by coarser-grained, secondary hydrothermal quartz lenses and veins (Figures 4.3C and D). The chert display colours of blue, black, grey and white, while the quartz crystals display orange and yellow (Figure 4.3D).

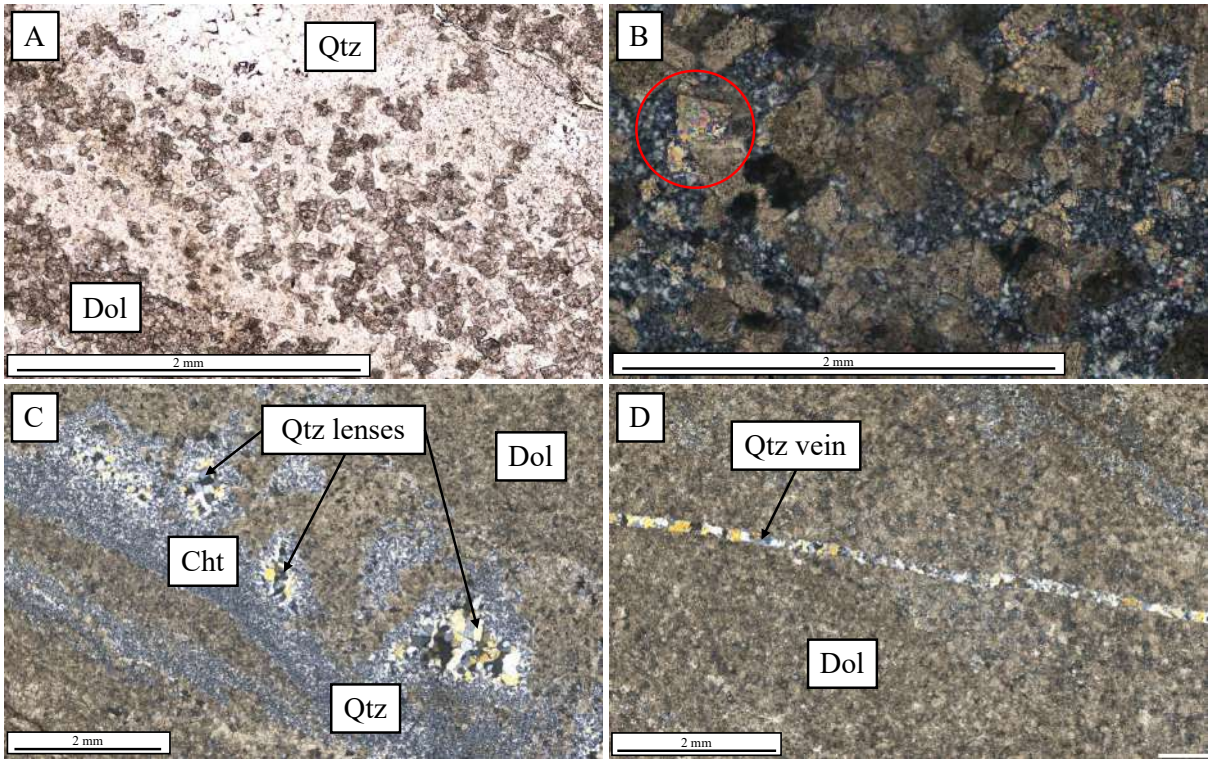


*Figure 4.3: A – PPL image showing complete and partial dolomitization, as well as the rhombohedral-shaped dolomite crystals. B – XPL image showing the high birefringent colours of the dolomite crystals. C – XPL image showing the dolomite-chert layers and the coarser-grained quartz lenses. D – XPL image showing a quartz vein. *Qtz = quartz, Dol = dolomite, Cht = chert.*

Under petrographic analysis, dolomite, chert and quartz crystals are easily identifiable. TIMA detected 47.19% dolomite and 46.20% SiO_2-minerals which includes the chert and quartz lenses and veins. Additionally, TIMA also detected trace minerals, including diopside (3.25%), calcite (2.48%), and mica (0.02%) (Figure 4.4) that are difficult to identify under polarized light. The presence of diopside indicates that the dolomite underwent high-grade metamorphism. This combined analysis underscores the intricate dolomitization process that shapes the microstructure of the dolomite.

Importantly, the rock contains very few detrimental minerals. However, quartz veins (Figure 4.3D) suggest the presence of fractures. While some fractures have been filled with silica-rich fluid, unfilled fractures could compromise the compressive strength and bond strength of concrete made with dolomite aggregate.

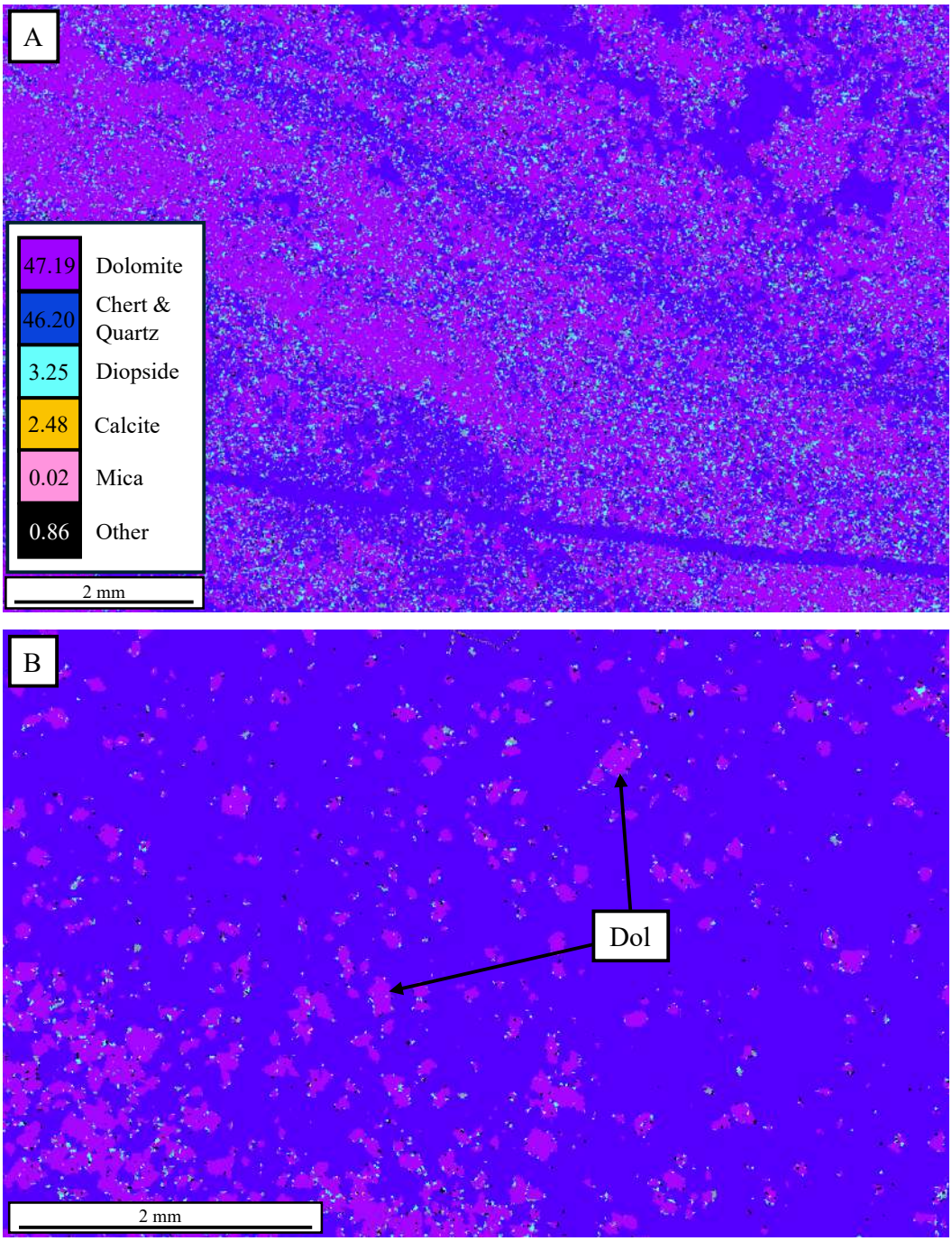


Figure 4.4: A – TIMA image of the dolomite sample showing the dominant dolomite and SiO_2-minerals crystals, as well as diopside and minor calcite and mica crystals. B – TIMA image showing the rhombohedral dolomite crystals.

4.1.2. Andesite

The andesite is light grey in colour on both its weathered and fresh surfaces. It exhibits two distinct textures, a homogenous aphanitic texture (Figure 4.5A) and an amygdaloidal or vesicular texture, containing silica-rich amygdales and veins (Figures 4.5B and C).

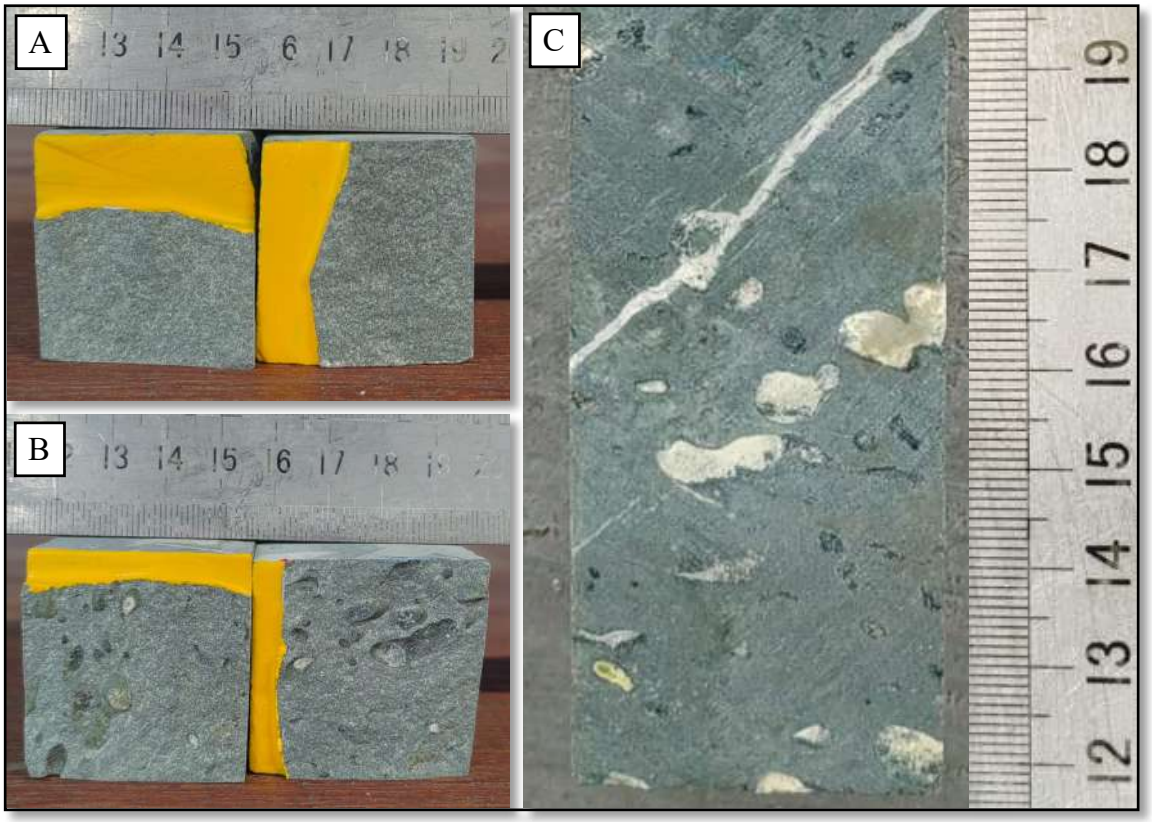


Figure 4.5: A - hand specimen of the aphanitic andesite sample. B and C – hand sample of the andesite sample showing the siliceous amygdales and veins.

Under XLP, the sample consists predominantly of dark-hued crystals, constituting approximately 90% of the composition (Figure 4.6A). The groundmass is composed of quartz crystals, plagioclase that display twinning in sharp and elongate crystals, epidote as dark green and elongate crystals, and hornblende as brown and elongate crystals. Hornblende suggests metamorphism of the andesite to amphibolite facies. Therefore, these minerals contribute to the mineralogical complexity, making petrographic analysis difficult. Figure 4.6B illustrates the quartz veins observed in the hand sample (Figure 4.5C).

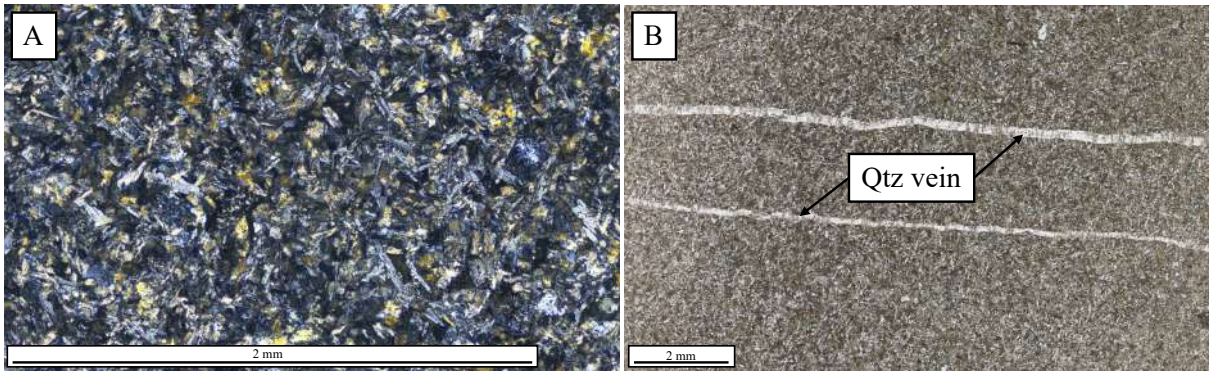


Figure 4.6: A – XPL image showing the homogenous, aphinitic texture of the andesite. B – PPL image showing the quartz veins that run through the andesite.

TIMA refined the mineralogy and quantified the identified minerals with significant mass percentages. TIMA identified the following minerals: zoisite (39.87%), quartz (20.17%), hornblende (17.41%), feldspar (8.31%), pyroxene (2.34%), dolomite (0.44%), mica (0.38%), and calcite (0.04%). Furthermore, trace minerals and unclassified pixels account for 4.03% of the total composition. Zoisite and hornblende are members of the epidote and amphibole groups, respectively. Hornblende and pyroxene indicate that the andesite is magmatic, and zoisite indicates that it underwent low-grade metamorphism and that these minerals are most likely secondary.

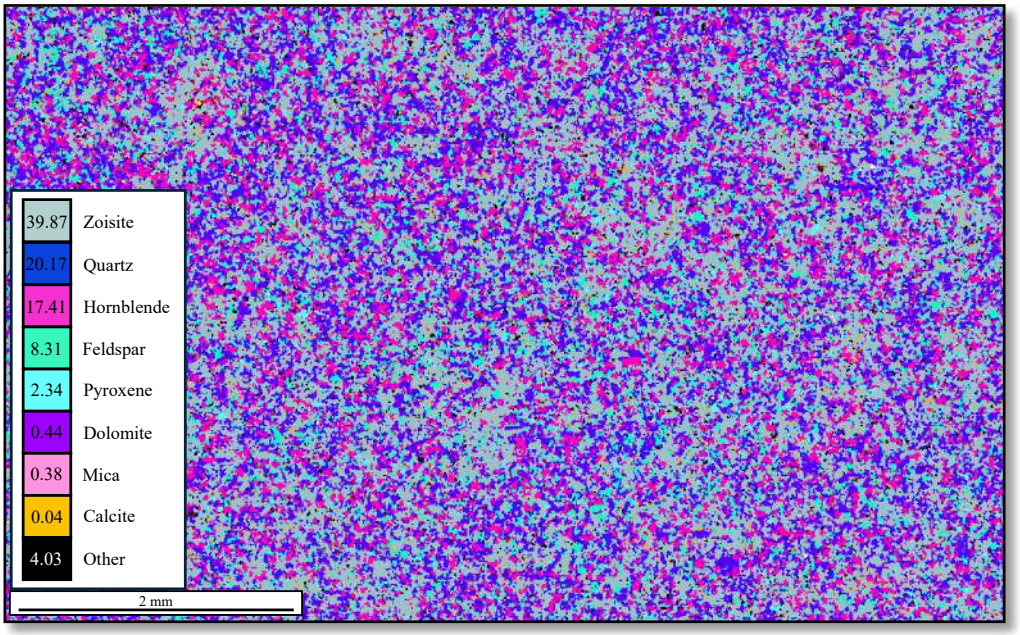


Figure 4.7: TIMA image of the andesite sample showing the homogenous, aphanitic texture.

4.1.3. Ferro-quartzite

The ferro-quartzite sample has shades of red, grey and white on the weathered and fresh surface (Figure 4.8A). It is predominantly composed of quartz, which makes up nearly 100% of the rock, displaying a range of grain sizes (Figure 4.8B).

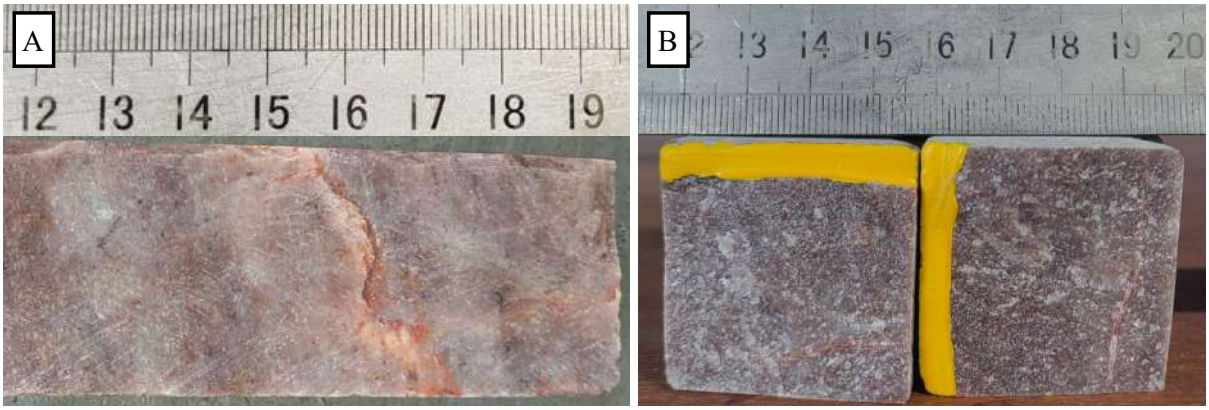


Figure 4.8: Hand specimen of the ferro-meta quartzite.

The quartz grains exhibit an interlocking phaneritic texture (Figure 4.9), characteristic of metamorphic recrystallization. A minor proportion of mica (0.56%), likely muscovite, detected through the TIMA analysis is scattered among the quartz grains. Under XPL, these mica grains display high birefringence (Figure 4.9), with colours ranging from orange and pink to blue, green, yellow, and purple. TIMA identified iron-rich minerals, hematite and/or magnetite (0.12%) (Figure 4.10), that are present in small amounts but are significant enough to influence the classification of the rock and its geochemical characteristics. Their occurrence suggests that iron-bearing fluids may have interacted with the protolith during metamorphism, or alternatively, that these iron minerals were incorporated during sedimentary deposition and subsequently altered by metamorphic processes. Additionally, the sample contains minor calcite (0.01%) and 0.35% minerals with mass fractions below 0.01%, along with some unclassified pixels.

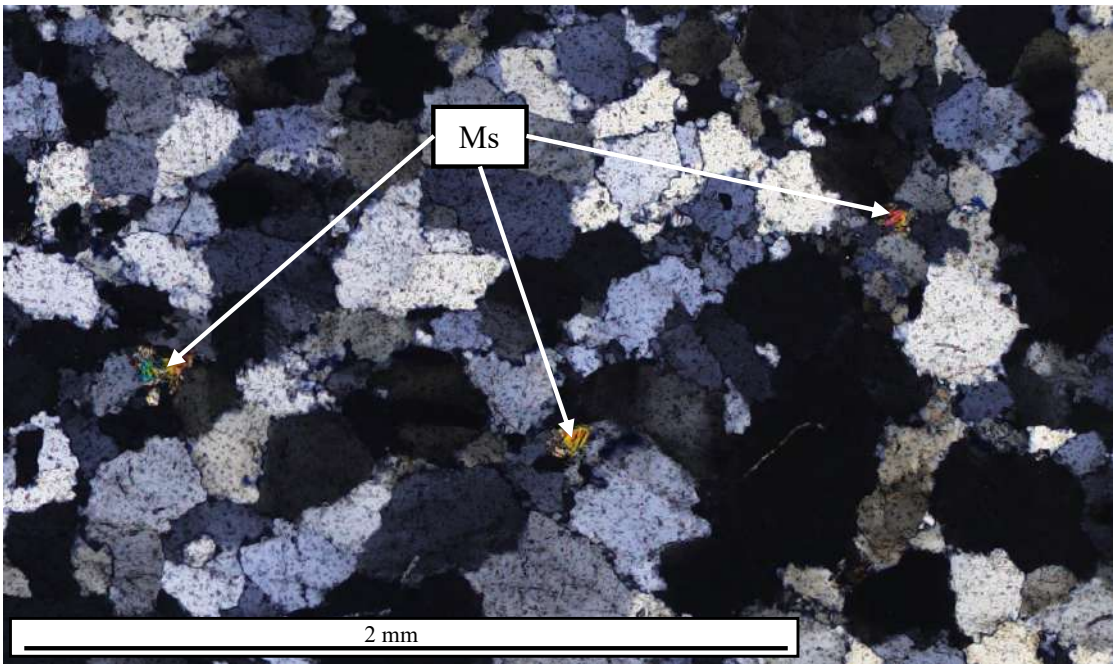


*Figure 4.9: XPL image showing the inlocking quartz crystals that give the ferro-quartzite its phaneritic texture, and the scattered musovite mica. *Ms = muscovite.*

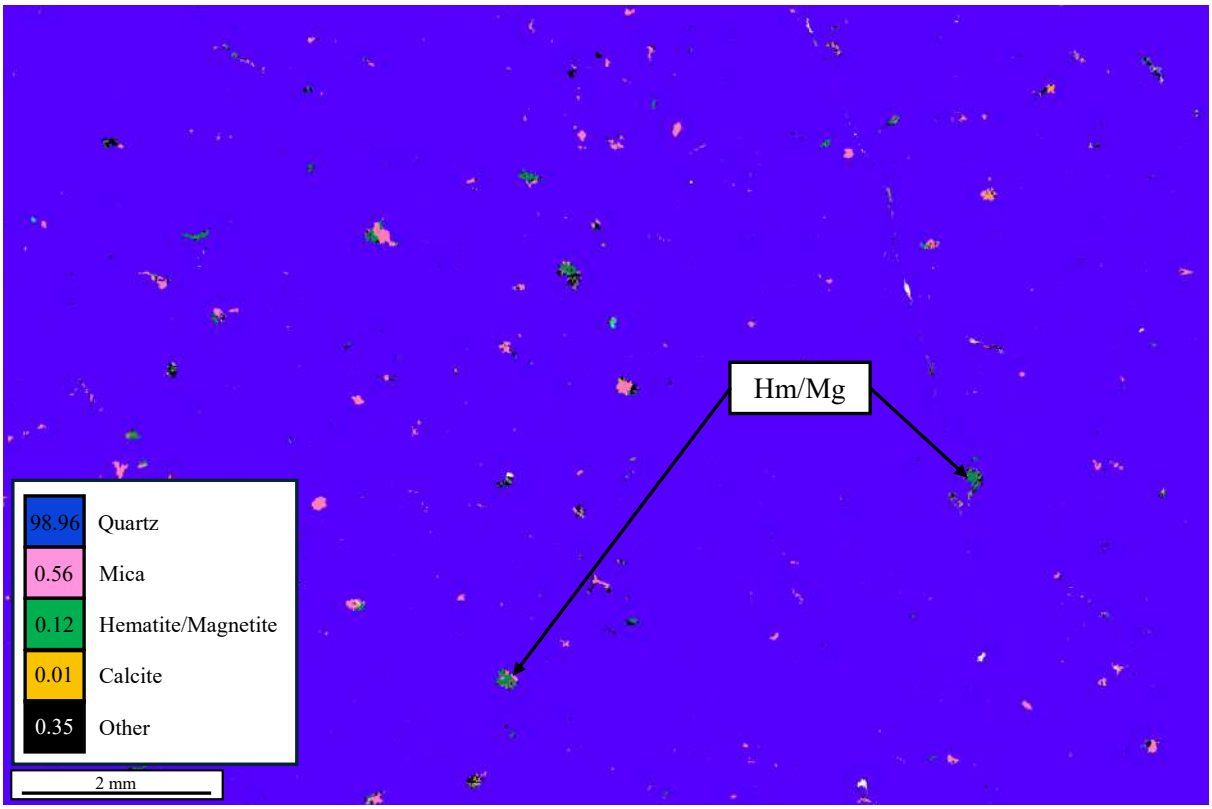


*Figure 4.10: TIMA image showing the scattered Fe-rich minerals in the ferro-quartzite. *Hm/Mg = hematite/magnetite.*

4.1.4. Quartzite

The quartzite is orange in colour on the weathered surface and shades of grey and white on the fresh surface (Figure 4.11). It is predominantly composed of quartz, making up approximately 90% of the rock.



Figure 4.11: A – hand specimen of the quartzite. B – the coarse quartz crystals of the quartzite.

The quartz crystals are coarse (2-3 mm in size), unsorted, and anhedral (Figures 4.12A and B). They are set within a metamorphosed argillaceous matrix composed of muscovite mica exhibiting high birefringent colours, including orange, green, blue, purple, and yellow (Figure 4.12A). The quartzite contains some polycrystalline quartz (Figures 4.12C and D) which form during regional metamorphism and recrystallisation. Its disconnected nature increases the porosity of the quartzite which decreases its resistance to weathering and its compressive strength.

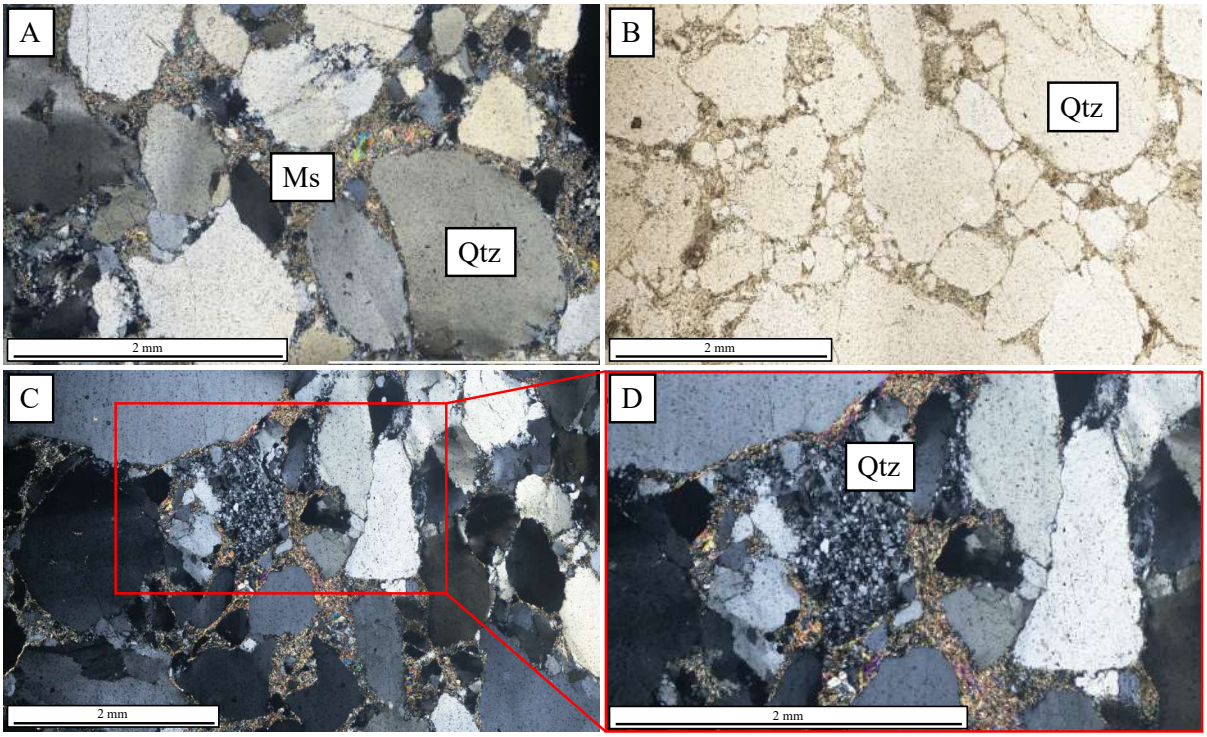


Figure 4.12: A – XPL image showing the coarse, unsorted, anhedral quartz grains surrounded by muscovite mica. B – PPL image showing the quartz and muscovite mica. C and D – XPL images showing the polycrystalline quartz.

Trace amounts of additional minerals detected through TIMA include amphibole (0.04%), calcite (0.02%), and feldspar (0.01%). TIMA quantified muscovite as 7.76% and Figure 4.13 displays the interconnected pattern of the argillaceous muscovite matrix that disconnects the quartz crystals from one another. This pattern suggests that the protolith of the quartzite prior to its metamorphism was most likely a sandstone interbedded within a mudstone or shale. The significant mass percent of muscovite mica present in the aggregate not only contributes to the interpretation of the metamorphic history of the quartzite but also influences the concrete performance. As mentioned in Chapter 2, mica is a detrimental mineral to aggregates in concrete due to its flaky texture and 2.5 ranking on the Mohs hardness scale which weakens the structural integrity of concrete structures.

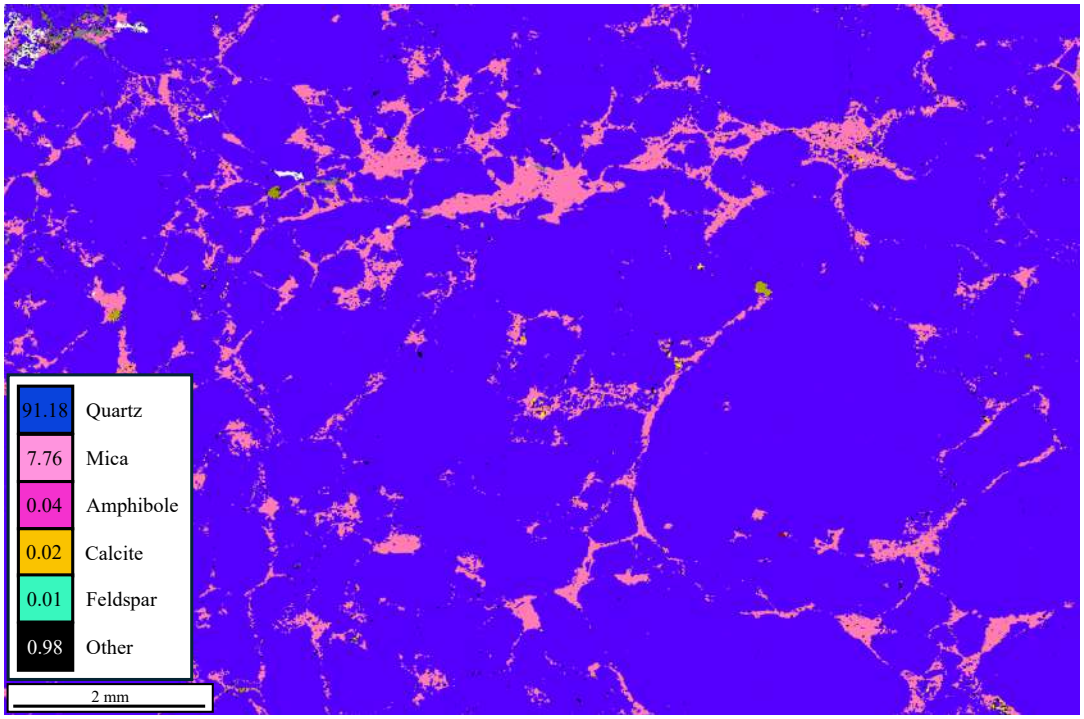


Figure 4.13: TIMA image showing the interconnected pattern of the muscovite mica around the quartz crystals.

4.1.5. Felsite

The felsite is red in colour on its weathered and fresh surfaces. It has a porphyritic texture and contains coarse feldspar phenocrysts (~2 mm) that are embedded within a fine-grained groundmass (Figure 4.14).

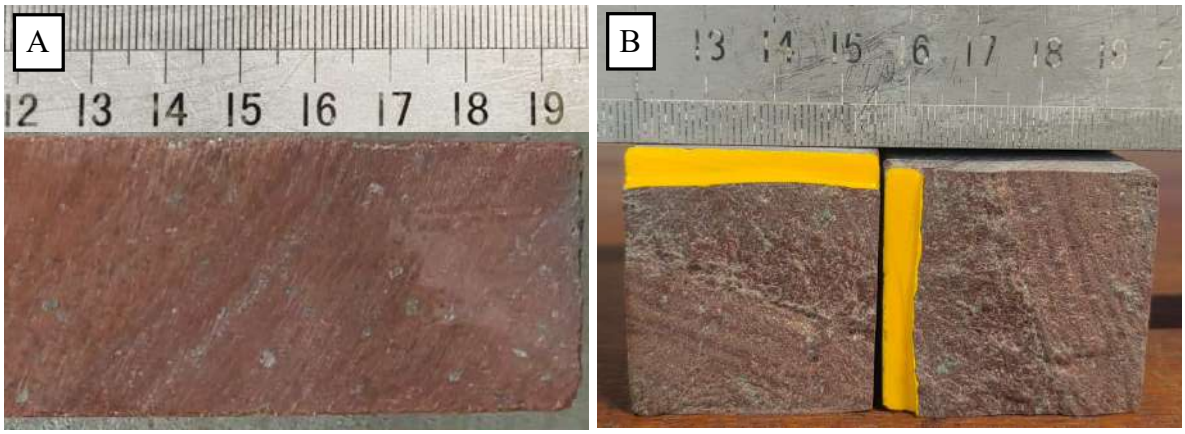


Figure 4.14: Hand specimen for felsite showing phenocrysts of ~2 mm within a fine-grained groundmass.

Under XPL, the feldspar crystals are irregularly shaped, they vary in size between 0.5 mm and 3 mm and are embedded in an altered quartz-rich matrix (Figure 4.15A). In some instances, the feldspar crystals appear fractured (Figure 4.15B). However, after analysing the TIMA data, the feldspar crystals emerge morphed with other minerals such as muscovite mica and calcite (Figures 4.15C and D). Additionally, there are opaque, oxide minerals scattered across the sample.

TIMA quantified the composition of the groundmass as a complex combination of quartz (68.86%), feldspar (13.46%), muscovite mica (12.35%), calcite (1.94%), ferro-minerals (1.14%), zoisite (0.06%), amphibole (0.04%) and dolomite (0.01%). Additionally, there are 0.35% minerals with mass fractions below 0.01%, along with some unclassified pixels.

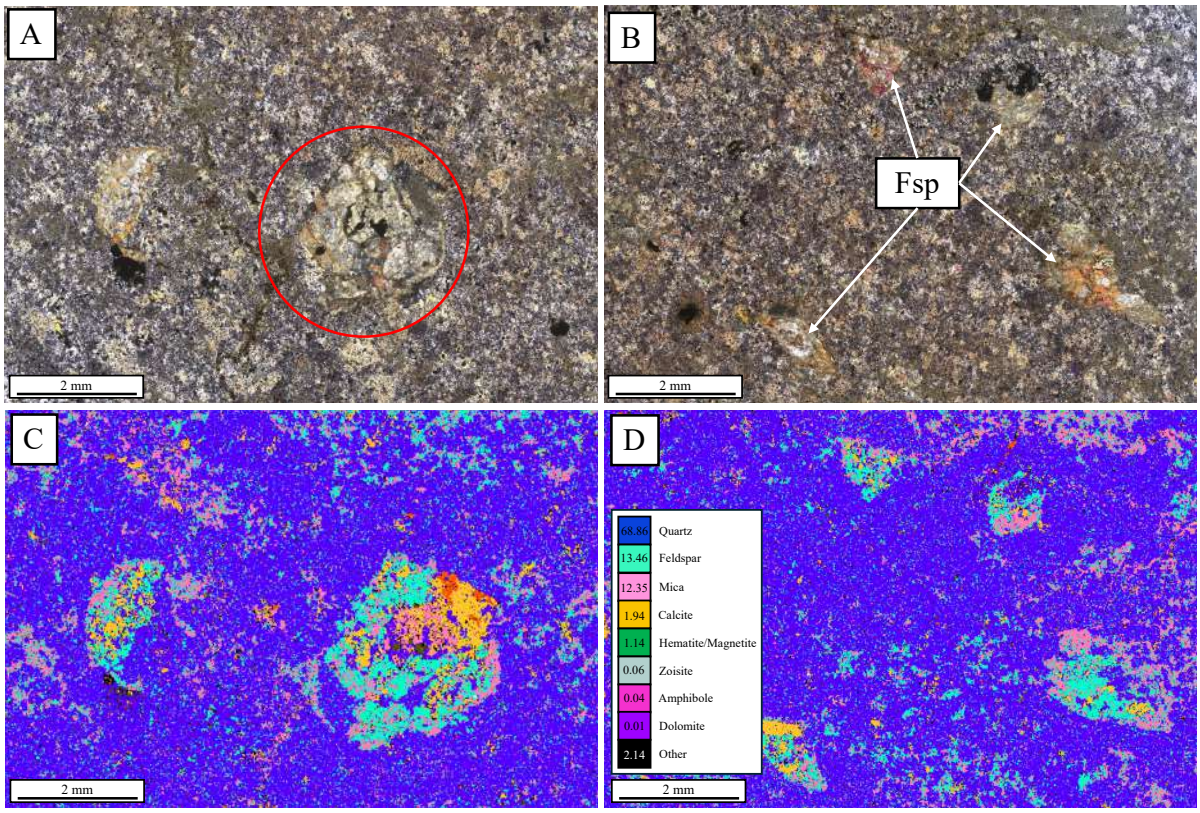


Figure 4.15: A and B – XPL images showing the coarse feldspar phenocrysts embedded in a fine-grained quartz-rich matrix. C and D – TIMA images showing the feldspar phenocrysts morphed with muscovite mica and calcite.

4.2. Compressive strength

After the concrete cubes were made and submerged in water tanks for the appropriate number of days (7, 28 and 56 days), the compressive strength was tested. The cubes were subjected to compressional force and the failure load (kN) was recorded. This failure load was used to calculate the crushing strength (MPa) of each cube. For each testing age and mixture, three measured compressive strengths are averaged and documented in Table 4.1, which also tabulates the saturated surface-dry mass of each cube prior to testing.

Table 4.1: The compressive strength results for each age and mixture. In the instance of a malfunction, the measurement was not accurate and a dash (-) is placed.

		Age (days)								
		7			28			56		
	Mix no.	Mass kg	*FL* kN	Av. c/s MPa	Mass kg	*FL* kN	Av. c/s MPa	Mass kg	*FL* kN	Av. c/s MPa
Dolomite	D4-1	2.44	607.1	60.1	2.38	679.8	68.8	2.38	747.8	74.6
	D4-2	2.43	609.4		2.45	671.4		2.42	747.4	
	D4-3	2.45	587.8		2.44	712.6		2.39	743.4	
	D6-1	2.40	393.0	39.5	2.46	484.8	48.0	2.42	514.8	51.2
	D6-2	2.45	-		2.49	478.6		2.46	511.8	
	D6-3	2.45	396.8		2.43	477.8		2.41	510.8	
Andesite	A4-1	2.49	632.0	62.7	2.49	712.4	73.7	2.50	788.8	77.9
	A4-2	2.50	622.8		2.48	748.8		2.46	788.6	
	A4-3	2.51	-		2.55	750.0		2.50	759.8	
	A6-1	2.50	397.4	40.0	2.50	510.8	50.5	2.49	541.6	55.0
	A6-2	2.55	-		2.50	505.8		2.53	557.2	

	A6-3	2.47	403.0		2.48	498.2		2.50	552.6	
Ferro-quartzite	FQ4-1	2.39	594.4	60.3	2.36	719.8	72.5	2.35	772.2	76.2
	FQ4-2	2.34	577.8		2.31	737.4		2.35	732.4	
	FQ4-3	2.36	638.0		2.37	719.0		2.38	780.8	
	FQ6-1	2.32	287.4	29.7	2.30	389.4	40.3	2.30	413.6	41.9
	FQ6-2	2.36	301.0		2.34	412.2		2.37	417.4	
	FQ6-3	2.36	302.6		2.33	406.6		2.39	424.8	
Quartzite	WQ4-1	2.33	549.4	55.1	2.35	648.8	65.6	2.42	699.4	71.1
	WQ4-2	2.38	558.2		2.45	669.0		2.41	678.4	
	WQ4-3	2.41	546.2		2.40	649.4		2.43	756.4	
	WQ6-1	2.39	366.4	37.9	2.38	475.0	45.6	2.44	528.4	52.9
	WQ6-2	2.40	409.2		2.37	452.8		2.43	547.2	
	WQ6-3	2.37	362.8		2.31	438.8		2.41	511.4	
Felsite	F4-1	2.35	585.4	59.4	2.33	-	69.5	2.33	729.4	72.1
	F4-2	2.37	598.6		2.35	703.0		2.32	693.0	
	F4-3	2.39	598.0		2.35	686.0		2.34	740.8	
	F6-1	2.33	408.0	41.5	2.30	481.8	49.8	2.33	503.8	53.2
	F6-2	2.37	421.0		2.36	498.6		2.34	545.0	
	F6-3	2.30	417.4		2.36	514.8		2.35	548.4	

According to BS 1881-116:1983 (Chapter 2, Section 2.2.5.2), the concrete cubes exhibit satisfactory failure patterns. Most of these cubes demonstrate a failure pattern characterised by the cone-shaped cracking and non-catastrophic splitting (Figure 4.16). However, there were a few samples that experienced explosive failure, in which the cubes crumbled upon being removed from the machine (Figure 4.17). These explosive failures are the result of very high loads in relation to the stiffness of the machine. As the compressional force was applied on the

concrete cube, tension was simultaneously experienced on the support poles of the machine. Near the capacity of the machine, as the high load was being applied and the first crack occurred, the strain in the support poles were transferred onto the cube which led to rapid cracking and explosive failure.



Figure 4.16: The typical failure pattern that most of the concrete cubes followed. Some cubes were not cracked symmetrically, however, the cone shape is present.



Figure 4.17: A concrete cube that experienced explosive failure. Broken fragments of concrete are scattered and the cube crumbled upon being removed from the testing machine, leaving no discernible pattern.

Figures 4.18 and 4.19 presents the graphs of the average compressive strengths of the concrete cubes made with the w/c ratios, 0.4 and 0.6, respectively. At the lower w/c ratio of 0.4, the andesite concrete exhibits the highest compressive strength from ages 0 to 56 days. Ferro-quartzite, dolomite and felsite concrete cubes have similar early strength development between 55 and 61 MPa from ages 0 to 7 days. The ferro-quartzite concrete strength increases the most at day 28 whilst the dolomite and felsite still share a similar strength growth. At day 56, the ferro-quartzite concrete continues to grow stronger than dolomite and felsite, whilst the dolomite grows stronger than the felsite. The quartzite concrete has the lowest compressive strength across all testing ages. However, it has the highest strength growth among the different aggregate concretes, increasing by 16 MPa from day 7 to 56. Between the two quartzites, ferro-quartzite concrete has a notably higher compressive strength compared to that of the quartzite concrete.

When the w/c ratio increases to 0.6, the compressive strength trends shift. The andesite concrete has the highest compressive strengths between days 28 and 56. Felsite concrete has the highest compressive strength between days 0 and 7, surpassing andesite, ferro-quartzite and dolomite, opposed to the trend shown in Figure 4.18. The dolomite concrete maintains a steady and equal strength growth to felsite, resulting in a lower compressive strength than felsite at day 56. The quartzite concrete has a lower compressive strength than both dolomite and felsite at days 7 to 28 but has an equal strength to felsite at day 56. Therefore, quartzite maintains its high strength growth between days 7 to 56, equivalent to the strength growth of andesite concrete at 15 MPa. The ferro-quartzite concrete has the lowest compressive strength across all testing ages at the higher w/c ratio. Out of concern for this unusually low result, a repeat test was conducted which confirmed these results (Figure 4.20).

Considering only the compressive strengths measured at the 28-day curing period as it serves as a benchmark in assessing the structural performance of the concrete (Chapter 2, Section 2.1), the compressive strengths of concrete made with 0.6 w/c ratio follow the same trend as the concretes made with the 0.4 w/c ratio, except for ferro-quartzite. In Figure 4.18 showing the compressive strength for concrete made with a w/c of 0.4, andesite concrete has the highest compressive strength, then ferro-quartzite, felsite, dolomite and quartzite concrete. In Figure 4.19 showing the compressive strength of concrete made with a w/c ratio of 0.6, andesite

concrete maintains its superior compressive strength, achieving the highest value at day 28, then felsite, dolomite, quartzite and ferro-quartzite concrete.

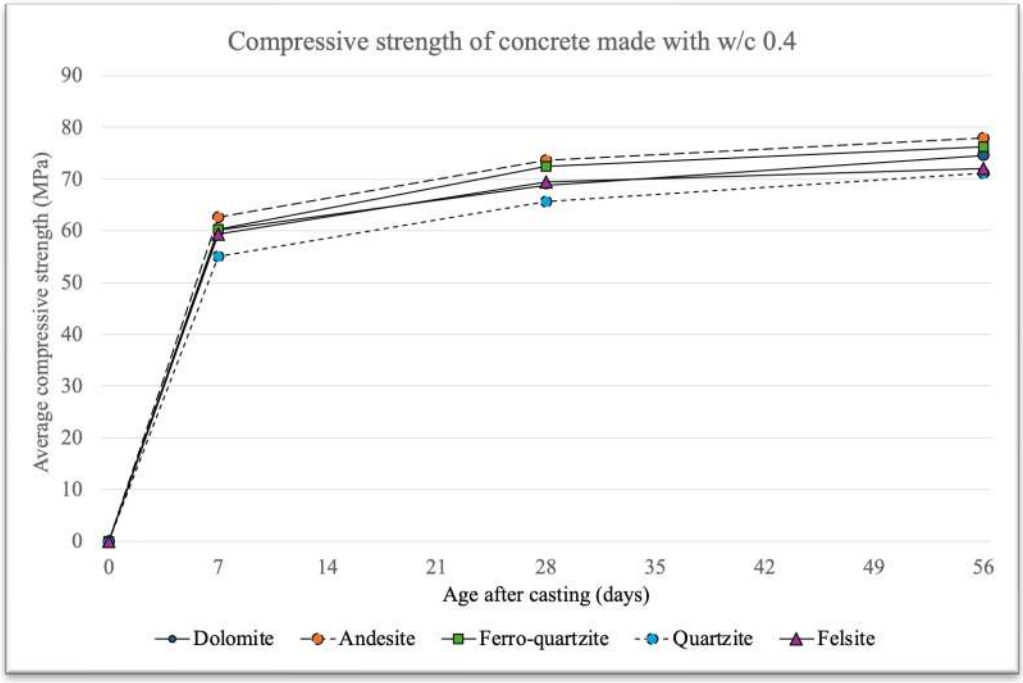


Figure 4.18: The average compressive strengths for the concrete made with the w/c ratio of 0.4.

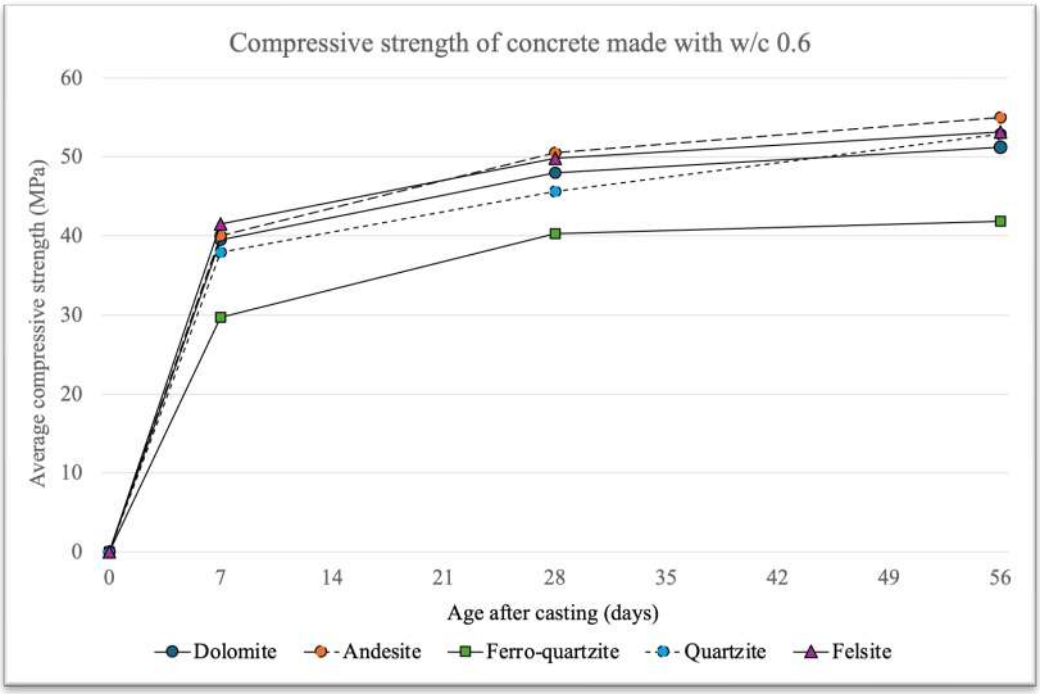


Figure 4.19: The average compressive strengths for the concrete made with the w/c ratio of 0.6.

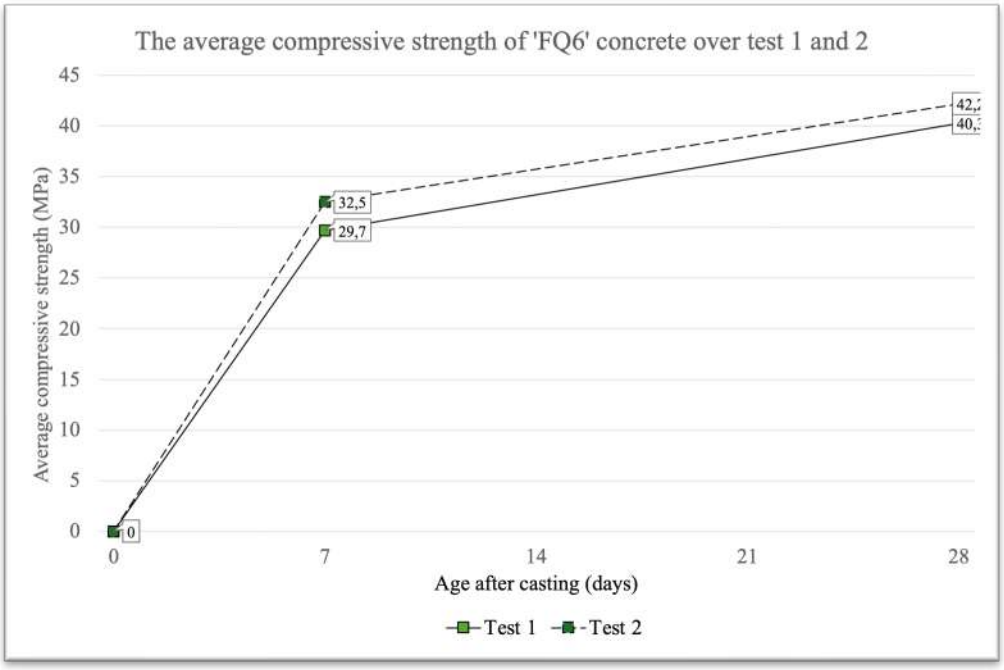


Figure 4.20: The comparison between tests 1 and 2 for compressive strength of ferro-quartzite concrete cubes made with the 0.6 w/c ratio.

4.3. Sessile drop (SD) method

4.3.1. Droplet size determination

To perform the SD method, an appropriate droplet size was required. Using trial and error and the hydrophilicity (hydrophilic or hydrophobic) of the aggregate samples, a droplet size was selected. Hydrophilicity refers to the affinity for water primarily due to their surfaces. The aggregates are composed of clays, micas and/or quartz, which exhibit higher hydrophilic behaviour due to their capacity to form hydrogen bonds with water molecules (Elkhatib et al., 2024). For this reason, a small droplet size was preferred to prevent absorption on the aggregate surfaces. This study used 2 µL droplets. Each liquid reacted differently with the aggregate samples due to their densities and composition. The water and ethylene glycol liquids, with densities of 1.00 g/cm^3 and 1.11 g/cm^3, respectively, produced the typical circular droplet, whereas the diiodomethane liquid with a density of 3.32 g/cm^3 produced an elongated droplet (Figure 4.21). The diiodomethane liquid droplets tend to be attracted to the aggregates, particularly the quartzite and ferro-quartzite, due to their high silica content (quartz >90%). These droplets had a tendency of falling from the needle onto the aggregate surface at micrometre proximities. However, contact angle results do not seem to skew (Table 4.2).

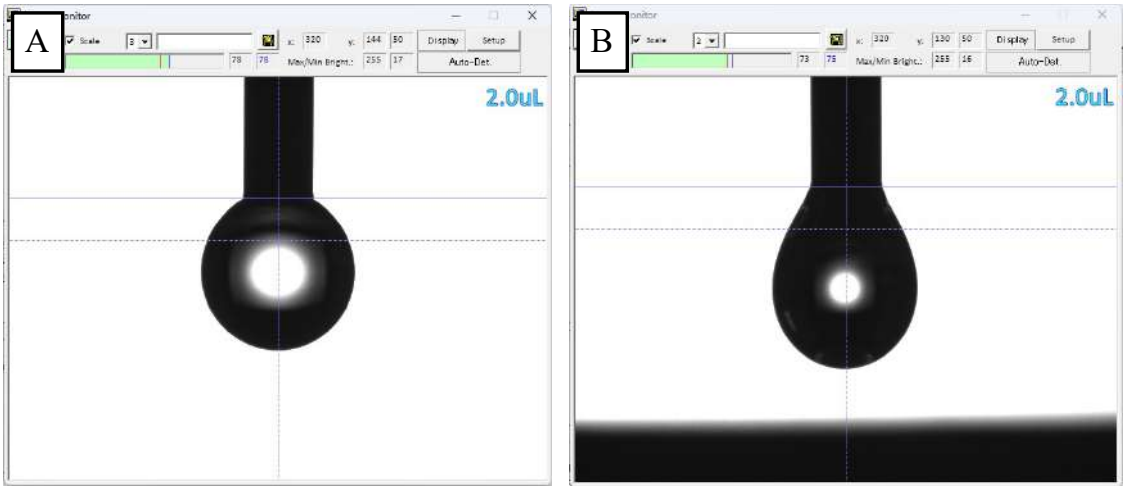


Figure 4.21: A – the droplet size (2 µL) and shape for the water and ethylene glycol probe liquids. B - the droplet size (2 µL) and shape for the diiodomethane probe liquid.

4.3.2. Contact angles and SFE of solid aggregates

The dynamic and static contact angles were measured on each aggregate using the three probe liquids and the SD method. Each aggregate was tested on twice and the average of ten contact angles (*C.A.*) and standard deviations (*S.D.*) were measured. These results are recorded in Table 4.2. The dynamic and static contact angles provide the rate at which the liquid droplets settle on the aggregate surface and the wettability. However, only the static contact angles were used to determine and analyse the SFE of the aggregate samples. The static contact angles provided steadier measurements as compared to the dynamic contact angles, reducing the experimental variability. Therefore, the calculated SFE are better represented by static angles.

The averaged contact angles for each probe liquid were used to determine the average Lifshitz-van der Waals (γ^{SLW}) and Lewis's acid (γ^{S+}) and base (γ^{S-}) components of the solid. These components, together with the Lifshitz-van der Waals (γ^{LLW}), Lewis's acid (γ^{L+}) and base (γ^{L-}) components of the probe liquids, were used to automatically calculate the total SFE of the solid aggregates (γ^{S}) using the Young-Dupré equation. The average dynamic (at 1 second) and static (at 30 seconds) contact angles, their average standard deviations determined by the Contact Angle Meter, as well as the Lifshitz-van der Waals, the Lewis acid and base components and the total SFE of the different solid aggregates are shown in Table 4.2. The manual step-by-step calculation for the total SFE of an aggregate can be found in Appendix B.

*Table 4.2: The average dynamic and static contact angles (**θ**) for each probe liquid and aggregate measured by the contact angle meter, the Lifshitz-van der Waals and Lewis acid and base components, and the total surface free energy for each solid aggregate.*

	Aggregate/Probe liquid		Dolomite	Andesite	Ferro-quartzite	Quartzite	Felsite
Dynamic (1 sec)	Water	**θ** (°)	92.10	96.90	88.85	84.70	78.15
		S.D.	5.50	5.30	4.15	3.10	3.65
	Ethylene glycol	**θ** (°)	74.55	76.10	70.75	69.50	71.50
		S.D.	3.35	2.90	2.95	2.40	2.20
	Diiodomethane	**θ** (°)	60.55	60.10	62.30	59.10	64.00
		S.D.	2.55	3.05	2.65	2.50	2.10
	γ^{SLW}		27.60	27.90	27.25	28.70	25.40
	γ^{S+}		0	0	0	0	0
	γ^{S-}		4.20	2.00	6.15	8.40	15.75
	γ^{S}		**27.60**	**27.90**	**27.25**	**28.70**	**25.40**
Static (30 sec)	Water	**θ** (°)	79.40	94.00	87.60	87.10	86.20
		S.D.	3.20	8.35	5.70	2.80	4.10
	Ethylene glycol	**θ** (°)	65.20	68.60	67.10	66.50	66.20
		S.D.	2.40	1.75	1.70	3.50	2.85
	Diiodomethane	**θ** (°)	60.30	59.70	61.70	57.50	60.60
		S.D.	2.50	2.95	1.05	2.70	3.35
	γ^{SLW}		28.40	28.70	27.60	30.00	28.20
	γ^{S+}		0	0	0	0	0
	γ^{S-}		12.60	2.20	5.80	5.80	6.50
	γ^{S}		**28.40**	**29.60**	**29.10**	**30.00**	**28.20**

Figure 4.22 shows the rate at which water settles on the aggregate surface from 1 to 30 seconds. The contact angles measured with water define the adhesiveness between aggregate and cement, and the formation of the ITZ. Figure 4.23 illustrates the total SFE of the aggregates, which influences their ability to bond with cement and form strong ITZs.

Figure 4.22 shows that dolomite is the most absorbent aggregate. Andesite and ferro-quartzite have low rates of absorption, and quartzite and felsite have similar absorption rates.

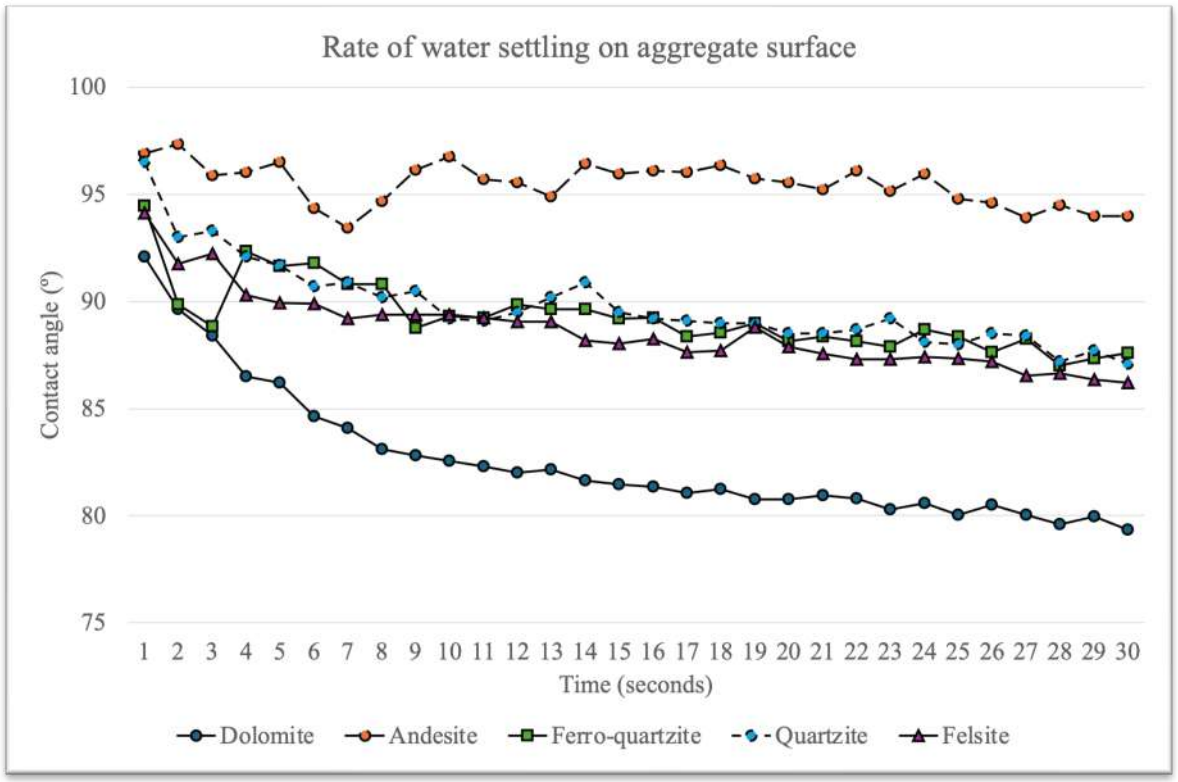


Figure 4.22: The rate at which water settles on the aggregate surface measured between 1 and 30 seconds with the contact angles.

Figure 4.23 shows that quartzite has the highest SFE at 30 mN/m. Andesite and ferro-quartzite exhibit similar SFE of 29.6 mN/m and 29.1 mN/m, respectively. Dolomite and felsite have the lowest SFE, measuring 28.4 mN/m and 28.2 mN/m, respectively. Overall, the SFE values of the aggregates fall within a narrow range of 28 to 30 mN/m, providing a small but consistent dataset for analysis.

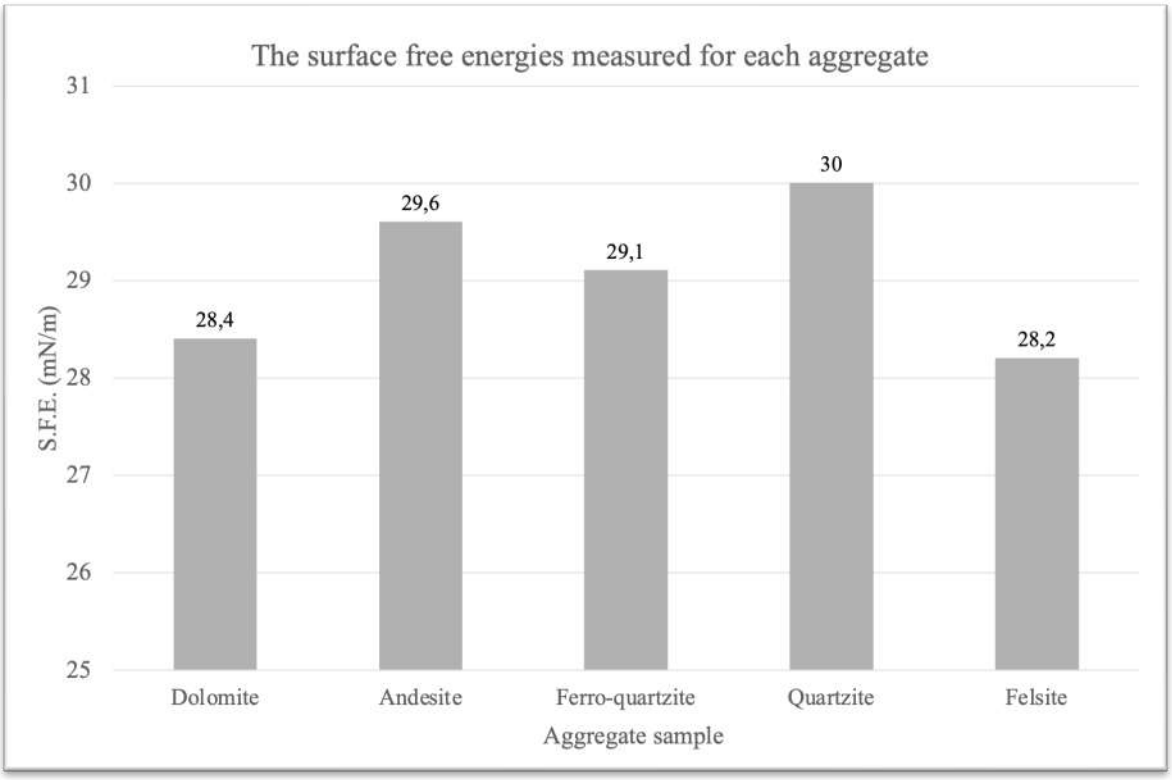


Figure 4.23: The total SFE of the solid aggregates determined using the static contact angles.

4.4. Bond strength test

The components required to calculate the bending strength to break the bond between the aggregate and cement were calculated. Tables 4.3 and 4.4 tabulates these components and the bending strength of the rough (macro-mechanical bond) and smooth (micro-mechanical bond) aggregate prisms, respectively. The manual step-by-step calculations can be found in Appendix C.

The width (*b*) and height (*d*) of the aggregate prism surfaces (Figure 4.24) were measured with a ruler. The prisms were not cut exactly at 40×40, but rather as close as possible. The rough textured surfaces (Figure 4.24B) contain a smooth zone created from the notches that were cut at ~5 mm. However, some of the notches were cut slightly deeper than others. Upon breaking the aggregate prism, the boundary between the smooth and rough textured surface was jagged. Therefore, an approximate average of that boundary was taken as the height of the prism.

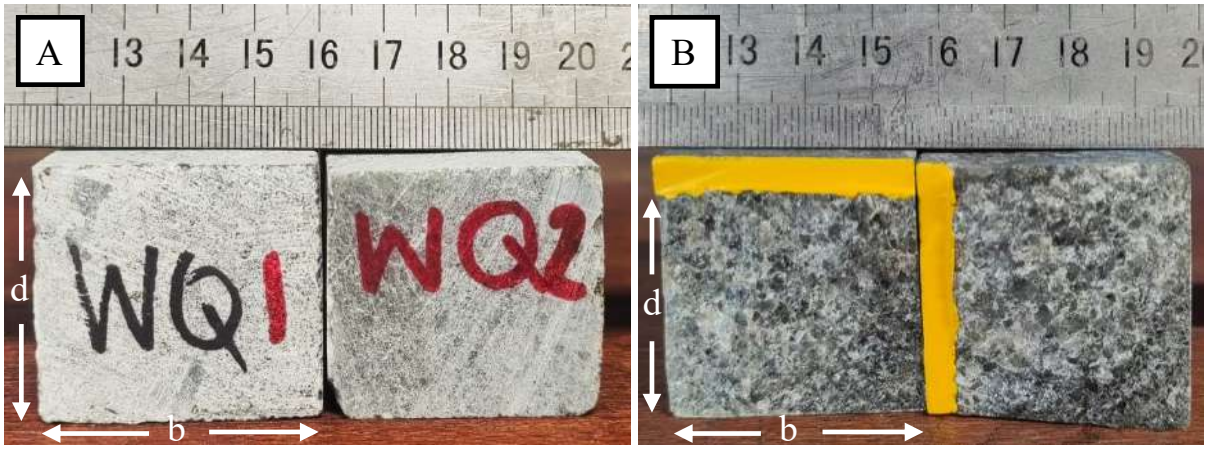


Figure 4.24: A – the dimensions measured for the smooth-textured surfaces. B – the dimensions measured for the rough-textured surfaces taking into account the notch cut to break the aggregate prism (painted in yellow).

Table 4.3: The bending strength (σ) determined using the failure load (m), the applied load (P), the width (b) and height (d) for the rough-surface prisms.

	m (kg)	*P* (N)	*b* (mm)	*d* (mm)	**σ (MPa)**
D1	108	1059.48	43	37	**3.71**
D2	82	804.42	38.5	35	**3.52**
Aa1	127.5	1250.78	37.5	35	**5.62**
Aa2	122	1196.82	38	34	**5.62**
A1	170	1667.70	38	28	**11.55**
A2	166	1628.46	37	27	**12.45**
FQ1	89.5	878.00	38	35	**3.89**
FQ2	108.5	1064.39	38	33	**5.30**
WQ1	127	1245.87	38	34	**5.85**
WQ2	125	1226.25	38	35	**5.43**
F1	80	784.80	36.5	34	**3.84**
F2	145	1422.45	36	35	**6.65**

Table 4.4: The bending strength (σ) determined using the failure load (m), the applied load (P), the width (b) and height (d) of the prism for the smooth-surface prisms.

	m (kg)	*P* (N)	*b* (mm)	*d* (mm)	**σ (MPa)**
D1	55	539.55	37	35	**2.46**
D2	52	510.12	36	34	**2.53**
Aa1	84	824.04	39	38.5	**2.94**
Aa2	81	794.61	39	39	**2.76**
A1	89	873.09	38	38	**3.28**
A2	62	608.22	38	35	**2.69**
FQ1	58	568.98	39	39	**1.98**
FQ2	75	735.75	38.5	38	**2.73**
WQ1	36	353.16	39.5	37	**1.35**
WQ2	50	490.50	39	37	**1.89**
F1	-	-	36	36	**-**
F2	60	588.60	36	36	**2.60**

Figure 4.25 illustrates the graph comparing the mechanical bond (rough textured surfaces), the micro-mechanical bond (smooth textured surfaces) and the macro-mechanical bond (the difference between) for each aggregate prism.

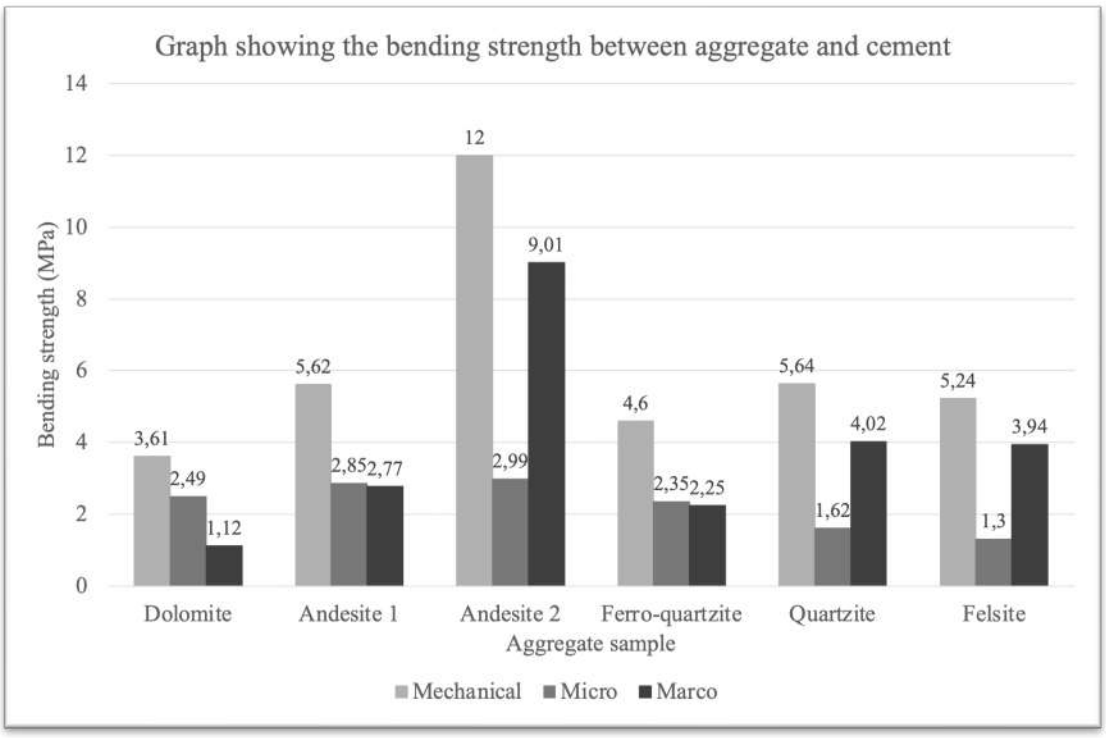


Figure 4.25: The mechanical, micro-mechanical and macro-mechanical bonds between each aggregate and cement.

Andesite 2 (without amygdales) has the highest mechanical bond (12 MPa) consisting of 2.99 MPa micro-mechanical bond and 9.01 MPa macro-mechanical bond. The quartzite and andesite 1 (with amygdales) have similar mechanical bonds of 5.64 MPa and 5.62 MPa, respectively. However, andesite 1 has a stronger micro-mechanical bond (2.77 MPa) than quartzite (1.62 MPa). Therefore, the quartzite has the stronger macro-mechanical bond (4.02 MPa) between the two due to its macroscopic rougher texture. Felsite has the third strongest macro-mechanical bond (3.94 MPa), which is three times stronger than its micro-mechanical bond (1.3 MPa). The macro- and micro-mechanical bonds between ferro-quartzite and cement are similar, 2.35 MPa and 2.25 MPa, respectively. Dolomite has the weakest macro-mechanical bond (1.12 MPa), and most of its bond is reliant on the micro-mechanical bond (2.49 MPa). Dolomite has the weakest bonds overall.

Although the accuracies are reported in Table D, uncertainty was not explicitly propagated to the final calculated values shown in the results. In studies where multiple input variables influence a derived parameter, such as surface free energy, the propagation of measurement error is necessary to assess the reliability of trends, particularly when those trends are weak. While a full statistical propagation was beyond the scope of this study, future work should include this analysis to more rigorously evaluate the significance of observed differences.

Chapter 5: Comparative analysis of results

A comparative analysis of the results recorded in Chapter 4 are discussed in Chapter 5. The following comparisons are made (Figure 5.1):

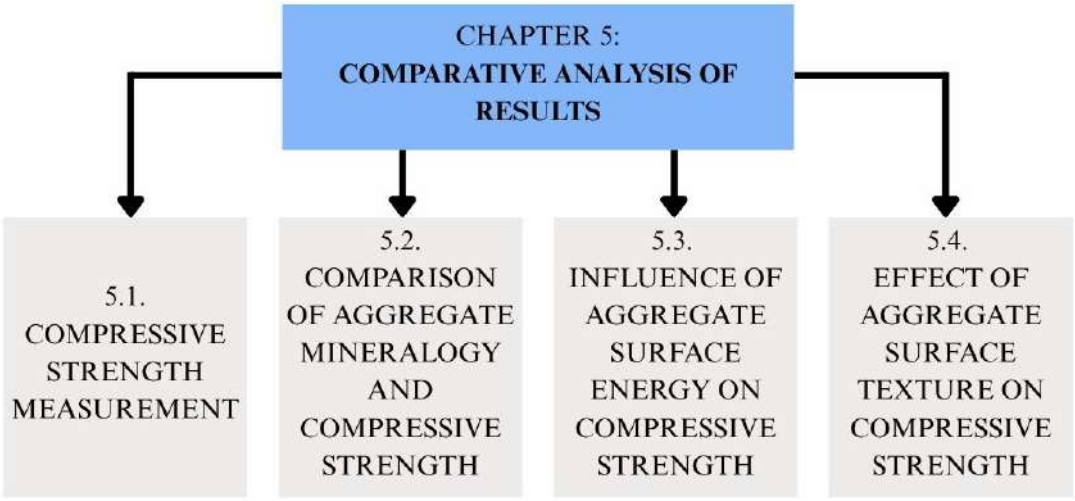


Figure 5.1: A flow diagram showing the structure of Chapter 5.

This study evaluated how different aggregate surface properties influence the compressive strength of concrete. The concrete cubes were tested at three curing durations (7, 28 and 56 days) using two different w/c ratios, 0.4 and 0.6. The results provided insights into the impact of aggregate mineral assemblage, surface energy and surface texture on concrete performance. Five geoscience and civil engineering methods were employed to assess these aggregate properties. This chapter compares the findings of each aggregate property to the compressive strength of concrete measured at 28 days, as well as previous literature. As mentioned in Chapter 2 (Section 2.1), the 28-day curing period serves as a benchmark in assessing the structural performance of concrete or cement, as it captures the critical strength development.

5.1. Compressive strength measurements

The compressive strength of the aggregates measured for this study follow a similar order as reported in the Davis and Alexander (1992) study. Group 1 andesite and felsite produced higher compressive strength, between 516-538 MPa and 377-453 MPa, respectively. Group 3 quartzite and ferro-quartzite produced lower compressive strength, particularly at lower c/w

ratios (or higher w/c ratios), between 105-394 MPa and 106-166 MPa, respectively (Davis and Alexander, 1992).

AfriMat Mining Company, from where the Lyttelton Formation dolomite was collected, recorded in their 'Corporate and Technical Reference Guide' the compressive strength of concrete bricks made with dolomite aggregate. The nominal compressive strength for these various bricks vary between 7 and 14 MPa (AfriMat, 2022). These compressive strengths were measured using concrete cubes and bricks that were made with different w/c ratios (c/w ratios), therefore comparing the values are inconsequential.

5.2. Comparison of aggregate mineralogy and compressive strength

The mineralogy was analysed through petrography and TIMA. The stacked bar graph (Figure 5.2) summarises the mineral assemblages classified during the TIMA analysis for each aggregate sample.

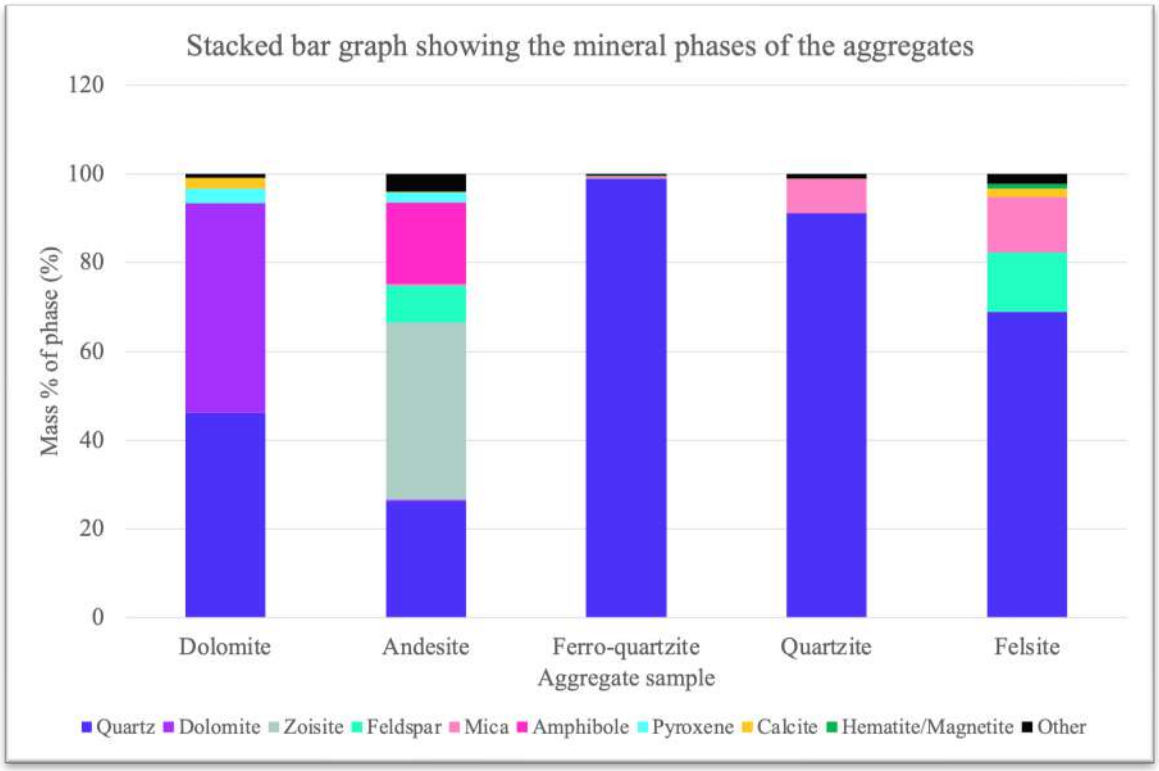


Figure 5.2: A stacked bar graph showing the mass percentage of minerals that each rock aggregate is composed of. "Other" includes minerals that make up less than 0.01%, as well as any other unclassified minerals.

Mica minerals, particularly muscovite, were the only significant detrimental mineral detected in the aggregate samples. According to Alexander and Mindess (2005), micas, such as biotite and muscovite, negatively impact the compressive strength of concrete due to their flaky texture and softness. The graphs (Figures 5.3 and 5.4) display the relationship between mica content present in the aggregate samples and the compressive strength of the concrete at age 28.

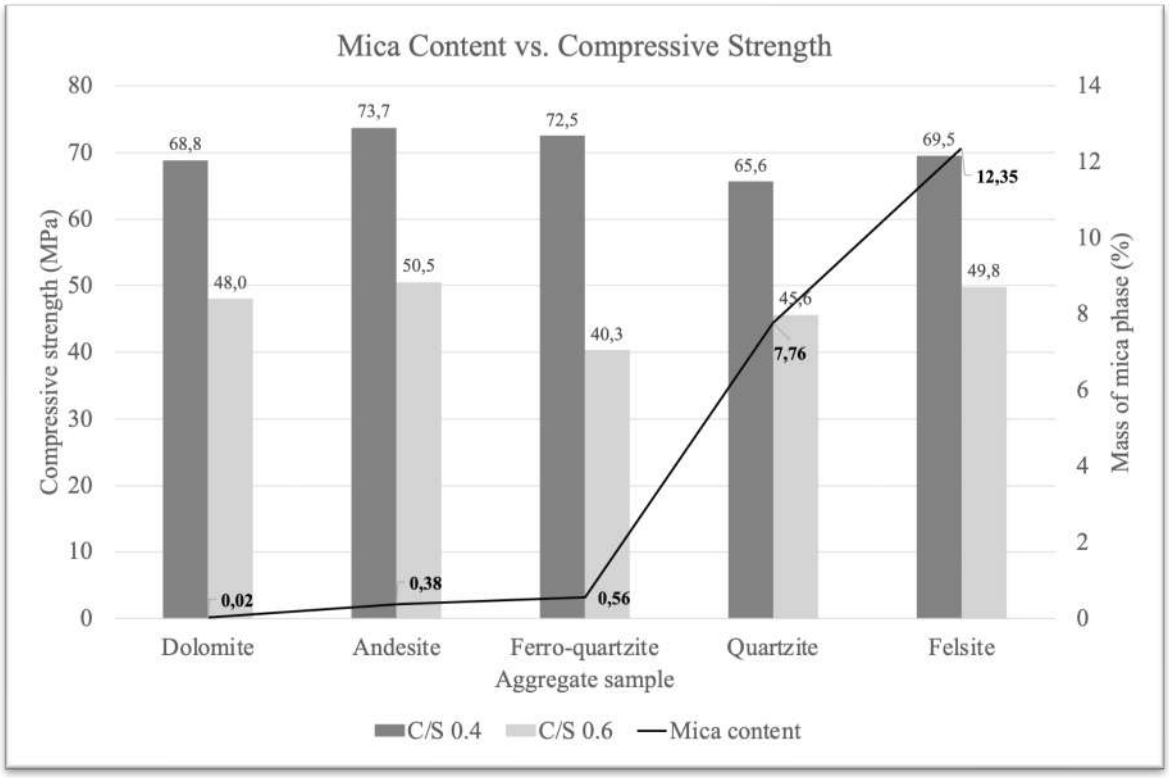


*Figure 5.3: The relationship between the mica content present in the aggregate samples and the compressive strength of the concrete. *C/S 0.4 = compressive strength of concrete cubes made the w/c ratio of 0.4; C/S 0.6 = compressive strength of concrete cubes made the w/c ratio of 0.6.*

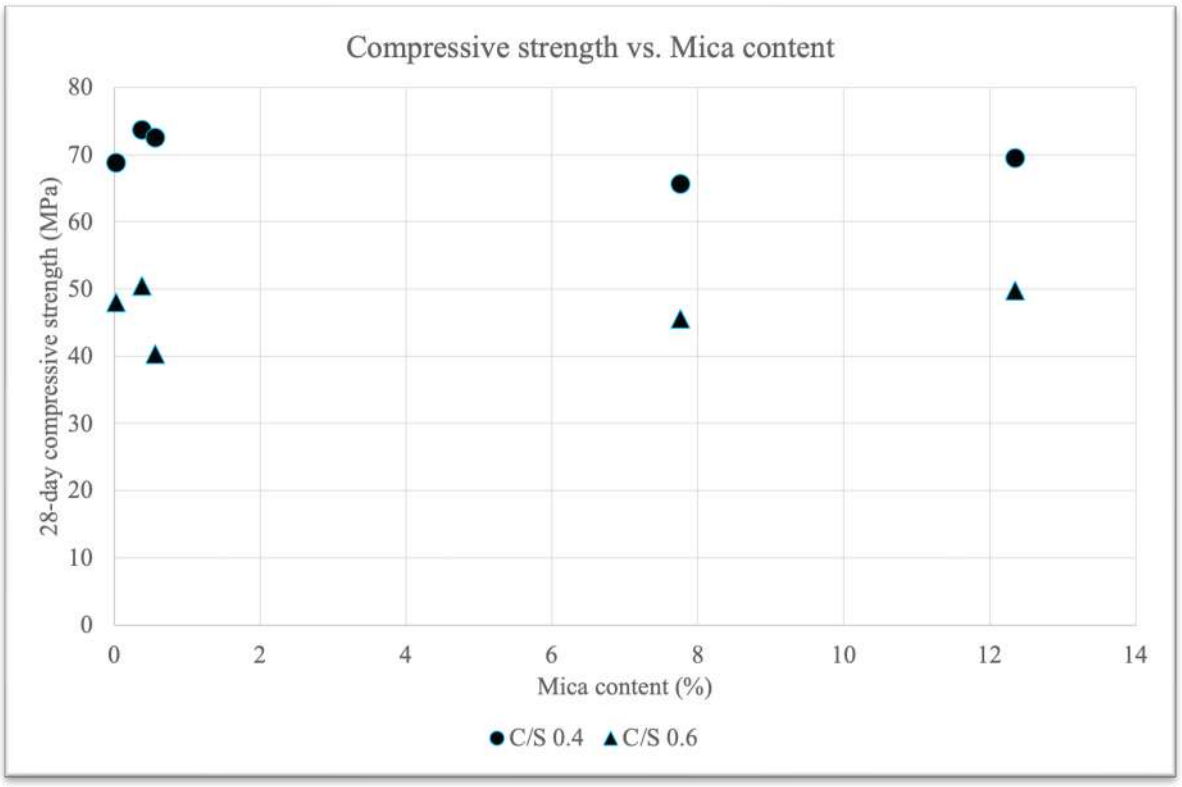


Figure 5.4: Scatter plot showing that compressive strength is dependent on mica content in most aggregate types.

When considering only the compressive strengths of the concrete made with a w/c ratio of 0.4:

- The strength differences are too small to make confident comparisons. However, three aggregates (dolomite, andesite, ferro-quartzite) with the negligible mica content show high compressive strengths.
- The quartzite and ferro-quartzite are both predominantly composed of quartz crystals (>90%). However, the mica content present in the quartzite significantly reduces its compressive strength.
- Felsite has the highest mica content, but does not produce the lowest compressive strength. This is most likely due to the compact texture and high silica composition .
- Felsite produces stronger concrete than dolomite and quartzite despite having a higher mica content.

When considering only the compressive strengths of the concrete made with a w/c ratio of 0.6:

- At a higher w/c ratio, the ferro-quartzite has the lowest compressive strength, despite having little to no mica present in the aggregate. This suggests that the formation of the

ITZ in the presence of more water affects the bond between the ferro-quartzite aggregate and cement paste.

Overall, the mineral assemblages and structural features in the aggregate influences the compressive strength of concrete; and the mica content becomes more influential as w/c ratio is reduced and strength increases.

5.3. Influence of aggregate surface energy on compressive strength

Matsushita and Onoue (2006) stated that the compressive strength of concrete is inversely proportional to the SFE of the aggerates used to produce the concrete; and that the influence of SFE of aggregates in concrete increase at higher w/c ratios. The graphs (Figures 5.5 and 5.6) show how the compressive strength of concrete is influenced by the SFE of the aggregates.

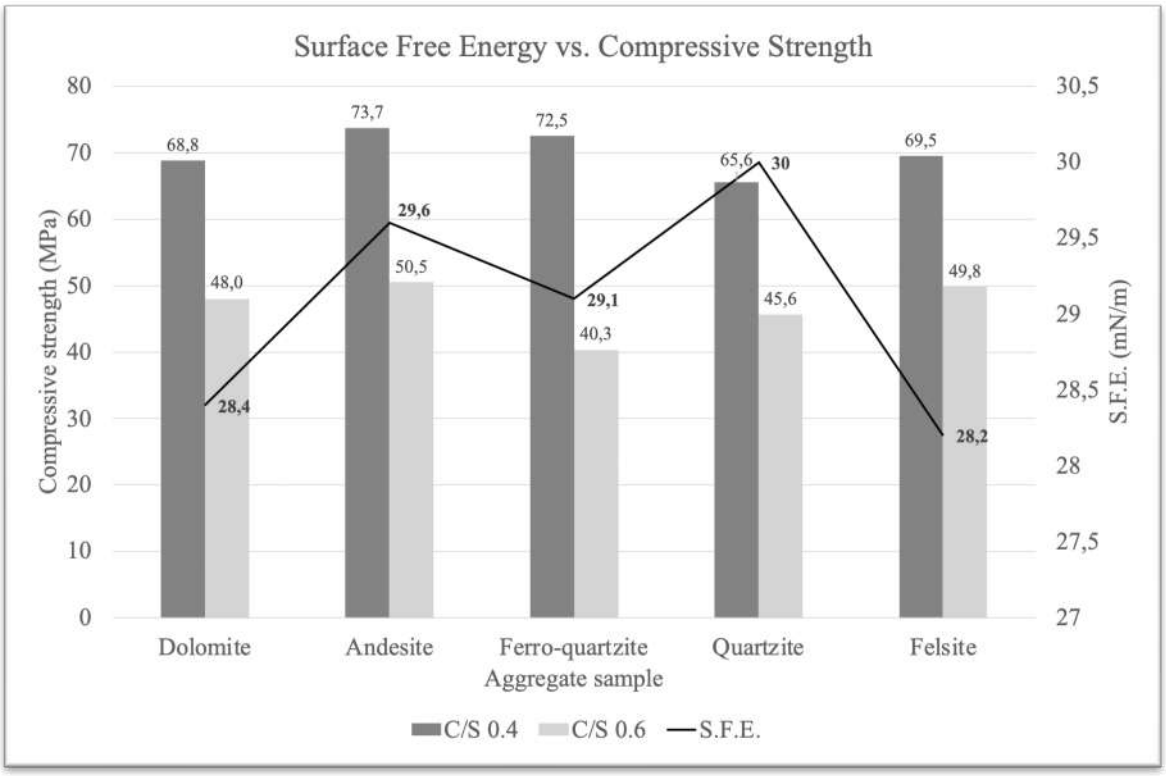


Figure 5.5: The relationship between the SFE of the aggregate samples and the compressive strength of the concrete.

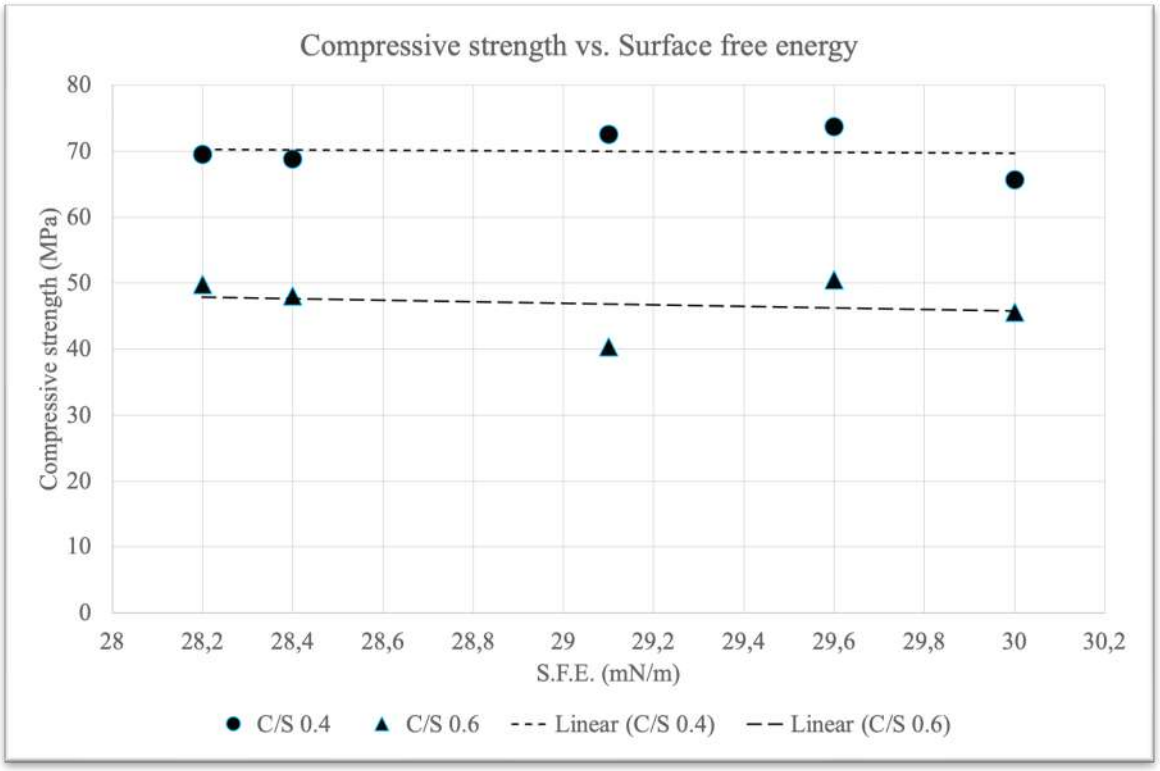


Figure 5.6: Scatter plot showing the incoherent relationship between the compressive strength and the surface free energy.

Felsite and dolomite have the lowest SFE. At age 28, both aggregates have the lower compressive strengths. This could be due to the presence of detrimental minerals and fractures, which prevent the strength of concrete from developing.

When considering only the compressive strength of concrete made with the andesite, ferro-quartzite and quartzite aggregates:

- Andesite does not have the lowest SFE, but its miniscule amount of detrimental minerals and its fine-grained texture contribute to its high compressive strengths.
- Ferro-quartzite has the lowest SFE of the three aggregates and a considerably high compressive strength.
- The quartzite has the highest SFE and the lowest compressive strength (except for the ferro-quartzite concrete made with the 0.6 w/c ratio). This suggests that its compressive strength is negatively impacted by its high mica content and its high SFE.

Therefore, the influence of the SFE of dolomite and felsite aggregates on the compressive strength is obscured by its mineral and structural influences. However, the quartzite and ferro-

quartzite aggregates exhibit the inversely proportional influence of SFE on the compressive strength of concrete.

There is no previous literature to correlate with these results, since this specific probe liquid combination (water–ethylene glycol–diiodomethane) has not been tested on the specific aggregates used in this study (andesite, dolomite, ferro-quartzite, quartzite and felsite). However, surface energy was measured on these aggregates (excluding dolomite) using a water–glycerol–diiodomethane probe combination (glycerol was not an available probe liquid to this study) by scientists at the Indian Institute of Technology–Madras (IIT-Madras). The results are as follows:

Table 5.1: The surface free energy results from the Indian Institute of Technology–Madras.

Aggregate	θ^{o} **(water)**	θ^{o} **(glycerol)**	θ^{o} **(DIM)**	γ^{SLW}	γ^{S+}	γ^{S-}	γ^{AB}	γ^{T}
Andesite	62.0 ± 2.23	96.4 ± 3.51	34.6 ± 3.25	42.2	62.3	11.0	52.3	**94.5**
Ferro-quartzite	70.8 ± 2.00	92.8 ± 2.89	47.6 ± 1.71	35.6	39.4	4.9	27.8	**63.4**
Quartzite	71.6 ± 1.95	75.6 ± 2.12	42.3 ± 0.90	38.4	19.3	0.4	5.6	**44.1**
Felsite	54.8 ± 1.44	86.4 ± 3.32	53.1 ± 1.05	32.5	65.8	4.1	32.8	**65.3**

The results (Table 5.1) show that andesite and quartzite have the highest and lowest SFE, respectively; and felsite and ferro-quartzite have similar surface energies. These results do not correlate with those collected in this study. Although the results itself cannot be correlated, the surface free energy values obtained in this study are considered more reliable than those reported by the IIT–Madras, primarily due to the selection of probe liquids. The water–ethylene glycol–diiodomethane (W–E–D) combination yielded a slightly lower CN of 4.47 than that of the IIT-Madras water–glycerol–diiodomethane (W–G–D) combination, which resulted in a CN of 4.9. Since a lower CN typically indicates reduced error propagation in surface energy calculations and greater numerical stability, the W–E–D combination used in this study offers a more robust basis for analysis. While this small difference suggests improved accuracy, it is acknowledged that a comprehensive comparison should also consider other factors such as measurement repeatability, experimental consistency, and overall procedural accuracy.

5.4. Effect of aggregate surface texture on compressive strength

Ballim (1983) suggested that rougher surface textures create stronger bonds to cement pastes, resulting in stronger ITZs compared to smoother surface textures. As mentioned in Chapter 2 (Section 2.5.4), surface texture is dependent on the surface area of the individual crystals that compose the aggregate. On broken surfaces, fine-grained aggregates expose a larger surface area due to multiple small and irregular fragments, creating a microscopically rougher texture. In contrast, coarse-grained aggregates tend to break along the natural crystal boundaries, creating smoother, more planar surfaces for cement paste to bond with. These broken surfaces favour macro-mechanical bonding when moulded against cement paste.

The aggregate samples used in the bond strength tests were also cut to create intentionally smooth surfaces to reduce the mechanical bond when cement paste was moulded against it. This favours chemical bonding, or rather, micro-mechanical bonding. Figure 5.7 displays the comparison between the compressive strengths and bending strengths of the prims. It should be noted that only the andesite without any silica-rich amygdales is displayed on the graph for the convenience of the analysis.

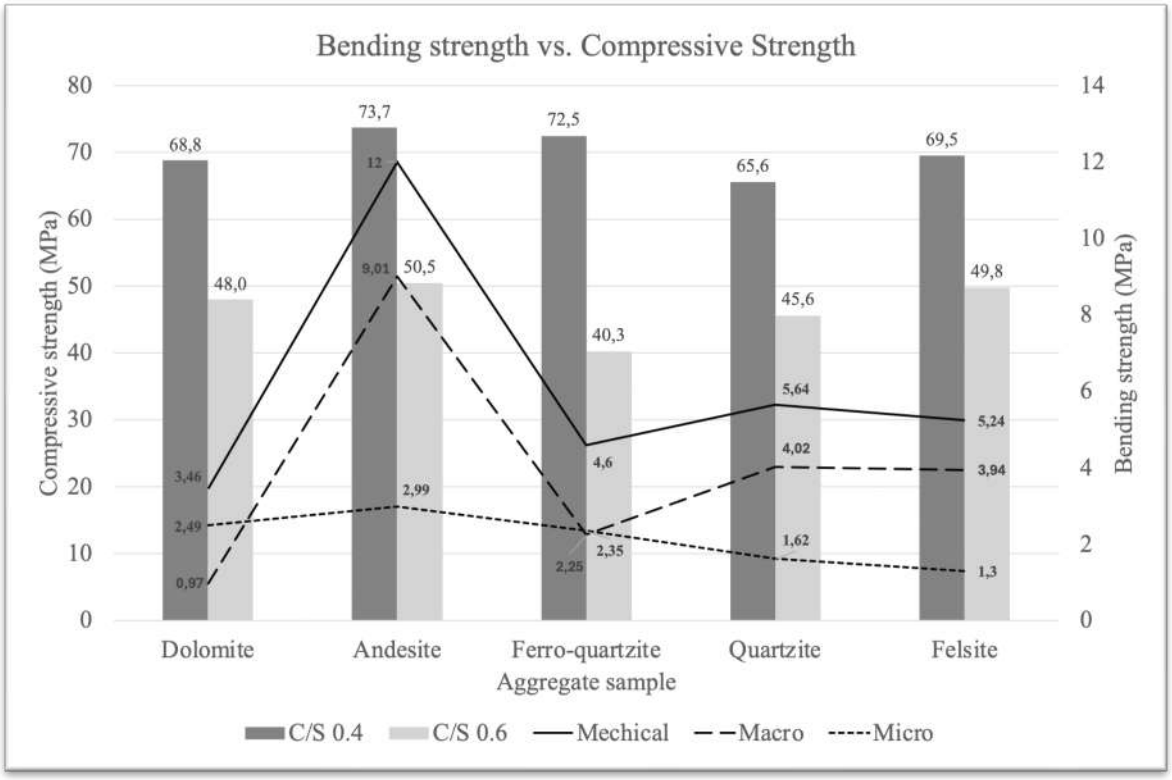


Figure 5.7: The relationship between the compressive strength of concrete and the different bonds that are tested during the bending strength tests.

- Macro-mechanical bond is the dominant bond that holds aggregate and cement phases together in concrete.
- Andesite is fine-grained, therefore has a rough texture. It has the strongest mechanical bond and the highest compressive strength.
- The quartzite has the largest crystals, yet it does not produce the weakest mechanical bond. The large quartz crystals in the mica matrix create a larger surface area, as the crystals are not as tightly packed together. This results in a macroscopic rough texture that enhances bonding with the cement paste. While the mica minerals assist in creating space for the cement to bond, their softness and flakiness prevent further strength development.
- Ferro-quartzite has a low mechanical bond, but a high compressive strength when made with a low w/c ratio. At a higher w/c ratio, the compressive strength is low, which aligns with its low bond strength. Therefore, the compressive strength of ferro-quartzite is more reliant on w/c ratio. An increase in water content affects the formation of the ITZ. This could be a result of the phaneritic texture of ferro-quartzite, providing little bonding space for the cement paste.
- Felsite has a finer-grained texture than the quartzite, yet has a similar mechanical bond and low compressive strength. This could be a result of the high mica content present in the felsite sample, preventing the concrete from developing strength after bonding and curing.
- Dolomite has an extremely weak mechanical bond, which corresponds with the structural features of the aggregate.
- The micro-mechanical bond is less pronounced for all the aggregates, except for dolomite. The dolomite and chert in the dolomite aggregate bond better with the cement paste than the surface of the dolomite itself despite having a fine- to medium-grained texture.

Overall, while the surface texture influences the compressive strength of concrete, it is not solely determined by the grain or crystal size. The mineralogy and the internal structure of the crystals which affect the mechanical bond also play a key role – in addition to intergranular fracture and breakage along grain boundaries, it is also possible that some fracture surfaces, particularly in minerals with pronounced cleavage such as mica, occurred along cleavage planes within individual mineral grains. This may have influenced the resulting surface texture and should be considered a potential contributor to the variability in interfacial bonding behaviour.

Chapter 6: Conclusion

The theory by Duff Abrams in 1918 stimulated the thought that the compressive strength of concrete was solely dependent on the w/c ratio. Ballim (1983) and Alexander and Davis (1992) showed that aggregate type has an influence on the compressive strength of concrete too. It was suggested by Matsushita and Onoue (2006) that the compressive strength is indirectly proportional to the SFE of aggregates; and by Ballim (1983) that the compressive strength is directly proportional to rough surface texture of the aggregates.

Therefore, this study aimed to evaluate the influence of different rock aggregates on the compressive strength of concrete, focusing on the geological and surface characteristics such as surface energy and surface texture. The methods used to investigate these properties included Petrography, TIMA, UCS testing, SFE testing and Bond Strength testing. The investigation included five aggregate types (dolomite, andesite, ferro-quartzite, quartzite and felsite) with different geological origins. Concrete cubes were prepared using these aggregates and two w/c ratios (0.4 and 0.6) to assess the compressive strength development over 7, 28 and 56 days.

Based on previous studies, it was proposed that these aggregate properties would have an effect on the compressive strength of concrete.

The following points summarize the findings of this study:

1. Concrete cubes made with a lower w/c ratio (0.4) result in higher compressive strengths due to reduced porosity and the formation of a stronger ITZ, compared to those made with a higher w/c ratio (0.6). Therefore, an increase in water content significantly lowers the compressive strength of concrete, particularly for ferro-quartzite.
2. The influence of mica content present in the aggregate samples increase as the w/c ratio decreases and compressive strength increases. High mica contents weaken the concrete strength.
3. The SFE plays a role in the concrete performance. However, while low SFE is meant to enhance bonding, it does not always correlate with higher compressive strengths when other properties, such as the presence of detrimental minerals and structural defects, counteract its benefits.

4. The surface texture which is defined by the grain/crystal size in the aggregate, plays a role in the mechanical bond between the aggregate and the cement paste. Finer-grained aggregates, like andesite, create rougher microscopic textures which improve the adhesion between phases and result in higher compressive strengths. Conversely, other fined-grained aggregates, like felsite, do not show as high a compressive strength due to the presence of detrimental minerals, such as mica.
5. Structural features such as fractures and foliation, like in dolomite, have a significant and negative impact on the compressive strength. These features prevent strong mechanical bonds from developing between aggregate and cement. Aggregates with favourable SFE and texture produce weak compressive strengths in concrete when structural defects are present.
6. The combined methods used in this study serve as a fresh perspective into analysing aggregates in concrete, particularly surface energy and surface texture tests that focus on the surface characteristics of aggregates. However, a broader range of aggregates with more than one detrimental mineral may better explain the influence that mineralogy has on concrete compressive strength; an improved understanding of the Contact Angle Meter DMs-401 and probe liquid combinations may eliminate smaller data sets; and a clearer distinction between mechanical and chemical bond would better explain the influence of surface texture on compressive strength.
7. Andesite has the finest grain size, therefore the most rough texture and the highest mechanical bond. It has little to no detrimental minerals and structural defects, and has a moderate SFE. These properties result in the andesite concrete having the highest compressive strength.

Overall, this study concludes that the compressive strength of concrete is not determined by a single aggregate property alone. Rather, it is best described as dependent on a combined influence of mineral characteristics, structural integrity, surface energy and surface texture. Therefore, the hypothesis is supported and the insights gathered regarding aggregate properties are important for aggregate selection in concrete mixture design. Future research could be explored in the microstructural analysis of the ITZ at different w/c ratios.

Recommendations

1. Exploring the microstructural analysis of the interfacial transition zone at different water-to-cement ratios.
2. The study of the relationship between ferro-quartzite aggregate and water in concrete.
3. The influence of different probe liquid combinations on the surface free energy of solid rock surfaces.
4. An investigation on how polished aggregates influence compressive strength of concrete.
5. Investigating the influence of surface texture and grain size on concrete strength using mineralogically similar intrusive and extrusive rocks.

References

- Addis, B. and Goodman, J. (2009) 'Concrete mix design', in Owens, G. (ed.) *Fulton's concrete technology.* Midrand, South Africa: Cement and Concrete Institute, pp. 219-225.
- AfriMat (2022) *Corporate and Technical Reference Guide.* South Africa: AfriMat. Available at: https://www.afrimat.co.za/wp-content/uploads/2022/08/Afrimat-Corporate-and-Technical-Reference-Guide-2022-v2.pdf (Accessed: 8 March 2025).
- Akbaş, E.N. (2012) *Bulk Density (Unit Weight) and Voids in Aggregate (ASTM C29)*. Unpublished report. Eastern Mediterranean University. Available at: https://staff.emu.edu.tr/ozgureren/en/Documents/CIVL284/CIVL284%20SAMPLE%20LAB%20REPORT.pdf (Accessed: 17 April 2024).
- Alex Strekeisen. (2020) *Andesite*. Available at: https://www.alexstrekeisen.it/english/vulc/andesite.php (Accessed: 8 April 2024).
- Alexander, M.G. (1994) *Effects of aging on mechanical properties of the interfacial zone between cement paste and rock*. 7th edn. USA: Elsevier Science Ltd, pp.1277–1285.
- Alexander, M.G. and Ballim, Y. (2011) *The concrete-making properties of andesite aggregates*, Sabinet Gateway, pp. 49–57.
- Alexander, M.G. and Mindess, S. (2005) *Aggregates in Concrete.* Milton Park, Abingdon: Taylor and Francis.
- Aligizaki, K.K., de Rooij, M.R. and Macdonald, D.D. (2000) '*Analysis of iron oxides accumulating at the interface between aggregates and cement paste'*, Cement and Concrete Research, 30(12), pp. 1941–1945. doi:10.1016/s0008-8846(00)00392-6.
- Altermann, W. and Lenhardt, N. (2012) 'The volcano-sedimentary succession of the Archean sodium group, Ventersdorp Supergroup, South Africa: Volcanology, Sedimentology and geochemistry', *Precambrian Research*, 214–215, pp. 60–81. doi:10.1016/j.precamres.2012.02.012.
- Anton Paar GmbH (2025) *Gas Pycnometer for Semi-Solid and Solid Density: Ultrapyc.* Available at: https://www.anton-paar.com/corp-en/products/details/ultrapyc/?utm_source=google&utm_medium=cpc&utm_campaign=HQ_FoodIndustry.Chocolate_EN&utm_content=C-00072004&gad_source=1&gbraid=0AAAAAD-OFHMcvS2cnr7dOzHA0xT06EL3A&gclid=Cj0KCQiAlbW-

BhCMARIsADnwasrXb6Ysbcor0KyzGabPCwi7Jx2qrtksPugHM2qcdY2kRXfGcLanfIAaAtMIEALw_wcB (Accessed: 4 February 2025).

- ASTM International (2020) *Standard Specification for Chemical Admixtures for Concrete*. Available at: https://www.astm.org/c0494_c0494m-17.html# (Accessed: 18 September 2024).
- Ballim, Y. (1983) The concrete making properties of the andesite lavas from the Langgeleven Formation of the Ventersdorp Supergroup. M.Sc. dissertation. University of the Witwatersrand, Johannesburg.
- Bhardwaj, B.B. and Singh, S. (2023) 'Evaluation of the failure planes in concrete containing reclaimed asphalt pavement (RAP) aggregates', *Cement and concrete composites*, 145 (2024), pp.1-16. doi:https://doi.org/10.1016/j.cemconcomp.2023.105334.
- Blue Pearl Stone. (2016) *Quartz Vs. Quartzite*. Available at: https://www.bluepearlstone.com/blog/quartz-versus-quartzite (Accessed: 5 March 2024).
- Bowen, T.B., Marsh, J.S., Bowen, M.P. and Eales, H.V. (1986) 'Volcanic rocks of the Witwatersrand Triad, South Africa. I: Description, classification and geochemical stratigraphy', *Precambrian Research*, 31(4), pp. 297–324. Available at: https://doi.org/10.1016/0301-9268(86)90038-0 (Accessed: 21 April 2024)
- Burke, K. (1986) *Archean foreland basin tectonics in the Witwatersrand, South Africa*. M. Sc. dissertation. NASA STI Facility.
- Chen, Q., Zhang, J., Wang, Z., Zhao, T., Wang, Z. (2024) 'A review of the interfacial transition zones in concrete: Identification, physical characteristics, and mechanical properties', *Engineering Fracture Mechanics*, 300 (4). doi:10.1016/j.engfracmech.2024.109979.
- Concrete Exchange. (2023) *How To Perform a Concrete Slump Test*. Available at: https://www.concreteexchange.com/how-to-center/concrete-mixes-and-additives/concrete-slump-test/ (Accessed: 10 February 2025).
- Davis, D.E. and Alexander, M.G. (1992a) *Properties of aggregates in concrete (Part 1)*. Johannesburg, South Africa: Hippo Quarries Technical.
- Davis, D.E. and Alexander, M.G. (1992b) *Properties of aggregates in concrete (Part 2)*. Johannesburg, South Africa: Hippo Quarries Technical.
- De La, H. and Winter, R. (1976) 'A lithostratigraphic classification of the Ventersdorp succession', *Sabinet African Journals*, 79(1), pp. 31–48. Available at: https://journals.co.za/doi/epdf/10.10520/AJA10120750_2917 (Accessed: 20 April 2024).

- Dooner, S. (2019). *Testing Concrete Mixing Water Quality*. Available at: https://watertreatmentservices.co.uk/concrete-mixing-water-testing/ (Accessed: 9 Mar. 2025).
- Du Plessis, G.P. (2008) *The relationship between geological structures and dolerite intrusions in the Witbank Highveld Coalfield, South Africa*. M. Sc. dissertation. University of the Free State.
- Earle, S. (2015) '5.3 the products of weathering and erosion', in *Physical Geology*. Gabriola Island, British Columbia: Creative Commons Attribution. Available at: https://opentextbc.ca/geology/chapter/5-3-the-products-of-weathering-and-erosion/ (Accessed: 15 April 2024).
- Elkhatib, O., Tetteh, J., Ali, R., Mohamed, A. I., Bai, S., Kubelka, J., Piri, M., and Goual, L. (2024). 'Wettability of rock minerals and the underlying surface forces: A review of the implications for oil recovery and geological storage of CO2', *Advances in Colloid and Interface Science*, 333, pp. 103283. doi: 10.1016/j.cis.2024.103283.
- Eriksson, P.G., Schreiber, U.M. and van der Neut, M. (1991) 'A review of the sedimentology of the early Proterozoic Pretoria Group, Transvaal Sequence, South Africa: Implications for tectonic setting', *Journal of African Earth Sciences*, 13(1), pp. 107–119. doi:10.1016/0899-5362(91)90046-2.
- Ferreira, S.R., de Andrade, R.G.M., de Andrade, G.M., de Araújo, O.M., Lopes, R.T., Fairbairn, E., Grabois, T.M. and Ukrainczyk, N. (2022) 'Bond behavior of a bio-aggregate embedded in cement-based matrix', *Materials (Basel)*, 15(17), p. 6151. doi:10.3390/ma15176151.
- Fuchs, S.H.J., Schumann, D., Williams-Jones, A.E., Murray, A.J., Couillard, M., Lagarec, K., Phaneuf, M.W. and Vali, H. (2017) 'Gold and uranium concentration by interaction of immiscible fluids (hydrothermal and hydrocarbon) in the Carbon Leader Reef, Witwatersrand Supergroup, South Africa', *Precambrian Research*, 293(1), pp. 39–55. doi:https://doi.org/10.1016/j.precamres.2017.03.007.
- Ghadafi, A.M. and Kankam, C.K. (2022) 'Toughness and Ductility Characteristics of Reinforced Concrete Beams Containing Recycled Polyethylene Fibres', *Jornal of materials Science research and Reviews*, 9(4), pp. 36–49.
- Gibbs, R. (2023) *Failure and Mohr's Circle, GEOL4030A: Structural Geology and Mineralisation Processes IV*. University of the Witwatersrand.

- Gordon, J.E. (1978) *Structures or Why things don't fall down*. 2nd edn. London: Da Capo Group, pp. 25, 220-221.
- Grieve, G. (2009) 'Aggregates for concrete', in Owens, G. (ed.) *Fulton's Concrete Technology*. 9th edn. Midrand, South Africa: Cement and Concrete Institute, pp. 25–54.
- Gu, X., Jin, X. and Zhou, Y. (2016) *Basic Principles of Concrete Structures*. Shanghai, China: Tongji University Press.
- Gusain, I., Sharma, S., Debarma, S., Sharma, A.K., Mishra, N., Dahale, P.P. (2023) 'Study of concrete mix by adding dolomite in conventional concrete as partial replacement with cement', *Materials Today: Proceedings*, 73(1), pp. 163-166. doi: 10.1016/j.matpr. 2022.09.583.
- Haist, M., Divoux, T., Krakowiak, K. J., Skibsted, J., Pellenq, R. J., Müller, H. S. and Ulm, F. (2021) 'Creep in reactive colloidal gels: a nanomechanical study of cement hydrates', *Physical Review Research*, 3(4). doi:10.1103/physrevresearch.3.043127.
- Harvey, D. (2000). *Modern Analytical Chemistry*. Boston: McGraw-Hill.
- Hein, G. (2014) *Lyttelton Dolomite*. Available at: https://www.geocaching.com/geocache/GC59FB7 (Accessed: 7 April 2024).
- Holmén, K. (2000) 'The global carbon cycle', *International Geophysics*, pp. 282–321. doi:10.1016/s0074-6142(00)80117-5.
- Hrstka, T., Gottlieb, P., Skala, R., Breiter, K. and Motl, D. (2018) 'Automated Mineralogy and Petrology - Applications of TESCAN Integrated Mineral Analyzer (TIMA)', *Journal of Geosciences,* 63(1) pp. 47–63. Available at: https://doi.org/10.3190/jgeosci.250 (Accessed: 12 May 2024).
- Htonl. (2008) *File: Map of Gauteng with municipalities labelled (2006).svg*. Available at: https://commons.wikimedia.org/wiki/File:Map_of_Gauteng_with_municipalities_labelled_%282006%29.svg#file (Accessed: 08 April 2024).
- Huang, Y., Hu, X., Shi, C., and Wu, Z. (2023) 'Review on the Formation and Improvement of Interfacial Transition Zone Between Cement Paste and Aggregate in Concrete', *Materials Reports*, 37(1). Available at: https://doi.org/10.11896/cldb.21050009 (Accessed 30 Jul. 2025).
- Hutchison, C.S. (2005) 'Semporna Peninsula volcanism', *Geology of North-West Borneo*, pp. 325–339. doi:10.1016/b978-044451998-6/50026-0.

- John, E. and Lothenbach, B. (2023) 'Cement hydration mechanisms through time – a review', *Journal of Materials Science*, 58(24), pp. 9805–9833. doi:10.1007/s10853-023-08651-9.
- Jones, M.Q.W. (2003) 'Thermal properties of stratified rocks from Witwatersrand gold mining areas', *The Journal of The South African Institute of Mining and Metallurgy*, pp.173–186.
- Joubert, P. and Johnson, M.R. (1998) *Abridged lexicon of South African stratigraphy*. Pretoria: South African Committee for Stratigraphy.
- Koc, M. and Bulut, R. (2012) 'Surface free energy components of aggregates from contact angle measurements using Sessile Drop method', in Miura et al. (eds) *Advances in Transportation Geotechnics II*. London: Taylor and Francis Group, pp. 560-565.
- Kumar, M. (2020). *Hooke's Law*. Available at: https://byjus.com/physics/hookes-law-equation-experiment/ (Accessed: 24 Oct. 2024).
- Kyowa. (2008) *DMs-401, Basic contact angle meter*. Available at: https://www.face-kyowa.co.jp/english/en_products/en_contact_angle/detail_01_2_2.html (Accessed: 25 March 2024).
- Law, J.D.M., Bailey, A.B., Cadle, A.B., Phillips, G.N., Stanistreet, I.G. (1990) 'Reconstructive approach to the classification of Witwatersrand 'quartzites', *South African Journal for Geology*, 93(1), pp. 83–92. Available at: https://journals.co.za/doi/pdf/10.10520/AJA10120750_799 (Accessed: 8 April 2024).
- Liang, Z. (2024) *How to Calculate Bending Moment Diagrams?* Available at: https://skyciv.com/docs/tutorials/beam-tutorials/how-to-draw-bending-moment-diagrams/ (Accessed: 24 October 2024).
- Martin, J.W. (2006) 'Glasses and ceramics', *Materials for Engineering*, pp. 133–158. doi:10.1533/9781845691608.2.133.
- Matsushita, H. and Onoue, K. (2006) 'Influence of surface energy on compressive strength of concrete under static and dynamic loading', *Journal of Advanced Concrete Technology*, 4(3), pp. 409–421. doi:10.3151/jact.4.409.
- Mishra, G. (2014). *Compressive Strength of Concrete-Cube Test, Procedure, Results*. Available at: https://theconstructor.org/concrete/compressive-strength-concrete-cube-test/1561/ (Accessed: 15 October 2024).
- Mishra, V., Singh, D. and Habal, A. (2020) 'Investigating the condition number approach to select probe liquids for evaluating surface free energy of bitumen', *International Journal*

of Pavement Research Technology, 13(1), pp. 10–19. Available at: https://doi.org/10.1007/s42947-019-0097-x (Accessed: 3 March 2025)

- Neto, J., de al Torre, A.G. and Kirchheim, A.P. (2021) 'Effects of sulphates on the hydration of Portland Cement - A review', *Elsevier Science Inc.*, 12(1). Available at: https://doi.org/10.1016/j.conbuildmat.2021.122428 (Accessed: 5 September 2024).
- Neville, A.M. (2011). *Properties of Concrete*. 5th ed. England: Pearson Education Limited.
- Neville, A.M. and Brooks, J.J. (1987) *Concrete Technology*. 2nd edn. Essex, England: Pearson Education Limited, pp. 134.
- Ollivier, J.P., Maso, J.C. and Bourdette, B. (1995) 'Interfacial Transition Zone in Concrete', *Elsevier Science Inc*., 2(1), pp. 30-38.
- Owens, G. (ed.) (2009) '*Fulton's concrete technology'*. Midrand, South Africa. Cement and Concrete Institute.
- Paprika, D.E., Agangi, A., Hofmann, A., Ringdahl, P., Hartmann, S. and Déri-Takács, J. (2024) 'New details on the volcanic and tectonic evolution of the Mesoarchaean Dominion Group with special reference to the Syferfontein Formation in the Ottosdal Area (South Africa)', *South African Journal of Geology*, 127(2), pp. 219–238. doi:10.25131/sajg.127.0003.
- Pedreros, L., Cárdenas, F., Ramírez, N. and Forero, E. (2020). 'NDT Non-Destructive Test for Quality Evaluation of Concrete specimens by Ultrasonic Pulse Velocity measurement', *IOP Conference Series: Materials Science and Engineering*, 844(1). doi:https://doi.org/10.1088/1757-899x/844/1/012041.
- Phillips, N., Vearncombe, J., Craw, D. and Day, A. (2024) 'The temporal distribution of the host rocks to gold, the Archean Witwatersrand Basin, South Africa', *Minerals*, 14(2), p. 199. doi:10.3390/min14020199.
- Premakumara, A.K. (2020). *Ensuring The Quality of Concrete - Cube Testing*. Available at: https://akpremakumara.wixsite.com/civilengexplorer/post/ensuring-the-quality-of-concrete-cube-testing (Accessed: 21 Aug. 2024).
- Ramé-hart instrument co. (2024) *Contact Angle Goniometer / Tensiometer Technical Information*. Available at: https://www.ramehart.com/technical.htm (Accessed: 6 September 2024.)
- Rammela, T. (2022) *Geology of the Malmani Subgroup in the Vaal area south of Johannesburg: Implications for the future development of the Glen Douglas Dolomite Mine*. M. Sc. dissertation. University of Johannesburg.

- Rossen, J.E. (2014) *Composition and morphology of C-A-S-H in pastes of alite and cement blended with supplementary cementitious materials.* M. Sc. Thesis. Materials Science and Engineering Federal Polytechnic School of Lausanne.
- Roxburgh, J. (2021) 'Water quality in the concrete mix', *Sabinet African Journals*, 46(5). Available at: https://hdl.handle.net/10520/ejc-imiesa_v46_n5_a4 (Accessed: 6 December 2024).
- Rudolph Research Analytical. (2025). *Density Meter*. Available at: https://rudolphresearch.com/density-meter/ (Accessed: 10 February 2025).
- Sahu, A., Dey, T. and Chakraborty, S. (2016) 'Study on the Interfacial Transition Zones of Recycled Aggregate Concrete', *Indian Journal of Science and Technology*, 9(47), pp. 1-6. doi: 10.17485/ijst/2016/v9i47/106263.
- Science Ready. (2019). *What is Gravimetric Analysis?* Available at: https://scienceready.com.au/pages/gravimetric-analysis?srsltid=AfmBOooUvZVDugKjYdblnf-bWMpU9O4SXfHuogsuv5gjdUqJ8Sgds6Pa (Accessed: 10 February 2025).
- Sika South African (Pty) Ltd. (2020). *Product Data Sheet, Sika® ViscoCrete®-3088+*. South Africa: Sika South Africa (Pty) Ltd. Available at: https://zaf.sika.com/dam/dms/za01/s/sika_viscocrete_-3088.pdf (Accessed 9 August 2024).
- Stamsnijder, J. (2017) *New geochronological constraints on the Klipriviersberg Group: defining a new Neoarchean large igneous province on the Kaapvaal Craton, South Africa.* dissertation. Department of Geology, Lund University.
- Twagira, M.E. and Jenkins, K.J. (2009). 'Moisture damage on bituminous stabilized materials using a MIST device', in *Advanced Testing and Characterization of Bituminous Materials*. London: Taylor and Francis Group.
- Vaia. (2019). *Mechanical Oscillations.* Available at: https://www.vaia.com/en-us/explanations/engineering/mechanical-engineering/mechanical-oscillations/ (Accessed: 10 February 2025).
- Vu, X.H., Malecot, Y., Daudeville, L. and Buzaud, E. (2009) 'Effect of the water/cement ratio on concrete behavior under extreme loading', *International Journal for Numerical and Analytical Methods in Geomechanics*, 33(17), pp. 1867–1888. doi:10.1002/nag.796.

- Wei, J. and Zhang, Y. (2012) 'Applications of Sessile Drop Method to Determine Surface Free Energy of Asphalt and Aggregate', *Journal of Testing and Evaluation,* 40(5), pp. 1-7. Available at: https://doi.org/10.1520/jte20120060 (Accessed: 16 August 2024).
- Wittmann, F. H., Sun, Z. and Zhao, T. (2010) 'Surface energy and fracture energy', in Oh, B.H. et al. (eds.) *Fracture Mechanics of Concrete and Concrete Structures - Recent Advances in Fracture Mechanics of Concrete*. Seoul: Korea Concrete Institute, pp. 13-20.

Appendix A: Contact angle meter DMs-401 guide

The following guide is meant to assist those interested in using the Contact Angle Meter DMs-401 instrument, housed at the School of Geosciences, University of the Witwatersrand. This is a detailed, step-by-step instruction sheet created by the author of this research paper. It includes images and important keywords that would assist any beginner using the instrument for the first time.

List of abbreviations used in the guide:

C.A.: contact angle

FAMAS: interFAce Measurement and Analysis System software

SFE: surface free energy

SUS: stainless steel

USB: universal serial bus

Ver.: version

Turn on the power



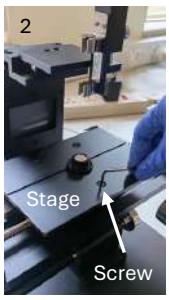
Turn the power on by flipping the switch upward. The light source will illuminate. Be sure to always wear lab gloves when handling the instrument and any apparatus.

Horizontal adjustment

1. Place the level on the base and turn the four horizontal adjustment legs until the bubble is centered.
2. Place the level on the stage and use the hexagon wrench to adjust the three horizontal screws until the bubble is centered.

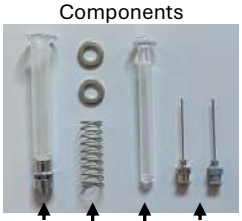


Adjustment leg



Set up the syringe

Components



=





Glass syringe

2x washers

Spring

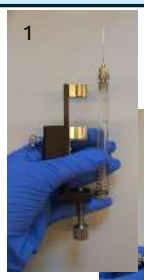
Syringe pusher

SUS & Teflon needle 22G

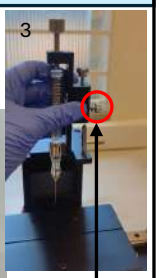
Assemble the syringe and draw up the liquid from a cup or bottle. Be careful to avoid drawing too many air bubbles.

Set up the dispenser

1. Place the syringe into the dispenser. Be sure that the discharge/suction knob is screwed out for optimal space.
2. Point the needle upward and turn the knob to release all the air bubbles.
3. Insert the dispenser into the column and tighten using the lock knob.







Lock knob

Discharge/ suction knob

Remove camera cover



Unscrew the camera cover from the lens.

Connect the laptop & start FAMAS

Turn on the laptop and connect the following to the laptop:

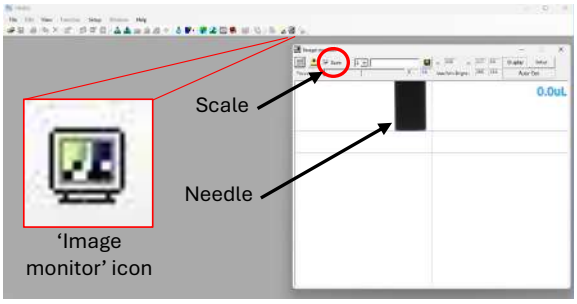
1. The DMs-401 instrument connector cable (USB).
2. The Kyowa software (USB).
3. FAMAS Ver. 7 software (USB).

Start the FAMAS software by clicking the icon on the screen.

Icon on laptop



Image monitor



Once FAMAS opens, click the image monitor icon to display the needle. Check the scale box to display the scale.

Position the needle tip

Position the needle tip in the center of the dotted vertical line using the left/right adjustment knob. Position the needle tip to extend 1/3 to 1/4 down the screen using the dispenser height adjustment knob. Tighten the dispenser lock knob.

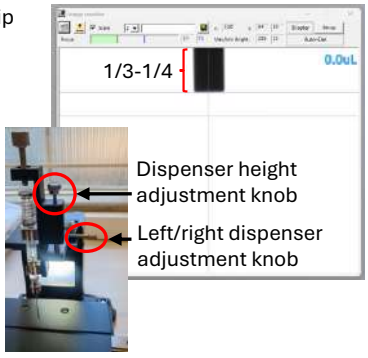


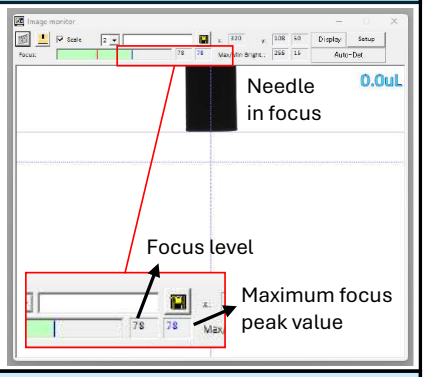
Figure A: Contact Angle Meter DMs-401 instruction guide, page 1.

Focus the needle tip



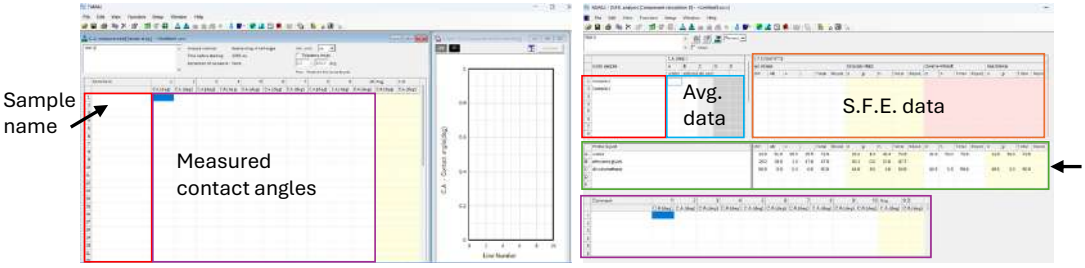


Focus the needle tip by using the camera focus adjustment knob. Adjust the light volume using the light-volume adjustment knob. The maximum brightness guideline is 230±20.

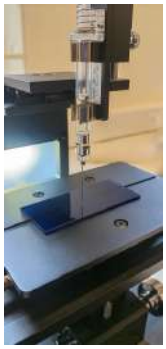


Open a measurement sheet

Click the "View" tab in the tool bar or the "Display" tab on the menu to open a measurement sheet. Select the appropriate measurement sheet relevant to your work. Example. Left – C.A. measurement [Sessile drop]; Right – S.F.E. analysis [Component calculation B]. For [Component calculation B], set to binary (2 liquids) or tertiary (3 liquids).



Place prepared sample on stage



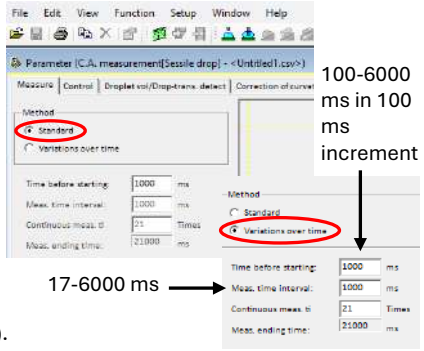
Ensure the sample is flat, smooth and clean from any chemicals and dust. Place the sample in the center of the stage. Be sure not to touch the needle.



Flat, smooth and clean sample surface shown on the image monitor.

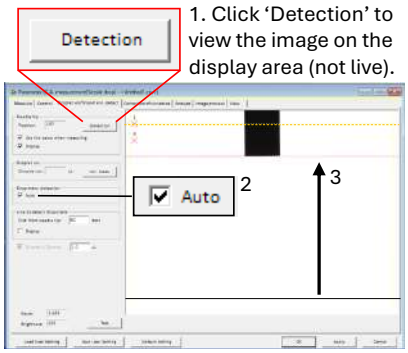
Set the parameters - Measure

To set the parameters, click "Setup" in the toolbox. To specify the measurement method, select between 'Standard' (static-) or 'Variations over time' (dynamic-measurements).



Set the parameters – Droplet vol.

2. Turn on the automation of 'Drop-trans. detect'.
3. On the image monitor, move the solid line (droplet volume scale line) to the needle tip.



1. Click 'Detection' to view the image on the display area (not live).

Set the parameters – Droplet vol.

1. Discharge a droplet into the needle using the discharge/ suction knob. Click 'Vol. Meas.' to measure the droplet. You can specify a droplet volume.
2. Move the solid line to the droplet.

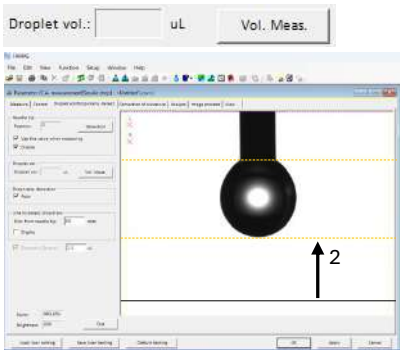
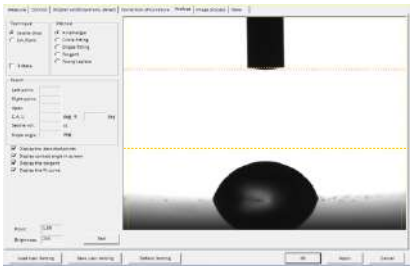


Figure B: Contact Angle Meter DMs-401 instruction guide, page 2.

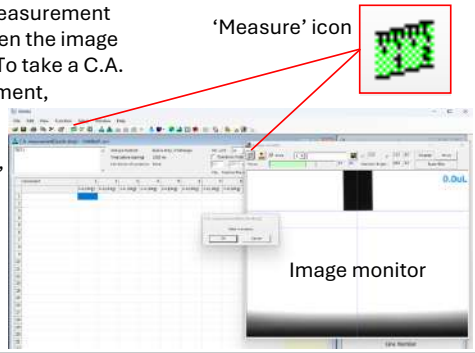
Set the parameters - Analyze

Specify the analysis method of a C.A. on the droplet image. The method can be modified on the property window after the measurement.



Take a measurement

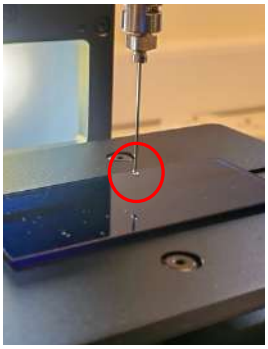
On the measurement sheet, open the image monitor. To take a C.A. measurement, click the green 'Measure' icon.

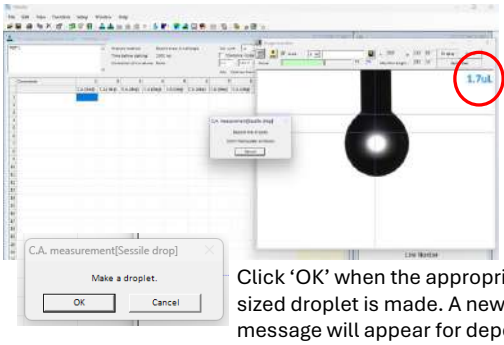


Make a droplet



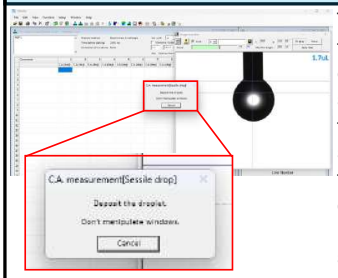
To dispense a droplet, turn the discharge/ suction knob until the appropriate droplet size is out at the tip of the needle.





Click 'OK' when the appropriate-sized droplet is made. A new message will appear for deposition.

Deposit the droplet



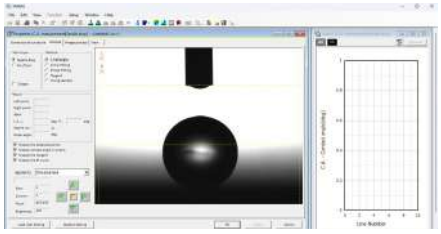
Do not click 'Cancel'.



To deposit the droplet, elevate the stage until the sample surface touches the droplet. Lower the stage. The instrument will read the C.A. and the record the value.

Modify saved data

To modify the data of a measured C.A., double-click on a cell containing the measurement data to open the property sheet. Change the analysis method and modify the endpoint if desired. Save the data.



Transfer the data

1. Save your work in an appropriate folder.
2. Label it well.
3. Open your student Google Drive.
4. Transfer all your work.
5. Log out of your Google Drive account.

Clean up

1. Turn off instrument at power switch and wall switch.
2. Screw camera cover back on.
3. Exit FAMAS and remove all USBs from laptop safely.
4. Turn off laptop and pack away.
5. Cover the instrument with the protective cover.
6. Clean all apparatus with distilled water or alcohol & distilled water (if probe liquid is not water) and allow to air dry.
7. Leave area clean and tidy.
8. Discard lab gloves.

Figure C: Contact Angle Meter DMs-401 instruction guide, page 3.

Appendix B: Manual SFE calculations

The Contact Angle Meter DMs-401 automatically calculates the SFE of each solid aggregate. This section outlines the manual calculations using three equations that require the known components of the probe liquids and the average contact angles ($\boldsymbol{\theta}$) measured using the SD method. Table B-1 tabulates these values.

The first component that is determined is the Lifshitz-van der Waals component (γ^{SLW}), thereafter the Lewis acid (γ^{S+}) and base (γ^{S-}) components are determined using simultaneous equations.

The following equations are used.

Total surface free energy equation

$$\gamma = \gamma^{LW} + \gamma^{AB}$$

Acid-base components of SFE equation

$$\gamma^{AB} = 2\sqrt{\gamma^{+}\gamma^{-}}$$

Young-Dupré equation

$$\gamma^{L}(1 + cos\theta) = 2(\sqrt{\gamma^{SLW}\gamma^{LLW}} + \sqrt{\gamma^{S+}\gamma^{L-}} + \sqrt{\gamma^{S-}\gamma^{L+}})$$

Table B-1: The components for each probe liquid, where γ^{LLW} is the Lifshitz-van der Waals component, γ^{LAB} is the total Lewis acid-base, γ^{L+} is the Lewis acid component, γ^{L-} is the Lewis base component, and γ^{L} is the total of these energies.

Probe liquid	γ^{LLW}	γ^{LAB}	γ^{L+}	γ^{L-}	γ^{L} (total)	Av. $\boldsymbol{\theta}$
Water	21.8	51.0	25.5	25.5	72.8	88.85
Ethylene Glycol	29.0	18.9	1.9	47.0	47.9	70.75
Diiodomethane	50.8	0.0	0.0	0.0	50.8	62.30

Calculation:

$$\gamma^L(1+cos\theta) = 2(\sqrt{\gamma^{SLW}\gamma^{LLW}} + \sqrt{\gamma^{S+}\gamma^{L-}} + \sqrt{\gamma^{S-}\gamma^{L+}})$$

For diiodomethane: (θ = 62.30°); (γ^{LAB} = 0), therefore:

$$\gamma^L(1+cos\theta) = 2(\sqrt{\gamma^{SLW}\gamma^{LLW}}$$

$$(50.8)(1+\cos(62.30)) = 2(\sqrt{\gamma^{SLW}(50.8)}$$

$$74.41 = 2(\sqrt{50.8\,\gamma^{SLW}})$$

$$37.21 = \sqrt{50.8\,\gamma^{SLW}}$$

$$50.8\,\gamma^{SLW} = 37.21^2$$

$$\gamma^{SLW} = \mathbf{27.25\ mN/m}$$

For water: (θ = 88.85°)

$$(72.8)(1+\cos(88.85)) = 2(\sqrt{(27.25)(21.8)} + \sqrt{\gamma^{S+}(25.5)} + \sqrt{\gamma^{S-}(25.5)})$$

$$74.26 = 2(24.37 + \sqrt{25.5\,\gamma^{S+}} + \sqrt{25.5\,\gamma^{S-}})$$

$$37.13 = (24.37 + \sqrt{25.5\,\gamma^{S+}} + \sqrt{25.5\,\gamma^{S-}})$$

$$12.76 = \sqrt{25.5\,\gamma^{S+}} + \sqrt{25.5\,\gamma^{S-}} \qquad \mathbf{1}$$

For ethylene glycol: (θ = 70.75°)

$$(47.9)(1+\cos(70.75)) = 2(\sqrt{(27.25)(29.0)} + \sqrt{\gamma^{S+}(47.0)} + \sqrt{\gamma^{S-}(1.9)})$$

$$63.69 = 2\left(28.11 + \sqrt{47.0\,\gamma^{S+}} + \sqrt{1.9\,\gamma^{S-}}\right)$$

$$31.85 = (28.11 + \sqrt{47.0\,\gamma^{S+}} + \sqrt{1.9\,\gamma^{S-}})$$

$$3.74 = \sqrt{47.0\,\gamma^{S+}} + \sqrt{1.9\,\gamma^{S-}}$$

$$\sqrt{47.0\,\gamma^{S+}} = (3.74 - \sqrt{1.9\,\gamma^{S-}})$$

$$47.0\,\gamma^{S+} = (3.74 - \sqrt{1.9\,\gamma^{S-}})^2$$

$$\gamma^{S+} = \frac{(3.74-\sqrt{1.9\,\gamma^{S-}})^2}{47.0} \qquad \mathbf{2}$$

Substitute 2 into 1:

$$12.76 = \sqrt{25.5 \times \frac{\left(3.74 - \sqrt{1.9\,\gamma^{S-}}\right)^2}{47.0}} + \sqrt{25.5\,\gamma^{S-}}$$

$$(12.76)^2 = \left(\sqrt{\frac{\left(95.37 - 25.5\sqrt{1.9\,\gamma^{S-}}\right)^2}{47.0}} + \sqrt{25.5\,\gamma^{S-}}\right)$$

$$162.82 = \frac{9095.44 - \left(190.74 \times 25.5\sqrt{1.9\,\gamma^{S-}}\right) + (25.5\sqrt{1.9\,\gamma^{S-}})^2}{47.0} + 25.5\,\gamma^{S-}$$

$$162.82 = \frac{9095.44 - \left(4863.87\sqrt{1.9\,\gamma^{S-}}\right) + (650.25 \times 1.9\,\gamma^{S-})}{47.0} + 25.5\,\gamma^{S-}$$

$$162.82 = \frac{9095.44 - \left(4863.87\sqrt{1.9\,\gamma^{S-}}\right) + 1235.48\,\gamma^{S-}}{47.0} + 25.5\,\gamma^{S-}$$

$$162.82 = 193.52 - 103.49\sqrt{1.9\,\gamma^{S-}} + 26.29\,\gamma^{S-} + 25.5\,\gamma^{S-}$$

$$0 = 30.70 - 103.49\sqrt{1.9\,\gamma^{S-}} + 51.79\,\gamma^{S-}$$

$$\left(103.49\sqrt{1.9\,\gamma^{S-}}\right)^2 = (51.79\,\gamma^{S-} + 30.70)^2$$

$$10710.18\,(1.9\,\gamma^{S-}) = 2682.20\,\gamma^{S-2} + 3179.91\,\gamma^{S-} + 942.49$$

$$20349.34\,\gamma^{S-} = 2682.20\,\gamma^{S-2} + 3179.91\,\gamma^{S-} + 942.49$$

$$0 = 2682.20\,\gamma^{S-2} - 17169.43\,\gamma^{S-} + 942.49$$

$\gamma^{S-} = \frac{-b \pm \sqrt{b^2 - 4ac}}{2a}$, where $a = 2682.20, b = -17169.43\ and\ c = 942.49$

$$\gamma^{S-} = \frac{-(-17169.43) \pm \sqrt{(-17169.43)^2 - 4(2682.20)(942.49)}}{2(2682.20)}$$

$$\gamma^{S-} = \mathbf{6.35\ or\ 0.06\ mN/m} \qquad \mathbf{3}$$

Substitute 3 into 2:

$$\gamma^{S+} = \frac{(3.74 - \sqrt{1.9\,\gamma^{S-}})^2}{47.0}$$

$\gamma^{S+} = \frac{(3.74 - \sqrt{1.9 \times 6.35})^2}{47.0}$ or $\gamma^{S+} = \frac{(3.74 - \sqrt{1.9 \times 0.06})^2}{47.0}$

$$\gamma^{S+} = \mathbf{1.51 \times 10^{-3}\ or\ 0.25\ mN/m}$$

Total SFE

$$\gamma = \gamma^{LW} + \gamma^{AB}$$
$$= \gamma^{LW} + 2\sqrt{\gamma^{+}\gamma^{-}}$$
$$= 27.25 + 2\sqrt{(1.51 \times 10^{-3})(6.35)}$$
$$= \boldsymbol{27.45\ mN/m}$$

The automated value determined by the Contact Angle Meter DMs-401 for these contact angles = 27.25 mN/m.

Appendix C: Manual bending strength calculations

The manual calculations for the bending strength of the prisms use Equations 2.11 and 2.14. The first component calculated is the applied force (P) and then the bending strength (σ). The necessary components to calculate the bending strength are tabulated in Table C-1: the load measured at failure (m), the width (b) and the height (d) of the interface prepared for bonding.

The following equations are used.

Force applied equation

$$P = m \times g$$

Bending strength equation

$$\sigma = \frac{3PL}{2bd^2}$$

Table C-1: The failure load (m), width (b) and height (m) of the aggregate interface.

Measured variables			Known variables	
m (kg)	b (mm)	d (mm)	L (mm)	g (m/s^2)
108	43	37	137.5	9.81

Calculation:

$$P = m \times g$$
$$= 81 \times 9.81$$
$$= 794.61\ N$$

$$\sigma = \frac{3PL}{2bd^2}$$
$$= \frac{3(794.61)(137.5)}{2(39)(39)^2}$$
$$= \mathbf{2.76\ MPa}$$